Image Encoding and Reconstruction for Portable Magnetic Resonance Imaging

A Thesis Submitted to the

College of Graduate Studies and Research

in Partial Fulfillment of the Requirements

for the degree of Doctor of Philosophy

in the Division of Biomedical Engineering

University of Saskatchewan

Saskatoon

By

Somaie Salajeghe

Permission to Use

In presenting this thesis in partial fulfilment of the requirements for a Postgraduate degree from the University of Saskatchewan, I agree that the Libraries of this University may make it freely available for inspection. I further agree that permission for copying of this thesis in any manner, in whole or in part, for scholarly purposes may be granted by the professor or professors who supervised my thesis work or, in their absence, by the Head of the Department or the Dean of the College in which my thesis work was done. It is understood that any copying or publication or use of this thesis or parts thereof for financial gain shall not be allowed without my written permission. It is also understood that due recognition shall be given to me and to the University of Saskatchewan in any scholarly use which may be made of any material in my thesis.

Requests for permission to copy or to make other use of material in this thesis in whole or part should be addressed to:

Head of the Division of Biomedical Engineering

Room 2B60 57 Campus Drive

University of Saskatchewan

Saskatoon, Saskatchewan, S7N 5A9

Canada

Abstract

Magnetic Resonance Imaging (MRI) is a successful imaging tool, but due to high cost, high weight and complexity of equipment, MRI is not currently as easily accessible clinically as desired. By making MRI cheaper, lighter, less complex and therefore potentially portable, it can become more widely accessible. A portable MRI system can be used in primary health care, operating and emergency rooms, car and air ambulances, sport and war facilities and remote regions (including outer space).

The objective of this study was to show the feasibility of reconstructing MRI signals generated by two different portable MRI systems. The first portable MRI, known as radiofrequency (RF) phase encoded MRI, encodes spatial information through the use of a non-linear spatially varying RF transmit (B_1) phase. The second portable MRI, known as rotating field MRI, encodes information through non-uniform radially varying main magnet field (B_0). The fact that there is no need for gradient coils in both systems, leads to a smaller, lighter and more affordable MRI than most conventional systems.

In RF phase encoded MRI, since the B_1 phase spatially varies non-linearly, using Fourier transform (FT) to reconstruct images results in distorted images. Therefore, regularized least squares inversion was used in place of the usual FT. The RF phase encoding coil generates an inhomogeneous B_1 field that leads to RF pulse imperfection in terms of flip angles produced versus flip angles intended. Composite pulses were therefore used to minimize the effect of RF transmit field inhomogeneity on tip angles.

In rotating field MRI, a Halbach magnet was used to generate a non-uniform radially varying B_0 field to encode information in the radial direction. For encoding information in the angular direction two separate Saddle RF receiver coils were used. The main magnet and receiver coils are

fixed relative to each other, but both rotate around the object. A regularized least squares inversion (LS) method followed by total variation (TV) techniques were used to reconstruct the images.

MRI simulation signals encoded in RF transmit field with non-linearly varying spatial phase may be accurately reconstructed using regularized LS method thus pointing the way to the use of simple RF coil designs for RF encoded MRI. Also, my results from simulation and experimental data, indicated the feasibility of reconstructing images from rotating field MRI. I have made progress in the realization of a novel approach to different MRI systems that do not rely on active magnetic gradient fields. These two methods can be combined to encode information in 3 dimensions (3D) in the future, for example inhomogeneous B_0 field can be used for slice selection and RF phase encoding can be used to encode information in the plane.

Acknowledgements

The work presented here was not possible without the support and encouragement of many individuals. I feel very fortunate to have worked with and learned from all of them.

I want to thank my thesis advisers Dr. Gordon Sarty and Dr. Paul Babyn for their guidance and encouragement. My appreciation is beyond expression. Dr. Sarty is the one who introduced me to the MRI world and granted me the opportunely to work on such a exciting project. He was there for me whenever I needed him to discuss and he has given me always intellectual inputs. Dr. Babyn was the one who always asked critical clinical questions which made me think more. He was always very supportive of my dreams and open to help.

I would also like to express my appreciation to my advisory committee members; Dr. Jonathan Sharp for his valuable inputs and advice on this research, Dr. Artur Sowa for giving me access to work with multiphysics modeling software, COMSOL, Dr. James (J.D.) Johnston for his help on writing.

I would like to thank Dr. Logi Vidarsson from LT imaging company for building the MRI (in chapter six of this thesis) and for all his help and advice on this research. I would also like to thank Dr. Michael Bradley for giving me access to use the RF shield room in Department of Physics and Engineering Physics of University of Saskatchewan.

I acknowledge my great friends in Canada, I am especially thankful to Walter and Luella Bergen for their kindness and support. They were like a family for me and I had such a memorable time with them in Saskatoon.

I gratefully acknowledge the funding provided by the Division of Biomedical Engineering of University of Saskatchewan, NSERC Discovery Grant for Dr. Sarty, Grant for Dr. Babyn, Saskatchewan Innovation and Opportunity Award, Toyota Automotive Engineering and Safety Award, and Fred-

erick Wheeler & W.H.T. Spary Graduate Scholarship.

I would like to express my deepest appreciation to my family members in Iran for their support and patience. Finally I want to thank my best friend who is also my husband, Majid, for his love, support, encouragement and for always being there for me.

I dedicate this dissertation to my brilliant husband, Majid, for his constant love and support and my parents for their encouragement.

Contents

List of Tables

List of Figures

List of Abbreviations

MRI	Magnetic Resonance Imaging
NMR	Nuclear Magnetic Resonance
B_0	Main magnetic field
B_1	Transverce Radiofrequency field
RF	Radiofrequency
FT	Fourier Transform
FFT	Fast Fourier Transform
DFT	Discrete Fourier Transform
Flip angle	The amount of rotation the net magnetization received by RF pulse
N	Image size
PSF	Point Spread Function
FOV	Field of View
fMRI	Functional Magnetic Resonance Imaging
SEMs	Spatial Encoding Magnetic Fields
LS	Least Squares
TV	Total Variation
CT	Computed Tomography
RMSE	Root Mean Square Error
SNR	Signal-to-Noise Ratio
T_1	Longitudinal relaxation time
T_2	Transverse relaxation time
γ	Gyromagnetic ratio
μ	Magnetic moment
J	Angular momentum
ω_0	Resonant frequency
M	Net Magnetization
S	Signal
180_x	180° tip angle excitation with the x direction RF encoding coil
180_U	180° tip angle excitation with uniform coil
G_x	Phase gradient in x direction
G_y	Phase gradient in y direction
k_x	Spatial frequencies in x direction
k_y	Spatial frequencies in y direction
Φ	Phase of the B_1 field for RF phase encoded coil
$[\mathrm{Rot_x}]$	Rotation about x
$[\mathrm{Rot_y}]$	Rotation about y
$[\mathrm{Rot_z}]$	Rotation about z
α	Nominal tip angle
ΔB	Inhomogeneity of the main magnet field
CPMG	Carr-Purcell-Meiboom-Gill

Chapter 1

Introduction

1.1 Statement of Problem and Purpose of Study

MRI is a non-invasive diagnostic medical imaging tool which utilizes a strong magnetic field, gradient field and RF energy for imaging. MRI is one of the most useful imaging modalities, but broader dissemination is currently limited by its high cost and complexity of equipment. Ways to reduce the complexity, cost and weight of MRI, and improve access are thus deemed beneficial.

By reducing complexity, cost and weight, MRI may be made more compact and hence potentially portable. This would allow potentially use in primary health care, ambulance services, sports arenas, military field hospitals, and operating and emergency rooms. This would also allow improved access specially to pediatric patients. Thereby Computed Tomography (CT) scanners can be replaced by portable MRI in pediatrics which is important, because radiation doses from CT scans increase the risk of cancer [1] specially in children [2, 3].

Portable MRI can also be used in remote regions (including outer space). If astronauts who stay in space for a long time can use MRI, we will have more information about the progress of their physiological alterations. Weightlessness affects their musculoskeletal system leading to microgravity induced osteoporosis, so one may be able to use the achieved

information from astronaut's images to better understand osteoporosis pathogenesis [4]. Now the question is how we can reduce cost and weight of MRI.

Conventional MRIs use gradient coils to modify the main magnetic field for the purpose of encoding spatial information. Gradient coils have different parts such as a power supply, air and water cooling systems (for themselves and their power electronics), filters, and cables. Therefore a significant fraction of MRI weight, power and complexity pertains to the gradient coils [5]. Also, the gradient coils are bulky and occupy a significant space inside the magnet bore (where the imaging take place) [5]. The bore consists of visible space and the space taken up by the coils. Therefore, the bore is required to be wide enough to provide adequate space. The wider the bore, the weaker the magnetic field inside the bore. Moreover, placing the coils in the magnet will alter its homogeneity. Gradient coils are needed to switch on and off which may cause additional problems discussed below.

Loud acoustic noises and vibrations are created by switching gradient pulses which may cause concern for some patients, especially pediatric. When currents are passed through the gradient wires, the gradient coils interact with the main magnetic field which leads to Lorentz forces. The Lorentz forces on the wires are the source of the acoustic noises [6]. The acoustic noises could especially cause problems when functional Magnetic Resonance Imaging (fMRI) is performed. The noises create activation in brain regions which may interfere with auditory processing [7, 8, 9]. It also may affect patient's hearing and make some temporary hearing threshold shifts if the patients are kept for a long time in the MRI [10]. Switching gradients additionally generate eddy currents in close conductors (including the patient) which may lead to image artifacts [5].

By eliminating the gradient coil subsystems, a portion of MRI costs related to installation,

operating and maintenance will be eliminated [11]. Alternative imaging techniques have been proposed which use different methods to encode spatial information (more details in chapter 2) in an effort to remove gradient coils. Among such techniques, RF phase encoded technique which uses RF phase gradient, instead of gradient coils to encode information are discussed in this research.

A truly portable MRI is possible by lessening B_0 field homogeneity requirements in addition to gradient coils. Conventional MRIs use a uniform B_0 field to polarize the sample being imaged. Inhomogeneity in the B_0 field leads to image distortion in conventional MRIs. It is impossible to have a perfectly homogeneous B_0 field in practice, thus shim coils and other main magnet homogeneity requirements are used to remove the inhomogeneity of the field. However, shim coils and other B_0 homogeneity requirements result in expensive and heavy MRIs. Therefore by eliminating shim coils and other B_0 homogeneity requirements, a significant fraction of MRI cost and weight will be removed. Rotating field MRI uses the B_0 inhomogeneity to encode information, instead of gradient coils. Therefore there is no need for gradient coils and shim coils in a rotating field MRI and this technique is discussed in this research. My overall dissertation research objective was to develop accurate techniques to reconstruct data obtained from RF phase encoded MRI and rotating field MRI. The structure of this dissertation is provided below.

1.2 Thesis Outline

Chapter two provides a brief introduction to the physics, hardware, encoding and image reconstruction of conventional MRIs. Literature related to existing encoding methods which remove the need for gradient coils is also presented here. The two image encoding methods

(RF phase encoded MRI and rotating filed MRI) which may result in a portable MRI and are the focus of this research are also presented.

In chapter three several configurations for an RF phase encoded coil are developed and designed. Such a coil generates an RF field with varying phase which can be used to encode information in MRI. The Pulse sequences which can be used in RF phase encoded MRI to produce the require signals, are also discussed in this chapter.

Chapter four focuses on image reconstruction methods of signal generated from RF phase encoded coils. It is shown that Fourier image reconstruction leads to a distorted image which is due to non-linearity of the RF field phase. Later in this chapter, another reconstruction method is introduced. The method is based on an algebraic reconstruction method which leads to an inverse problem.

The RF phase gradient coil generates an inhomogeneous B_1 field that leads to spatially dependent flip angles. The effect of B_1 inhomogeneity on tip angles may be minimized using composite pulses. Chapter five assesses different composite pulses to compensate for B_1 inhomogeneities.

Chapter six provides information about a rotating field MRI which encodes information using a non-uniform radially varying B_0 field for radial direction and variation of receiver B_1 field for angular direction. The reconstruction method is applied to the signals generated from the rotating field MRI to obtain an image.

Chapter seven includes the summary and conclusions of the work. Future directions are also provided.

1.3 Contributions

Sections of this thesis have been submitted in refereed journals and conferences. Details of these submissions can be found in Appendix. The research was performed by me except for building the MRI scanner, which was built by LT Imaging Inc. Data analyses and manuscript preparation were carried out by me and the co-authors contributed in editing the manuscripts for submission to refereed journals.

Chapter 2

Background

MRI is a non-invasive imaging tool which uses a strong magnetic field, RF energy and field gradients for imaging the anatomy and the physiological processes of the body, based on the science of Nuclear Magnetic Resonance (NMR). NMR is a quantum mechanical phenomenon in which nuclei of atoms with non-zero spin values absorb and emit RF energy at their resonance frequency when placed in an external magnetic field. The resonance frequency is called the Larmor frequency, ω_0, and depends on the magnetic field magnitude and the physical properties of the nuclei. By varying the magnetic field spatially, the Larmor frequency will also vary spatially which can be used to form an image. Lauterbur [12] and Mansfield [13] introduced the use of gradient coils to encode information by varying the magnetic field spatially. In this chapter the physics of MRI including magnetization vector, application of an RF field and Bloch equation will be explained. Also, information about spatial localization including spatial encoding, signal detection and image reconstruction will be presented.

2.1 MRI Physics

2.1.1 Spin and Magnetization

Human body is mostly composed of hydrogen atoms [14]. Nuclei (the combination of protons and neutrons) which have an odd number of protons or neutrons have an angular momentum

(J) which is called spin [14]. Therefore, the proton, the nucleus of the hydrogen atom, can be considered as a charged particle spinning about its own axis [14]. The spinning motion causes a magnetic dipole moment (μ) in the direction of the spin axis like a tiny bar magnet. When a magnetic dipole moment is placed in an external magnetic field (B_0), a torque is experienced by the dipole such that the moment vector will align with the B_0 field. The spin associated with the magnetic moment causes the magnetic moment to precess around the axis of B_0 with a Larmor frequency. The Larmor frequency is given by the Larmor equation and is proportional to the local magnetic field strength by:

$$\omega_0 = \gamma\, B_0 \tag{2.1}$$

Where γ is the gyromagnetic ratio and is equal to 42.57 MHz/T for a proton [15].

In quantum theory, when protons are located in a B_0 field, they may become aligned in one of two possible orientations: parallel (low energy state) or anti-parallel (high energy state) to the B_0 field [14, 16]. Following Boltzmann's law, the population of nuclei in the higher energy level is less than the population of nuclei in the lower energy level [17]. The population difference results in a net magnetization (sum of magnetic moments (M)) directed along B_0 and precessed around it as shown in Figure 2.1. The behavior of M in presence of a B_0 field can be shown by Bloch Equation as (Without relaxation terms):

$$\frac{d\vec{M}}{dt} = \gamma \vec{M} \times \vec{B} \tag{2.2}$$

2.1.2 Application of an RF field

M is in the direction of B_0 and the spin system is in its lowest energy state. However, when an RF field with a frequency equal to the resonant frequency of the spins is applied in the

plane perpendicular to the B_0, M moves away from the z direction (the direction of the B_0) [14]. The transverse RF field (B_1) will tip away the net magnetization from the longitudinal axis to a certain angle which is called the flip angle. The flip angle is directly proportional to the duration and strength of the applied B_1 field [16].

B_1 is generated by an applied electromagnetic pulse and induces resonance (happens when the RF frequency is equal to the Larmor frequency and in sync with the precessing magnetization) [18]. The RF field can be written as two circularly polarized components: one rotating clockwise (plus sign) and the other counter-clockwise (minus sign) as:

$$\vec{B_1}(t) = B_1(t)[\cos(\omega t)\vec{i} + \sin(\omega t)\vec{j}] + B_1(t)[\cos(\omega t)\vec{i} - \sin(\omega t)\vec{j}] \tag{2.3}$$

The only component of an RF field affecting the magnetization is the clockwise component, because it rotates in sync with the magnetization.

The total magnetic field seen by magnetization, B in Eq. (2.2), is equal to the clockwise circularly polarized component of the B_1 field and the B_0 field as:

$$\vec{B} = \vec{B_1} + \vec{B_0} = B_1(t)\cos(\omega t)\vec{i} + B_1(t)\sin(\omega t)\vec{j} + B_0\vec{k} \tag{2.4}$$

The equation of motion for the magnetization M in the presence of B_0 and B_1 fields can be shown by Bloch equations which will be discussed in the next section.

2.1.3 Bloch Equation

It is hard to analyze the magnetization M behavior in the presence of B_0 and B_1 fields by solving the Bloch Eq. (2.2) in the reference plane. Therefore, a rotating frame is used to simplify solving Bloch Equation. The rotating frame is a Cartesian coordinate system rotating around the magnetization vector with angular velocity of Larmor frequency (see

Figure 2.1). Therefore, the effective B in Eq. (2.2) viewed from the rotating frame can be considered as:

$$\vec{B} = B_1(t)\vec{i'} \tag{2.5}$$

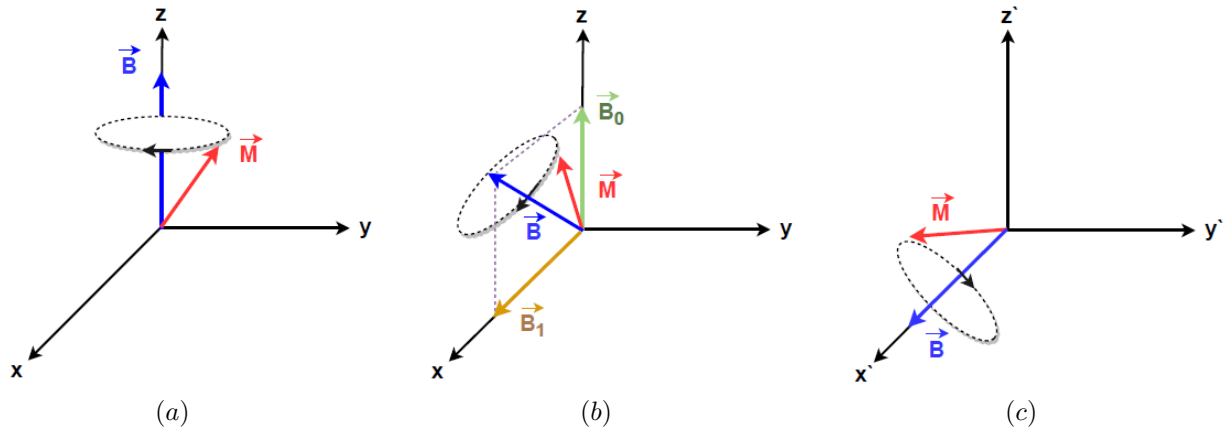

Figure 2.1: This figure shows the principles of MRI. (a) The magnetization rotates around the effective magnetic field which is the B_0 field. (b) The magnetization rotates around the effective magnetic field which is the sum of the B_0 field and the B_1 field in the reference plane. (c) The magnetization rotates around the effective magnetic field which is the sum of the B_0 field and the B_1 field in the rotating reference frame.

Please consider that x, y and z will be used instead of x', y' and z' in the rotating frame through this thesis. The Bloch Equation shown in Eq. (2.2) was considered without the effect of relaxation time. Relaxation is the process by which the magnetization returns to an equilibrium state [17]. The process of energy exchange between the magnetization of nuclei and their environment or between the magnetization and neighbouring magnetization is described by the Bloch equation as (without considering the Diffusion term) [16]:

$$\frac{\mathrm{d}}{\mathrm{d}t}\vec{M} = \gamma\vec{M} \times \vec{B}_0 + \frac{(M_0 - M_z)\vec{k}}{T_1} - \frac{(M_x\vec{i} - M_y\vec{j})}{T_2} \tag{2.6}$$

where $\vec{M} = M_x\vec{i} + M_y\vec{j} + M_z\vec{k}$, M_z is the magnetization component in z direction (longitudinal magnetization), M_x is the magnetization component in x direction and M_y is the

magnetization component in y direction. The first term in the right hand side of Eq. (2.6) is the precession without T_1 and T_2 effects. The other two terms in the right hand side of Eq. (2.6) can be split up into the longitudinal relaxation (T_1) effects [16]:

$$\frac{\mathrm{d}}{\mathrm{d}t}\vec{M_z} = -\frac{(M_z - M_0)\vec{k}}{T_1} \tag{2.7}$$

And the transverse relaxation (T_2) effects [16]:

$$\frac{\mathrm{d}}{\mathrm{d}t}\vec{M_{xy}} = \frac{M_x\vec{i} + M_y\vec{j}}{T_2} \tag{2.8}$$

where $M_{xy} = M_x\vec{i} + M_y\vec{j}$ is transverse magnetization.

The solution to the equation of the longitudinal magnetization behavior, defined by Eq. (2.7), is:

$$M_z = M_{z(0)}e^{-t/T_1} + M_0(1 - e^{-t/T_1}) \tag{2.9}$$

The mechanism of T_1 relaxation is that the protons release the energy absorbed from the RF pulse to the surrounding environment. Therefore, T_1 is called the spin-lattice relaxation time as well. T_1 relaxation varies with the strength of the main magnetic field and increases with higher field magnets [14]. For a fixed B_0 field T_1 varies with tissue type.

The solution to the equation of the transverse magnetization behavior, defined by Eq. (2.8), will be:

$$M_{xy} = M_{xy(0)}e^{-t/T_2} \tag{2.10}$$

The mechanism of T_2 relaxation is that the spins interact with each other. As a result, they lose their phase coherence and the overall transverse magnetization Mxy is reduced. T_2 relaxation is independent of the strength of the B_0 field [14]. For a fixed B_0 field T_2 varies with tissue type. Eqs. (2.9) and (2.10) are plotted in Figure 2.2.

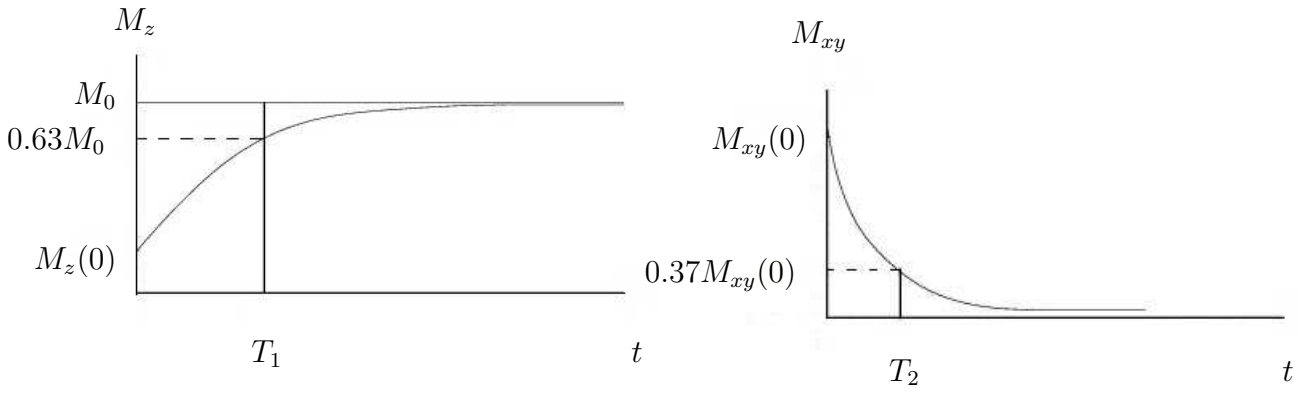

Figure 2.2: T_1 and T_2 relaxation. Right after a 90° RF pulse, there is no longitudinal magnetization (M_z). T_1 is the time when M_z reaches to 63% of M_0 and T_2 is the time when M_{xy} reaches to 37% of the maximum value.

2.2 Imaging

2.2.1 Signal Detection

A receiver coil is placed along the object to detect the signal emitting from the nuclei in the sample. A time-varying magnetic field passing through the conductor loop induces a voltage in the loop. The voltage in the loop equals the negative time derivative of the magnetic flux through the loop:

$$V(t) = -\frac{d\phi}{dt} = -\int_s \frac{\partial B}{\partial t}.\, dA \tag{2.11}$$

where ϕ is the magnetic flux, A is the area of the loop and B is the magnetic field passing through the receiver coil.

The detected signal is the integral of the magnetization over the field of view (FOV). A single number will be detected for the whole body without spatial localization. Therefore, there must be a way to separate signal to determine its origin in three dimensions.

2.2.2 Spatial Encoding and Image Reconstruction

In order to recover the distribution of magnetization, a spatially varying field in the x, y and z directions is needed to be generated in the sample, in a way that nuclei at different locations produce signal which has information about their location. There are different ways to encode spatial information (see Figure 2.3) which will be discussed in detail below.

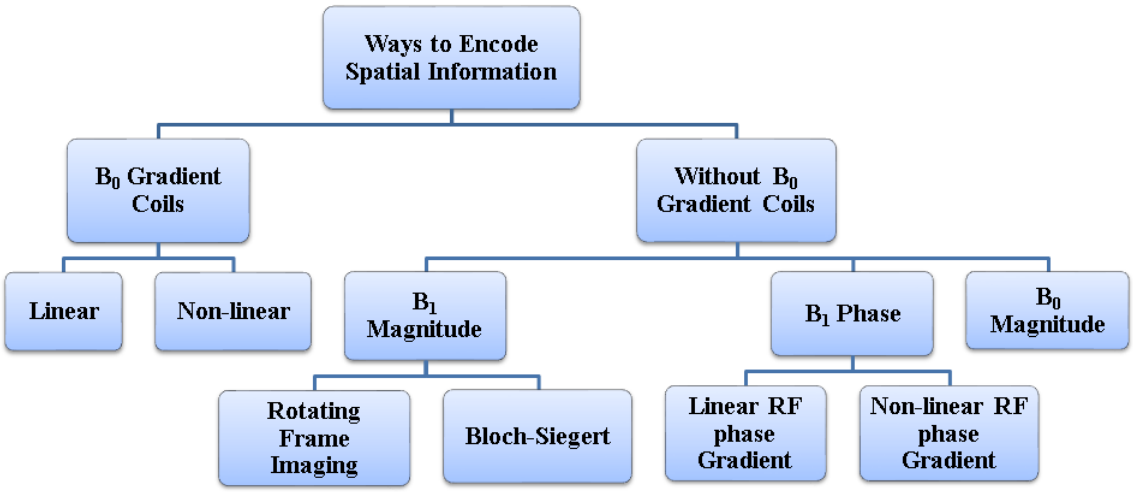

Figure 2.3: Different ways to encode information.

Spatial Encoding with B_0 Gradient Coils

B_0 Gradient coils generate gradient fields which vary frequency ω and phase ϕ over the sample in a way that the original distribution of transverse magnetization Mxy can be recovered from a set of integrals. There are three different types of spatial encoding: slice selective excitation, frequency encoding, and phase encoding.

Slice selection is performed by a gradient coil which generates gradient field in the appropriate direction. For example, by turning on the z gradient coil, the protons at each position in the body experience different magnetic fields which lead to corresponding gradient in the

precession frequencies along the body. Therefore, by varying the frequency of the RF pulse, it is possible to excite a specific corresponding slice. As such, only the protons in that slice are excited, because their Larmor frequency matches the frequency of the pulse. Therefore, the generated signal is an integration over the specific corresponding slice. To get information about individual pixels in the selective slice, the phase encoding and frequency encoding gradients are needed.

Phase encoding is performed by switching on a gradient coil which generates a gradient field in the y direction for example, after the RF pulse. The phase encoding gradient makes nuclei at the top of the sample precess with higher frequency than the nuclei at the bottom. Therefore, each transverse magnetization vector has its own unique Larmor frequency. After the gradient is switched off, the precession frequency returns to a constant value over the plane (the same frequency), while the phase remains proportional to y (different phases). As such, information in the y direction is encoded. In order to encode information in x direction frequency encoding is performed by switching on a gradient coil which generates gradient field in the x direction. The frequency encoding gradient causes nuclei on one side of the sample precess with lower frequency than the nuclei on the other side, because they received different magnetic field. Therefore, different locations will have different frequencies which can be used to encode information in the x direction. Using frequency encoding in addition to the phase encoding will determine the spatial position of the MR signal within the selected slice.

Linear : B_0 gradient coils generate magnetic fields with much weaker intensity than B_0 and vary linearly across the x, y or z directions. They can be turned on in combinations to create a linear gradient in any direction in space. Regarding the Larmor equation in Eq. (2.1), if

the magnetic field varies across space, the precession frequency of the protons vary as well.

The RF signal received during frequency encoding is then used to fill k-space. Each data point in k-space consists of the summation of MR signals from all voxels in image space under corresponding gradient fields. The inverse Fourier transform of the k-space will generate an image. The signal emitted from a point at a specific time, t is proportional to the spin density and the Larmor frequency ($\omega(r,\tau)$) [19]:

$$S(r,t) = A\rho(r)e^{i\int_o^t \omega(r,\tau)d\tau} \tag{2.12}$$

Therefore:

$$S(t) = A \iiint_V \rho(\vec{r})e^{i\int_o^t \omega(r,\tau)d\tau}dxdydz \tag{2.13}$$

where S is signal and A is an unknown constant. The Larmor frequency is related to gradient fields (G_x, G_y, and G_z) so the signal can be written as [19]:

$$S(t) = A \iiint_V \rho(\vec{r})e^{-i\gamma\int_o^t \vec{r}.G(\vec{\tau})d\tau}dxdydz \tag{2.14}$$

where $G(\vec{\tau}) = G_x(\tau)\vec{i} + G_y(\tau)\vec{j} + G_z(\tau)\vec{k}$ and $\vec{r} = x\vec{i} + y\vec{j} + z\vec{k}$. Now let:

$$k(\vec{t}) = \frac{\gamma}{2\pi}\int_o^t G(\vec{\tau})d\tau \tag{2.15}$$

So that Eq. (2.15) becomes:

$$S(t) = A \iiint_V \rho(\vec{r})e^{-2\pi i\vec{r}.k(\vec{t})}dxdydz \tag{2.16}$$

where $k(\vec{t})$ is the spatial frequency. k-space is the space of spatial frequencies in which the x axis representing the frequency encoding (k_x), the y axis representing the phase encoding value (k_y) and the z axis representing the slice selection value (k_z) [19].

The value of the received signal which is realized as an induced voltage in the receive coil is recorded in the corresponding position in the k-space map according to the k_x, k_y

and k_z values [20]. An image with pixel values that show the amplitude of the signal with a specific phase and frequency will be created after applying an inverse Fourier Transform to the k-space data.

Non-linear : Linear gradient coils generate spatially linearly varying fields which leads to a direct mapping between the local resonance frequency and k-space data. Therefore, the image can be reconstructed using Fourier transform without distortion. However, peripheral nerve stimulation increases with the local rate of change of the magnetic field [21, 22] which results in development of arbitrary coil shapes to generate non-linear gradient field [23, 24, 25]. One of this non-linear spatial encoding methods is PatLoc (Parallel imaging Technique with LOCalized gradients) which uses an arbitrarily shaped non-linear spatial encoding magnetic fields (SEMs) in Parallel imaging [26]. The first PatLoc imaging was performed in a Cartesian acquisition paths. In Cartesian PatLoc, the z gradient is used for slice selection and two non-linear and non-bijective (in bijective, there is a one-to-one correlation between the frequency domain and the location in space) SEMs (NB-SEMs) were used for encoding in other 2 directions. For image reconstruction, 2D Fourier transform was used to transform the k-space data in each RF coil channel to the curvilinear encoding space which resulted in distorted images. Then an unwrapping procedure using RF coils needs to be done, because the mapping from image space to encoding space is non-bijective. For more details, see reference [26]. To decrease the Gibbs artifacts in Cartesian PatLoc, PatLoc imaging was performed in radial acquisition schemes. The image reconstruction for radial PatLoc is performed by using a Filtered back-projection (FBP) followed by using the Cartesian PatLoc reconstruction algorithm. The reconstructed images have some blurring and ringing artifacts at the center due to lack of encoding information from both the gradient system and the RF sensitivity.

The curvilinear SEMs was combined with linear SEMs to reduce ringing artifact in O-space imaging [27] and 4D-RIO [28]. In O-space imaging different SEM shapes (an array of surface coils) were used to optimize parallel imaging performance. Image reconstruction in O-space is performed by directly solving the matrix equation using the Kaczmarz iterative projection algorithm [27]. COGNAC (Combination Of arbitrary Gradient encoding fields using SPACE RIP for reconstruction) is another method that uses both conventional gradients and the spatial information of the underlying receiver coil array to encode information and is more robust to systematic calibration errors. Image reconstruction in COGNAC is performed by inverting the encoding matrix which includes both coil sensitivity profile and gradient encoding using a method called SPACE RIP [29]. There are other more general approaches which SEM shapes are designed from the coil sensitivity profile of a specific surface coil array, such as Null Space Imaging [30, 31]. Using receiver coil sensitivity profiles to perform spatial encoding in parallel imaging is a growing area of research [32, 33, 34, 35, 36].

Spatial Encoding without B_0 Gradient Coils

Gradient coils have different parts such as a power supply, air and water cooling systems, filters, and cables. Hence, by eliminating the gradient coil subsystems, a portion of MRI costs related to installation, operating and maintenance will be eliminated [11]. There are few imaging techniques which use different methods to encode spatial information instead of magnetic gradient coils which would list them here and then discuss.

B_1 Magnitude Gradient : There are different methods which use the magnitude gradient of the B_1 field to encode information:

1. *Rotating Frame Imaging*: In rotating frame imaging technique, the amplitude of B_1 field is used to encode spatial information instead of the B_0 gradient coils [37, 38]. However the method requires high RF power, because it depends on large flip angle pulses. Also since this method collects only a single data point in each excitation, the imaging speed is slow [37, 39, 40]. Therefore, rotating frame imaging has not made its way to clinical imaging [41]. The image reconstruction in this method was performed with Fourier transform when a linear B_1 gradient was used to encode information [37] and with solving the matrix of equation when a non-linear B_1 gradient was used to encode information [39].

2. *Bloch-Siegert (BS)*: BS spatial encoding technique (BS-SET) uses an inhomogeneous B_1 field to generate a spatially varying phase shift to encode spatial information [42], therefore there is no need for gradient coils. However, the method needs a homogeneous B_0 field. Kartausch et.al [42] used a BS-SET method to encode information in 1D and the B_0 gradient coils for the other direction. They then reconstructed images using an analytic Fourier method by rearranging the encoding equation to include the non-linearity [42, 43]. BS-SET method was used for encoding information without the need for B_0 gradient coils using multiple RF coils. This encoding was non-linear and the images were reconstructed using Kaczmarz algorithm to solve the matrix of equations [44].

B_1 Phase Gradient : There are different methods which use the phase gradient of the B_1 field to encode information:

1. *TRansmit Array Spatial Encoding (TRASE)*: TRASE is an imaging technique which uses linear RF phase gradients instead of magnetic field gradients to encode spatial

information [5]. An ideal TRASE coil has to create a B_1 field with uniform magnitude and linearly spatially varying phase to be able to generate the desired image. With B_0 in the z direction, and with i, j, k being unit vectors in the x, y, and z directions, respectively, linear RF phase gradient coils produce the following fields:

$$\vec{B}_1 = \|\vec{B}_1\| \left(\cos(G_x x + \phi_0)\vec{i} + \sin(G_x x + \phi_0)\vec{j}\right) - x \text{ direction encoding field} \quad (2.17)$$

$$\vec{B}_1 = \|\vec{B}_1\| \left(\cos(G_y y + \phi_0)\vec{i} + \sin(G_y y + \phi_0)\vec{j}\right) - y \text{ direction encoding field.} \quad (2.18)$$

$$\vec{B}_1 = \|\vec{B}_1\| \left(\cos(G_z z + \phi_0)\vec{i} + \sin(G_z z + \phi_0)\vec{j}\right) - z \text{ direction encoding field} \quad (2.19)$$

where $\|\vec{B}_1\|$ is constant. However, an actual TRASE coil creates the desired B_1 field only over a limited spatial region, after some optimization of coil geometry. Image reconstruction in TRASE can be performed by Fourier transform [5]. The design and manufacture of RF coils intended for RF encoding would be simpler if it were not necessary for the phase of the transmitted B_1 field to vary linearly.

2. *Non-linear RF phase encoded MRI*: RF phase encoded MRI uses non-linear RF phase gradients instead of magnetic field gradients to encode spatial information. To produce an RF phase gradient, a combination of Maxwell and Helmhotlz coils can be used which will be discussed in the next chapter. A Helmholtz coil has elements in which the current flows in the same direction while a Maxwell coil has elements in which the electrical current flows in opposite directions. The image reconstruction for RF phase encoded MRI can be performed using regularized least squares algorithm to solve the matrix of equations. This method will be discussed in this research.

Inhomogeneous B_0 field : Rotating field MRI uses inhomogeneity of the main magnet field to encode spatial information in the same way as rotating spatial encoding magnetic fields (rSEMs) [45]. In this method, the B_0 magnet and B_0 gradient coils are replaced by a rotating permanent magnet, which eliminates the need for B_0 gradient coils and B_0 field homogeneity requirements. However, rSEMs can do 2D imaging and for encoding information along the axis of rotating magnet another imaging technique is required. A Halbach magnet is used to generate a non-uniform radially varying B_0 field, such that intended image plane is perpendicular to the axis of the magnet. The static field is approximately parabolic inside the rotating MRI which means that the Larmor frequency is a function of radius. To encode information in the angular direction, rotating MRI uses two RF receiver coils which rotate with main field around the sample using a stepper motor (see Figure 2.4).

In this research, we explore the feasibility of reconstructing images from non-linear RF phase encoded MRI signals. This part of the research is a simulation study. However, in order to show the accuracy of the reconstruction method, we applied this method on a portable MRI with rotating fields.

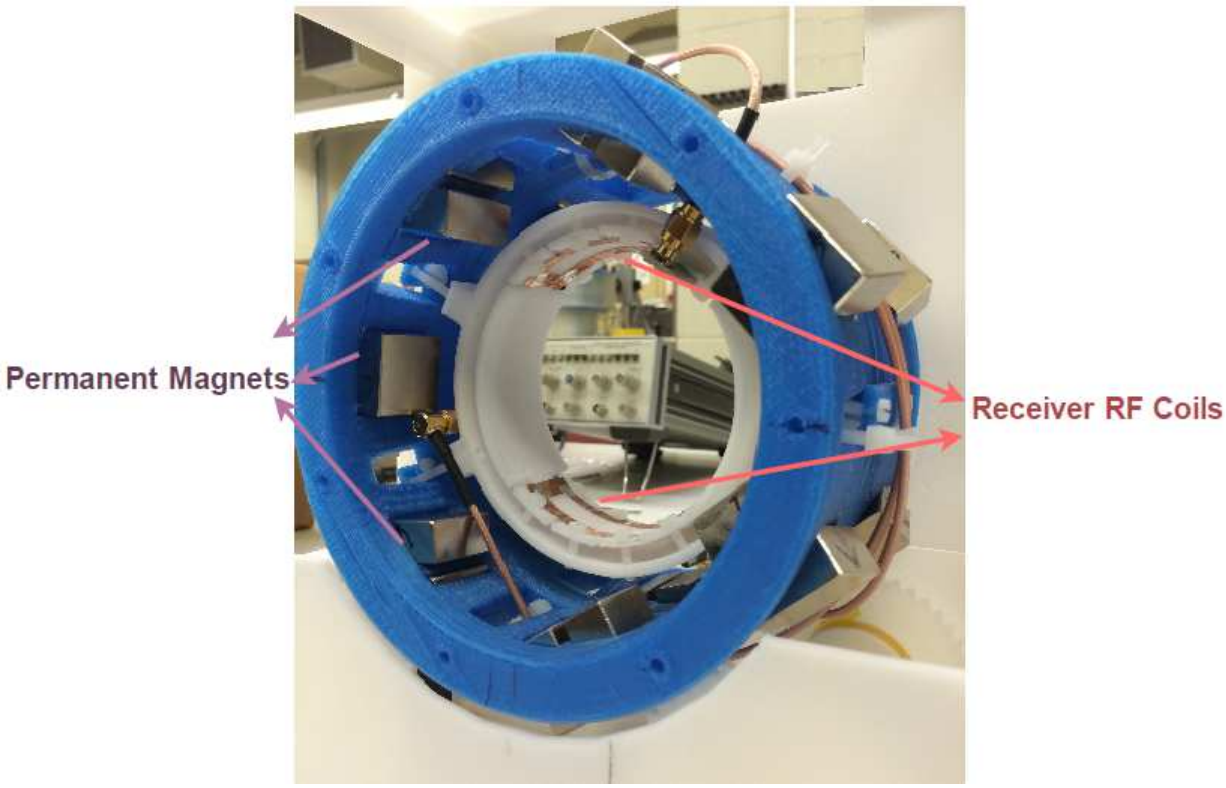

Figure 2.4: This figure shows the main magnet and receiver coils of a rotating field MRI. The rotating field MRI was built in LT imaging Company. The average strength of the main magnet is 0.08 T. The Rotating MRI composed of Halbach magnet and two separate saddle receiver coils located 180^0 from each other. The receiver coils are fixed relative to the magnet and both are rotated around the imaged object.

Chapter 3

RF Phase Encoded MRI

3.1 Introduction

The RF encoding method dispenses with electromagnetic B_0 gradient coils and relies on RF phase encoding within a uniform B_0 field. The original approach to RF encoding in MRI, TRASE, encodes spatial information through the use of a linear spatially varying B_1 transmit phase [5]. With RF encoding, it is possible to eliminate the traditional B_0 gradient coil systems and their associated power supply, air and water cooling systems, filters and cables. By eliminating the gradient coil subsystems, a significant fraction of MRI costs related to installation, operation and maintenance can be eliminated [11].

A linear TRASE coil can create a B_1 field with a uniform magnitude and linearly varying spatial phase only over a limited spatial region [46], after some optimization of coil geometry. The design and manufacture of RF coils intended for RF encoding could be simplified if it were not necessary for the phase of the transmitted B_1 field to vary linearly. In this chapter, we explore simple RF coil configurations for each direction which generate an RF phase gradient field in that direction. The B_1 field is also simulated for each non-linear RF phase encoded coil using the Biot-Savart Law, Eq. (3.2). The appropriate RF pulse sequences for non-linear RF phase encoded coils are presented.

3.2 Design of RF Phase Encoded Coils

To produce an RF phase gradient in the x direction, the Maxwell coil axis should be oriented in the x direction and the Helmholtz coil axis in the y direction. An RF phase gradient in y direction can be obtained by electrically switching the Maxwell and Helmholtz coil axes. These two pairs are orthogonal to each other [5]. Producing spatially varying RF phase in z direction is possible in two ways: (a) using three pairs of Helmholtz coils which have different sizes and the same volume between their elements [5]. The large pair is concentric with x axis and the two small pairs are parallel and with the same space from y axis (above and below of y axis). The two elements of the small pairs are coplanar and non overlapping. The current in small Helmholtz pairs flows in opposite directions (see Figure 3.1), (b) using a spiral birdcage coil (see Figure 3.2). In a twisted birdcage coil there are N equidistant line currents which have a helical shape on a cylindrical surface of radius r. The line currents have different currents which are defined as:

$$I_n = I_0 \sin\left[\frac{2\pi(n-1)}{N}\right] \tag{3.1}$$

where $1 \leq n \leq N$ is the number of the conductors.

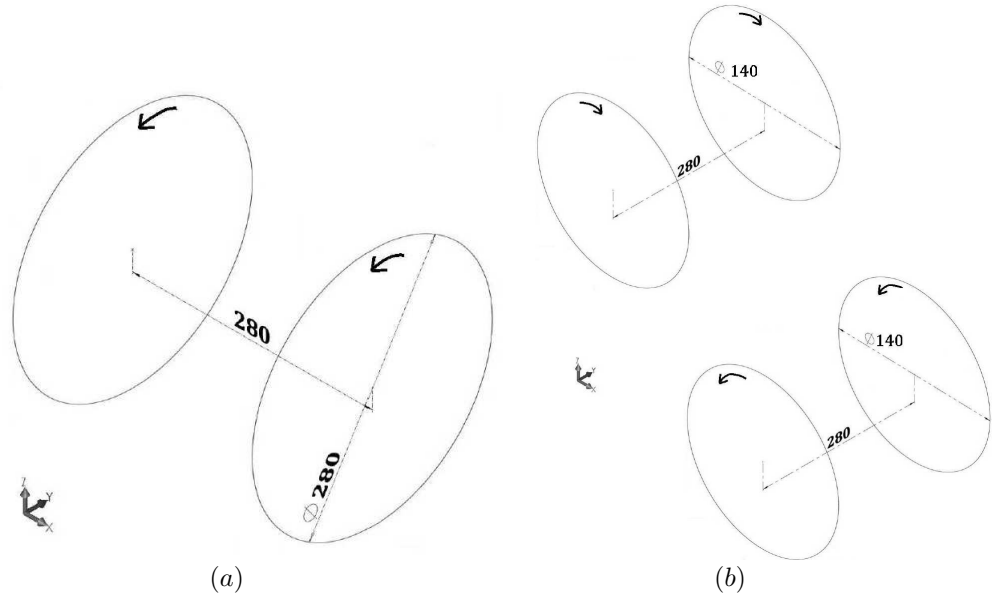

Figure 3.1: Spatially varying RF phase in the z direction.(a) shows the large pair which is concentric with the x axis. The radius of each loop is 140 mm and the distance between the loops is 280 mm. (b) shows the two small pairs which are parallel and with the same space from the y axis (above and below of y axis). The radius of each loop is 70 mm and the distance between the loops is 280 mm. Dimensions in mm are shown.

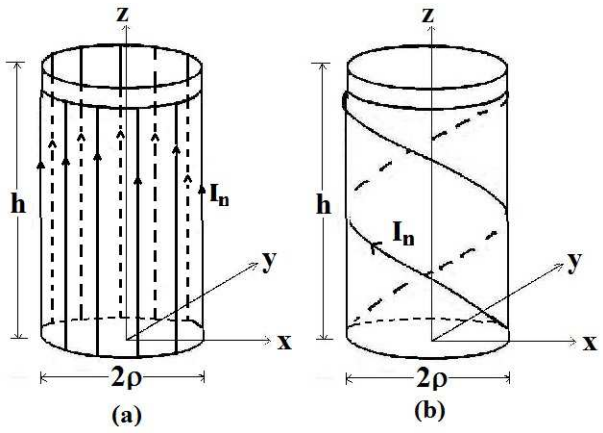

Figure 3.2: Spatially varying RF phase in the z direction using spiral birdcage. (a) Conventional bird cage coil (b) Twisted bird cage coil, h is the birdcage coil's height, ρ is its radius, I_n is the amount of current in each conductors and x, y , z are Cartesian coordinates. The spiral birdcage coil is similar to a traditional one but with helical conductors instead of straight ones. There are N equidistant line currents which have helical shapes on a cylindrical surface of radius ρ.

Here we assume that we are working with an excited slice (the z direction encoding field may be used for slice selection, for example) and focus on encoding and reconstructing an image in the $z = 0$, x–y plane using the x and y encoding fields. There are various ways to create a spatially varying RF phase. Here, four different RF coil configurations are explored: (a) A "circular coil set" composed of a combination of circular Maxwell and Helmholtz coils (Figure 3.3); (b) A "square coil set" composed of a combination of square Maxwell and Helmholtz coils (Figure 3.4); (c) A "parallel conductor coil set" composed of a curved Helmholtz and a double Maxwell coil that follows an optimized TRASE coil as designed by Deng et al. (Figure 3.5) [11] and; (d) A "linear coil set" which can create the linear RF encoding B_1 fields of Eqs. (2.17) and (2.18). Eqs. (2.17) – (2.19) can only be satisfied approximately in a limited field of view using currents in essentially one dimensional RF coils, so the linear coil set represents an ideal situation.

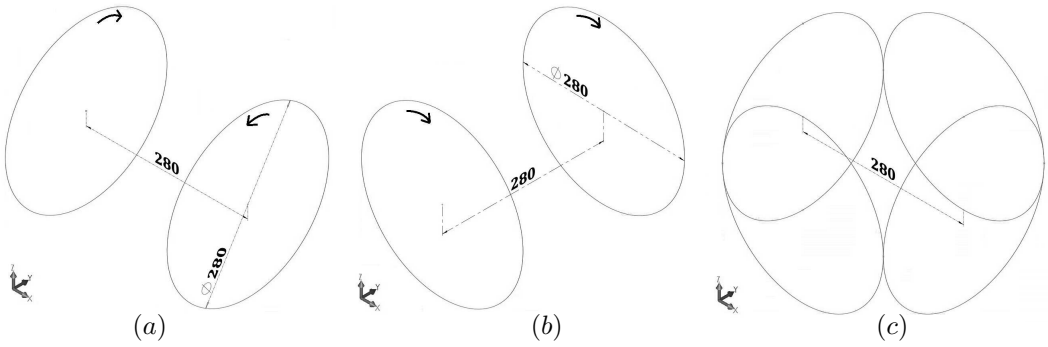

Figure 3.3: The circular coil set. A pair of Maxwell (anti-parallel currents) and Helmholtz (parallel currents) coils, 28 cm in diameter, produce spatial variation of the B_1 phase. The Maxwell coils provide approximations of the sine terms in Eqs. (2.17) and (2.18) while the Helmholtz coils provide approximations for the cosine terms. For producing an RF phase gradient in x direction, the Maxwell coil axis should be placed in x direction and the Helmholtz coil axis should be placed in the y direction. An RF phase gradient in the y direction can be obtained by switching the axis of the Maxwell and Helmholtz coils. This switch may be done by changing the currents in the coils; a physical switch is not necessary. The current magnitude in the Helmholtz and Maxwell coils were set to be equal for the simulations considered here. (a) Maxwell coil for the x direction. (b) Helmholtz coil for the y direction. (c) Complete circular coil set. The radius of the each loop is 140 mm and the distance between the loops is 280 mm. Two physical loop pairs are adequate to provide both x and y direction encoding. Dimensions in mm are shown.

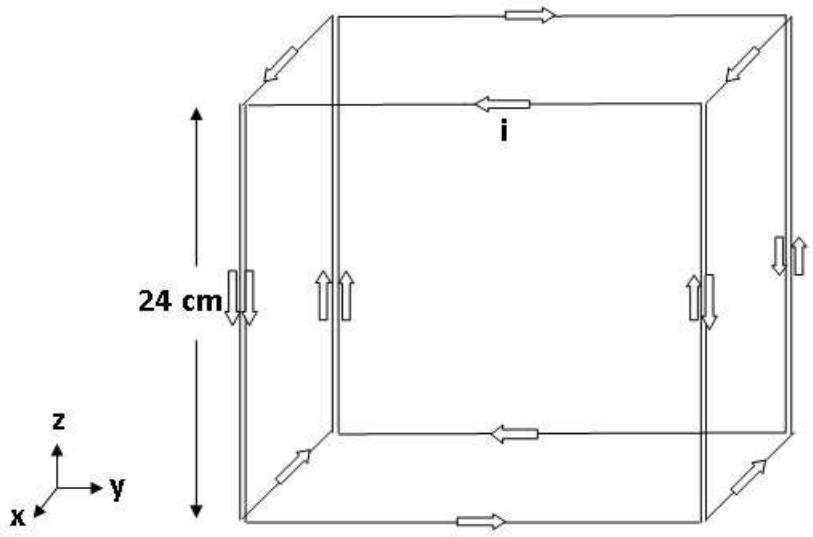

(a)

Figure 3.4: Geometry of the square coil set. The B_0 field is in the z direction. The currents illustrated here show the square coil pair on the x axis as a Maxwell pair and the coil pair on the y axis as a Helmholtz pair. This configuration will produce RF phase gradient in the x direction. An RF phase gradient in the y direction can be obtained by electrically switching the axis of the Maxwell and Helmholtz coils.

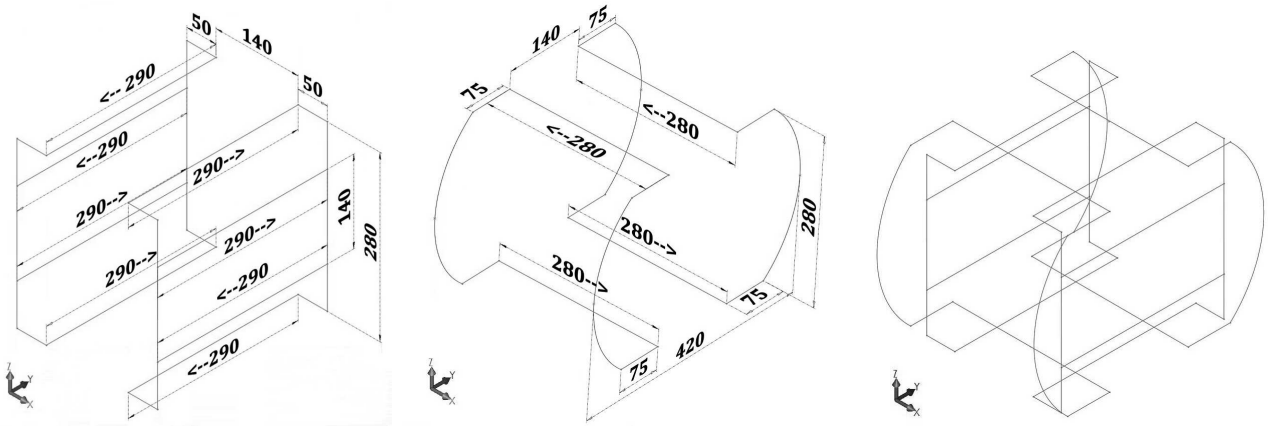

(*a*) (*b*) (*c*)

Figure 3.5: The parallel conductor coil set. Here the circular Maxwell and Helmholtz coils are replaced with parallel conductors, with shielded return paths, carrying anti-parallel ("double Maxwell coil") and parallel currents ("Helmholtz coil") respectively. The anti-parallel currents generate an approximation for the sine terms and the parallel currents generate an approximation for the cosine terms in Eqs. (2.17) and (2.18). The ratio of current in two external lines of the double Maxwell coil to the two internal lines of the double Maxwell coil and to the Helmholtz coil lines were taken as 1.4, 0.2 and 0.85 respectively. (a) Double Maxwell coil with current in conductors parallel to y direction. (b) Helmholtz coil with current in conductors parallel to x direction. (c) The complete parallel conductor coil set for x direction RF phase gradients. Rotating the coil set by 90° produces phase variation in at the y direction. Dimensions in mm are shown.

3.3 RF Field Calculation

Portable MRI systems are likely to be low magnet strength, for example TRASE has been implemented in a B_0 field of 0.2 T [5]. At such low field strengths, the coil tissue interactions are negligible because the RF coils are small compared to the wavelength of the RF field inside the biological tissue [47]. Therefore an *a priori* field map can be used in the image reconstruction algorithm. Also at low field a quasistatic field approximation can be used to calculate the B_1 field because the RF frequency will be low (8.5 MHz at 0.2 T). In other words, the B_1 field may be calculated following Biot-Savart's Law [48]. The Biot-Savart Law is:

$$\vec{B}_1(\vec{r}) = \frac{\mu_0 I}{4\pi} \int_C \frac{\vec{r'}(\ \vec{l}\ ) \times \vec{R}(\vec{r},\ \vec{l}\ )}{\|\vec{R}(\vec{r},\ \vec{l}\ )\|^3}\, d\vec{l} \tag{3.2}$$

where μ_0 is the magnetic permeability of the free space, I is a constant electric current in C, C being a closed contour of current wires, $\vec{l}$ is tangent to C, $\vec{R}(\vec{r},\ \vec{l}\ ) = \vec{r} - \vec{r'}(\ \vec{l}\ )$, and $\vec{r}$ is the position of the observation point (note, $\vec{r} \notin C, \vec{r'} \in C$). Using the appropriate C and I for the circular coil set and the parallel conductor coil set, B_1 was computed using Eq. (3.2). For the linear coil set B_1 is given by Eqs. (2.17) and (2.18). The phase of the B_1 field was made to vary linearly for the linear coil set with $G_x = G_y = 7.20$ deg/cm.

Figure 3.6 shows the variation of the difference between the actual phase of the B_1 field from the ideal phase in each position for the circular coil set. The variation of the phase of B_1 field is not linear, therefore the phase gradient is not constant over a field of view (FOV) of 16 cm $\times$ 16 cm. The phase gradient is 6.03 deg/cm at the center and 4.09 deg/cm at the edge of the FOV with an average of 5.42 deg/cm over the FOV.

Figure 3.7 shows the variation of the difference between actual phase of the B_1 field from

the ideal phase in each position for the square coil set. The phase gradient of B_1 field is not constant over a FOV of 16 cm $\times$ 16 cm. The phase gradient is 5.17 deg/cm at the center and 4.12 deg/cm at the edge of the FOV with an average of 4.86 deg/cm over the FOV.

Figure 3.8 shows the variation of the difference between actual phase of the B_1 field from the ideal phase in each position for the parallel conductor coil set. The phase gradient of B_1 field is not constant over a FOV of 14 cm $\times$ 14 cm. The phase gradient is 7.35 deg/cm at the center and 5.59 deg/cm at the edge of the FOV with an average of 6.68 deg/cm over the FOV.

The spatial phase variation of the B_1 field for the parallel conductor, square coil sets and circular coil sets was close to linear in the center and the magnitude of the B_1 field was uniform in the center as well, but the deviation from linearity and uniformity was considerable at the edges. The largest change in gradient for the circular coil set over the dimensions of the phantom FOV of 16 cm $\times$ 16 cm was approximately 47 percent of the average at the edge of the FOV (see Figure 3.6). The largest change in gradient for the square coil set over the dimensions of the phantom FOV of 16 cm $\times$ 16 cm was approximately 45 percent of the average at the edge of the FOV (see Figure 3.7). The largest change in gradient for the parallel conductor coil set over the dimensions of the phantom FOV of 14 cm $\times$ 14 cm was approximately 13 percent of the average at the edge of the FOV (see Figure 3.8).

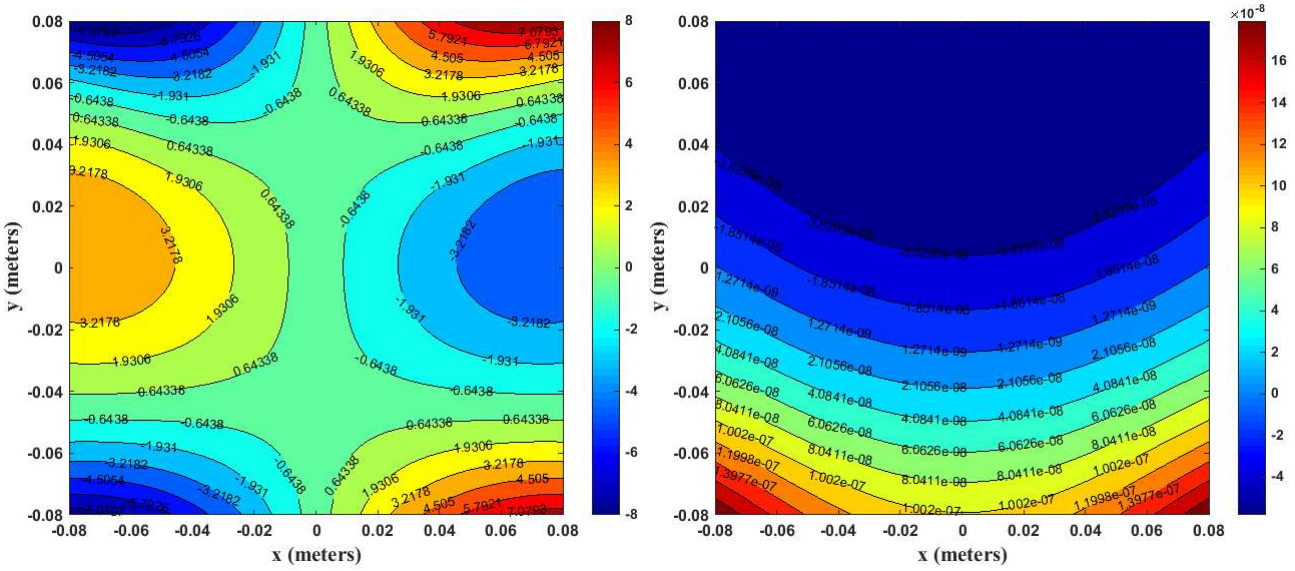

(a) (b)

Figure 3.6: The variation of the actual B_1 phase and magnitude from the ideal ones for the circular coil set are shown in this figure. (a) shows the difference between the actual phase and the ideal one, $\phi(x, y) - G \times x$ (in degree), where $\phi(x, y)$ is the phase of the B_1 field for the x encoding in each position and G is the RF phase gradient in deg/m. (b) shows the difference between the actual magnitude and the ideal one $B_1(x, y) - B_{1_{av}}$ (in Tesla), where $B_1(x, y)$ is the magnitude of B_1 field in each position and $B_{1_{av}}$ is the average of the magnitude of the B_1 field.

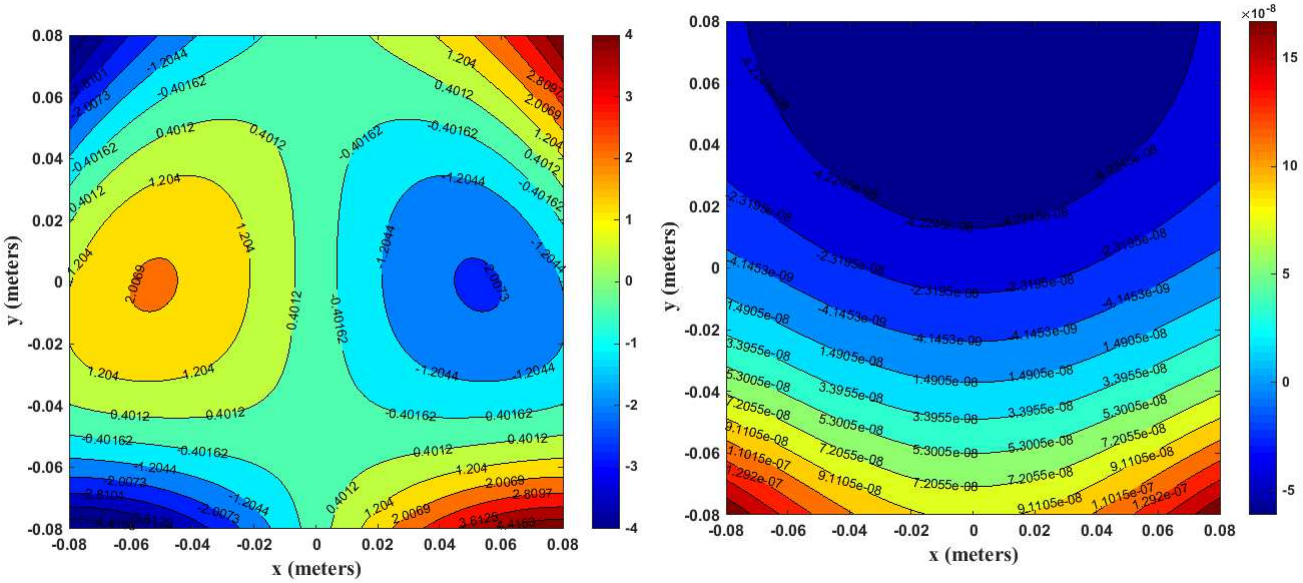

(*a*) (*b*)

Figure 3.7: The variation of the actual B_1 phase and magnitude from the ideal ones for the square coil set are shown in this figure. (a) shows the difference between the actual phase and the ideal one, $\phi(x,y) - G \times x$ (in degree), where $\phi(x,y)$ is the phase of the B_1 field for the x encoding in each position and G is the RF phase gradient in deg/m. (b) shows the difference between the actual magnitude and the ideal one $B_1(x,y) - B_{1_{av}}$ (in Tesla), where $B_1(x,y)$ is the magnitude of B_1 field in each position and $B_{1_{av}}$ is the average of the magnitude of the B_1 field.

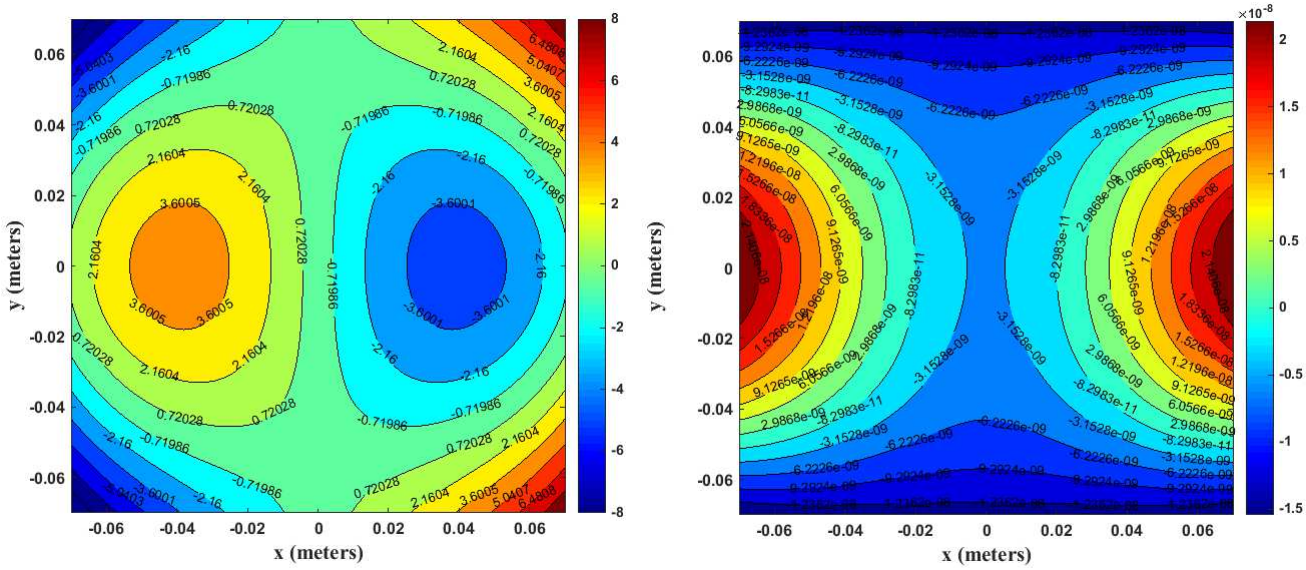

(*a*) (*b*)

Figure 3.8: The variation of the actual B_1 phase and magnitude from the ideal ones for the parallel conductor coil set are shown in this figure. (a) shows the difference between the actual phase and the ideal one, $\phi(x, y) - G \times x$ (in degree), where $\phi(x, y)$ is the phase of the B_1 field for the x encoding in each position and G is the RF phase gradient in deg/m. (b) shows the difference between the actual magnitude and the ideal one $B_1(x, y) - B_{1_{av}}$ (in Tesla), where $B_1(x, y)$ is the magnitude of B_1 field in each position and $B_{1_{av}}$ is the average of the magnitude of the B_1 field.

3.4 180^0 pulse with RF phase encoded coil

The excitation (90^0 pulse) is done by an uniform coil, therefore just the effect of a 180° pulse with an RF phase encoded coil will be discussed in this section. After the 90° excitation the magnetization is in the transverse plane, such that $M^- = Me^{i\alpha}$, where α is the initial phase of the magnetization and M^- is the transverse magnetization just before 180°. The 180° pulse is then applied with RF phase encoded field of $B_1 = b_1 e^{i\phi}$, where ϕ is the angle that B_1 makes with the x axis. As can be seen in Figure 3.9 the results of applying a 180° pulse with a RF phase encoded coil is [5]:

$$M^+(\vec{r}) = \overline{M^-(\vec{r})}\ \ e^{i2\Phi(\vec{r})}. \tag{3.3}$$

where $\overline{M}$ is the complex conjugate of M.

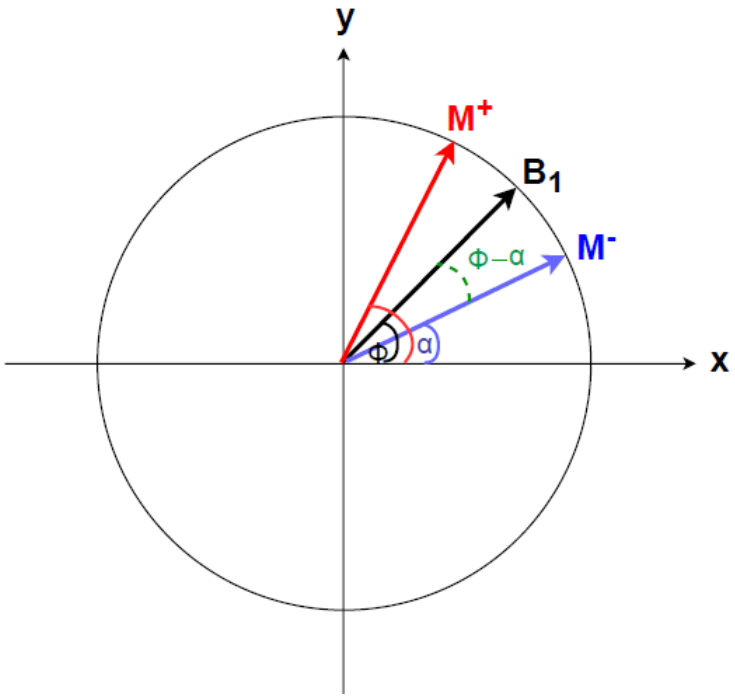

Figure 3.9: A 180° pulse using an RF phase encoded coil will rotate M^-, 180° about the B_1 vector. This rotation will transfer M^- to M^+. The angle that M^+ makes with the axis x is $2\phi - \alpha$; therefore, $M^+ = Me^{i(2\phi-\alpha)} = Me^{-i\alpha}e^{i2\phi}$.

3.5 Pulse Sequences

At least two RF coils (one has to be RF phase gradient coil which has a different spatial phase distribution over the desired sample) are required to move through 1D in k-space. The difference between the spatial derivatives ($G_i = \frac{d\theta_i}{dx}$) of the spatial phase distribution of two B_1 fields is called a gradient difference field ($G1_1$, which ideally should be constant) causes a step through k-space in the encoding direction [5, 11]. Differences between the phase gradients control step size in k-space, hence the step size can be controlled by choosing phase distribution of B_1 fields [5]. For 2D k-space traversal another B_1 field is necessary with a continuous spatial phase distribution along a second direction [5]. By adding other B_1 fields that vary in different directions, moving through k-space in several directions is possible [5].

The basic RF encoding sequence, as we use it here, consists of a 90° RF excitation pulse from a uniform coil (no spatial RF phase variation) followed by a train of 180° pulses made through appropriate RF encoding coils (having spatial RF phase variation). Between the 180° pulses, read out of the echo is made through uniform receiver coils giving one data point (which may be the average of several points from the ADC). Prior to, or included with, the first 90° pulse of the RF encoding sequence, a traditional spin preparation pulse such as a 90° – 180° spin echo preparation may be done to obtain the desired spin relaxation image contrast.

To encode $N + 1$ points in the x direction, we may use a pulse sequence composed of alternating blocks of 180_{+x} and 180_{-x} pulses, to maximize resolution, or we may use a pulse sequence composed of alternating blocks of 180_x and 180_U pulses, to maximize field of view. The 180_x and 180_U denote 180° tip angle excitation with the x direction RF encoding coil and uniform coils respectively. Here we use alternating 180_x and 180_U pulses to explore wider

regions of B_1 inside the coils (see Figure 3.10)

$$90_U - S_0 - \cdots - [180_x - S_{2b-1} - 180_U - S_{2b}]_b - \cdots - [180_x - S_{N-1} - 180_U - S_N]_{N/2} \quad (3.4)$$

where S_n denotes the read out of the n^{th} echo (data point n) and 90_U denotes a 90° tip angle excitation with a uniform coil. For a linear spatial phase gradient this sequence will acquire data on a uniform grid in k-space along the k_x axis. The ideal linear RF encoding coil will have a "k-space origin" giving a fixed Δk_x [5] and the k-space coordinates of the points from the above sequence will be as follows: S_0 will be located at $k_x = 0$, S_{2b-1} will be located at $k_x = -b\Delta k_x$ and S_{2b} will be located at $k = b\Delta k_x$. With non-linear spatial RF phase gradients it is not possible to assign a k-space location to the data points however, to introduce the RF encoding concept, we will assume ideal linear B_1 spatial phase gradients as we complete the description of RF encoding here.

RF pulse sequence:

$$90_U - S_1 - 180_x - S_2 - 180_U - S_3 - 180_x - S_4 - 180_U - S_5$$

k-space positions:

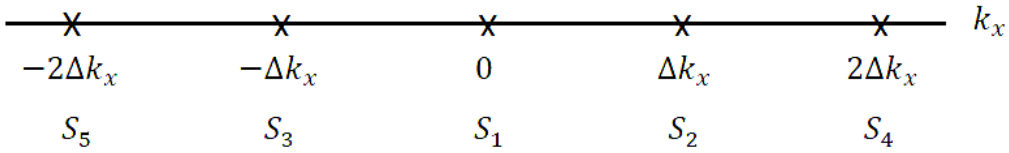

Figure 3.10: One dimension RF encoding sequence consists of a 90^0 RF excitation pulse from a uniform coil followed by a train of 180^0 pulses made through appropriate RF encoding coils. Between the 180^0 pulses, read out of the echo is made (M) through uniform receiver coils giving data points of a, b, c, d, and e. The corresponding positions of a, b, c, d, and e in k-space have been shown.

Define $B_1 \in \mathbb{C}$ (complex) as $B_1 = B_x + iB_y$ for $\vec{B}_1 = B_x\vec{i} + B_y\vec{j} + B_z\vec{k}$ so that

$$B_1(\vec{r}) = |B_1(\vec{r})| \; e^{i\Phi_c(\vec{r})} \quad (3.5)$$

where $\vec{r} = x\vec{i} + y\vec{j} + x\vec{k}$. For the uniform coil, $\Phi_c(\vec{r}) = \Phi_U = 0$, for the linear x encoding coil described by Eq. (2.17), $\Phi_c(\vec{r}) = \Phi_x(x) = G_x x$ and for the linear y encoding coil described by Eq. (2.18), $\Phi_c(\vec{r}) = \Phi_y(y) = G_y y$. In general, the magnitude of B_1 will not be constant so not all spins will experience exact 180° flips; this will lead to diminishing transverse magnetization on top of T_2 decay and to the introduction of artifacts if the echo train is long enough. Hard B_1 pulses with short durations will minimize the problems produced by inhomogeneous B_1 transmit magnitude and inhomogeneous B_0. Let M be the transverse magnetization after the first 90° pulse and label the phase of the transverse magnetization at measurement S_n as Φ_n, then the transverse magnetization, M_n during measurement n may be written:

$$M_n(\vec{r}) = M(\vec{r})\ e^{i\Phi_{x,n}(\vec{r})}. \tag{3.6}$$

Using the phases implied by the x encoding sequence Eq. (3.4) in Eq. (3.3) and unwrapping the measurement phases given by Eq. (3.6) leads to:

$$\Phi_{x,0} = 0,\ \cdots, \Phi_{x,2b-1}(\vec{r}) = 2b\Phi_x(x),\ \Phi_{2b}(\vec{r}) = -2b\Phi_x(x),\ \cdots \tag{3.7}$$

or

$$\Phi_{x,0} = 0,\ \cdots, \Phi_{x,2b-1}(\vec{r}) = 2bG_x x,\ \Phi_{2b}(\vec{r}) = -2bG_x x,\ \cdots. \tag{3.8}$$

Setting $\Delta k_x = G_x/\pi$ leads to:

$$\Phi_{x,0} = 0,\ \cdots, \Phi_{x,2b-1}(\vec{r}) = 2\pi b\Delta k_x x,\ \Phi_{x,2b}(\vec{r}) = -2\pi b\Delta k_x x,\ \cdots. \tag{3.9}$$

Therefore, in a uniform B_0 field, signal can be simulated as:

$$S_{2b-1} = \int_{\vec{r}} M(\vec{r})\ e^{2\pi i b\Delta k_x x}\ d\vec{r} \tag{3.10}$$

$$S_{2b} = \int_{\vec{r}} M(\vec{r})\ e^{-2\pi i b\Delta k_x x}\ d\vec{r} \tag{3.11}$$

which are the Fourier transforms of $M(\vec{r})$ at $k_x = -b\Delta k_x$ and $k_x = b\Delta k_x$ respectively.

To encode in the y direction as well as the x direction use:

$$90_U - [180_y - 180_U]^{m/2} - S_0 - \cdots - [180_x - S_{2d-1} - 180_U - S_{2d}]_d - \cdots$$

$$m \geq 0, \text{even} \tag{3.12}$$

$$90_U - 180_y - [180_U - 180_y]^{(m-1)/2} - S_0 - \cdots - [180_x - S_{2d-1} - 180_U - S_{2d}]_d - \cdots$$

$$m \geq 1, \text{odd} \tag{3.13}$$

where the exponent on a block of pulses tells how many times to repeat that block (the subscript on a block is an index as before) and $0 \leq m \leq M$ will give $M+1$ sequences with k_y values of $k_y = -(m-1)\Delta k_y/2$ for m odd and $k_y = m\Delta k_y/2$ for m even if the phase gradients are linear. The transverse magnetization during measurement will be:

$$M_{n,m}(\vec{r}) = M(\vec{r})\ e^{i(\Phi_{x,n}(\vec{r}) + \Phi_{y,m}(\vec{r}))} \tag{3.14}$$

where $\Phi_{x,n}(\vec{r})$ is given by Eqs. (3.7) and [3.8] and

$$\Phi_{y,0} = 0,\ \cdots, \Phi_{y,2d-1}(\vec{r}) = 2d\Phi_y(y),\ \Phi_{y,2d}(\vec{r}) = -2d\Phi_y(y),\ \cdots \tag{3.15}$$

or

$$\Phi_{y,0} = 0,\ \cdots, \Phi_{y,2d-1}(\vec{r}) = 2dG_y y,\ \Phi_{y,2d}(\vec{r}) = -2dG_y y,\ \cdots . \tag{3.16}$$

if the phase gradient is linear. In the linear case the signal points are:

$$S_{2b-1,2d} = \int_{\vec{r}} M(\vec{r})\ e^{-2\pi i(-b\Delta k_x x + d\Delta k_y)}\ d\vec{r} \tag{3.17}$$

$$S_{2b,2d} = \int_{\vec{r}} M(\vec{r})\ e^{-2\pi i(b\Delta k_x x + d\Delta k_y)}\ d\vec{r} \tag{3.18}$$

$$S_{2b-1,2d-1} = \int_{\vec{r}} M(\vec{r})\ e^{-2\pi i(-b\Delta k_x x - d\Delta k_y)}\ d\vec{r} \tag{3.19}$$

$$S_{2b,2d-1} = \int_{\vec{r}} M(\vec{r})\ e^{-2\pi i(b\Delta k_x x - d\Delta k_y)}\ d\vec{r} \tag{3.20}$$

where $\Delta k_y = G_y/\pi$. When the sequences [3.12] and [3.13] are run with non-linear phase gradient RF coils, Eq. (3.3) is still true and

$$S_{n,m} = \int_{\vec{r}} M(\vec{r})\ e^{i(\Phi_{x,n}(\vec{r})+\Phi_{y,m}(\vec{r}))}\ d\vec{r} \tag{3.21}$$

but the data points $S_{n,m}$ will no longer be linearly related to k-space.

To increase k-space density, one can use a second pulse sequence with a different excitation. This method produces points between the points of the first walk, because moving through k-space will start from a different origin [5]. k-space acquisition can be accelerated by using more than one receive coil at the same time [5].

For having a higher resolution, the largest area of k-space with the smallest step size (FOV) should be covered [5]. The RF encoding sequence of Eqs. (3.12, 3.13 and 3.4) trades resolution for FOV. To increase the resolution at the expense of FOV (by increasing the distance between data points in "k-space") the following *high resolution RF encoding sequence* for encoding in x direction can be used:

$$90_U - S_0 - \cdots - [180_x - S_{2b-1} - 180_{-x} - S_{2b}]_b - \cdots - [180_x - S_{N-1} - 180_{-x} - S_N]_{N/2} \tag{3.22}$$

where 180_{-x} denotes 180° tip angle excitation with the $-x$ direction RF encoding coil.

3.6 Signal Simulation and Image Reconstruction

The density of the imaged object and as a phantom is a real quantity which we denote by $\rho(x, y)\ \epsilon\ \mathbb{R}$. Here ρ is assumed to be weighted by spin preparation (e.g. T_1 or T_2 weighting). The measured transverse density will be a complex quantity which we denote by $M(x, y)\ \epsilon\ \mathbb{C}$ and its relation to the desired image density is:

$$M(x, y) = A(x, y)\rho(x, y)\ e^{i\phi(x,y)} \tag{3.23}$$

where the real and imaginary parts of M are defined in the transverse plane rotating at the resonant frequency for B_0 and the function A characterizes the gain and uniformity of the receive coil while ϕ characterizes phase of the received signal. For a spatially uniform transmit coil, A is a constant that will not change image contrast so we may assume that $A = 1$. When A is not uniform we can correct for it by dividing the reconstructed image by a function of A (determined by the flip angles achieved). We set $A = 1$. By adjusting the phase of the received RF for example, we may, and will, assume that $\phi = 0$, that is, the first 90_U pulse of the RF encoding sequence is about the rotating frame y axis to the x axis. In other words, we assume that the transverse magnetization represents the phantom, $\rho = M$. Working in the transverse plane, we define $B_1 \in \mathbb{C}$ as in Eq. (3.5). Assuming that slice selection has been accomplished, the ℓ^{th} detected signal (data point) may be modelled as

$$S_\ell(\rho) = \iint \rho(x,y)\, e^{i(\Phi_\ell(x,y)+\gamma n \Delta t \Delta B_0(x,y))}\; dx\, dy \quad + \quad N_\ell. \tag{3.24}$$

where ℓ is a function of the n and m associated with the data points generated by the pulse sequences [3.12] and [3.13]; Φ_ℓ is accumulated phase and is associated with the 180° pulse immediately proceeding the data point acquisition as per Eq. (3.14) with $\Phi_\ell(x,y) = \Phi_{x,n}(x,y) + \Phi_{y,m}(x,y)$; $N_\ell \in \mathbb{C}$ is Gaussian white noise added in the simulations (will be shown in chapter 4) to give signal to noise ratios (SNR) of ∞ (no noise), 10, 20 or 50 dB in each of the real and imaginary parts and; $\Delta B_0(x,y)$ quantifies main field inhomogeneities. The Biot-Savart law [3.2] was used to compute the B_1 phases of the x and y RF encoding coils, $\Phi_x(x,y)$ and $\Phi_y(x,y)$, so that:

$$\Phi_\ell(x,y) = \Phi_{n,x}(x,y) + \Phi_{m,y}(x,y) \tag{3.25}$$

for $0 \leq \ell \leq L = NM$, $0 \leq n \leq N$ and $0 \leq m \leq M$. A Riemann sum approximation of Eq. (3.24) can be used to compute the simulated signal:

$$S_\ell(\rho) = \sum_{i=0}^{I-1} \sum_{j=0}^{J-1} \rho(x_i, y_j) \; e^{i(\Phi_\ell(x_i,y_j)+\gamma n \Delta t \Delta B_0(x,y))} \quad + \quad N_\ell \tag{3.26}$$

where we have set $\Delta x \Delta y = 1$ because a multiplicative constant does not affect the image contrast.

For the linear coil sets the image can be reconstructed by using Fourier transforms. For the other types of coil sets Fourier transforms may lead to a distorted image, because the phase of B_1 field varies non-linearly with the position. Therefore the least squares method has been used in case of non-linear phase. The reconstruction methods will be briefly discussed in the next chapter.

Chapter 4

Image Reconstruction of RF Phase Encoded Data

4.1 Introduction

B_0 gradient coils are engineered to generate linear magnetic field gradients over a suitable FOV in the magnet bore with the result that the image can be reconstructed from the NMR signal through the use of Fourier transform techniques. Non-linear magnetic field gradients have been introduced in an effort to achieve faster imaging times without inducing painful nerve stimulation. These spatial encoding magnetic field (SEM) methods include the parallel imaging technique using local gradients (PatLoc) approach [24, 28], the O-Space approach [27] and, methods that use combined linear and non-linear approaches [49, 50, 51]. In the extreme, specially engineered electromagnetic B_0 gradient coils are dispensed with entirely and the native B_0 profile of a given inhomogeneous magnet is used for SEM in portable MRI designs [45]. All of these new approaches require a modification of the Fourier transform reconstruction approach [52, 53] or alternative approaches with generalized projections [54, 55]. In these more generalized circumstances, a least squares approach is one of the more straight-forward ones useful for image reconstruction [45].

Similar to data acquired using B_0 gradients, the imaging data generated with a TRASE coil may be reconstructed, generally after data reordering, via a Fourier transform [12, 19]. The TRASE coil creates a B_1 field with a uniform magnitude and linearly varying spatial

phase. However, the RF coils discussed in chapter 3 generate a non-linear RF phase gradient which can not be reconstructed simply with Fourier transform. In this chapter we explore the feasibility of reconstructing non-linear RF encoded signals from a mathematical perspective.

Considered mathematically, the MRI signal dataset is the result of a signal function from the image domain, here considered as a discrete lattice, to a signal range which in the case of RF encoding may be parametrized by echo number and echo train number. (RF encoded data consist of a number of separate echo trains, with a T_R spacing between them.) In the case of linear B_1 spatial phase variation, as with linear B_0 gradients, the signal function is linear (a Fourier transform). If the signal function is non-linear it is still, in principle, invertible as long as the map is one-to-one. However, the inversion problem may be ill-posed or close to ill-posed, especially when noise and/or non-uniform B_0 fields are present. Ill-posed inversion problems may be handled to a certain extent by regularization methods [56] such as the Tikhonov [57] or maximum entropy methods [58, 59]. These regularization methods are examples of constrained least squares methods and they require the selection of a suitable regularization parameter [60, 61, 62].

Here we show that least squares inversion [63, 64, 65] without regularization may be used to reconstruct noiseless RF encoded data obtained using simple, realistic, non-linear RF encoding coils. The inversion is, however, sensitive to noise so we show that Tikhonov regularization can be added to obtain a stable solution. In this chapter the images were reconstructed for each of the three coil configurations, linear, parallel conductor coil set and circular coil set. The result for the square coil is given in the next chapter.

4.2 Theory

4.2.1 Fourier Image Reconstruction

Linear RF Phase Encoded Data

For the numerical experiments reported here, a mathematical phantom ρ was discretized and a Riemann sum approximation of Eq. (3.24) was used to compute the simulated signal (see Eq. (3.26)). In the simulations here we set $\Delta B_0 = 0$ in Eq. (3.26), in order to focus on the effects of B_1 variation. Also, known ΔB_0 may be corrected by including it in the encoding $[T]$ matrix of Eq. (4.14) given below and the effect of unknown ΔB_0 may be modified by changing the length, N, of the individual pulse sequences. For the linear coil set the noiseless simulated signal data are

$$S_{\ell(n,m)}(\rho) \;=\; \sum_{i=0}^{I-1}\sum_{j=0}^{J-1} \rho(x_i, y_j)\;\; e^{-2\pi i[n\Delta k_x x_i + m\Delta k_y y_j]} \tag{4.1}$$

where $-N/2 \le n \le N/2$ and $-M/2 \le m \le M/2$ have been reindexed from the n and m used to index the data points as labeled in the sequences [3.12] and [3.13]. If we promote the discrete function $\rho(x_i, y_j)$ to a function $\rho(x, y)$ defined on all of $\mathbb{R}^2$ by defining it to be constant on the pixels defined by each $(x_i, y_j) \in [x_i - \Delta x/2, x_i + \Delta x/2] \times [y_j - \Delta y/2, y_j + \Delta y/2]$ then Eq. (4.1) becomes a close approximation of

$$S_{\ell(n,m)}(\rho) = \iint \rho(x, y)\; e^{-2\pi i[n\Delta k_x x + m\Delta k_y y]}\;\; dx\; dy. \tag{4.2}$$

Since we have a finite number of data values, we use a Riemann approximation to the inverse integral Fourier transform (again ignoring the actual value of $\Delta x \Delta y$) to obtain the

reconstructed approximation $P\rho$ of ρ as[1]

$$P\rho(x,y) = \sum_{n=-N/2}^{N/2-1} \sum_{m=-M/2}^{M/2-1} S_{\ell(n,m)}(\rho)\, e^{2\pi i[n\Delta k_x x + m\Delta k_y y]} \tag{4.3}$$

$$= \rho * \phi(x,y) \tag{4.4}$$

where $*$ denotes integral convolution and ϕ is the point spread function (PSF) given in this case by

$$\phi(x,y) = \sum_{n=-N/2}^{N/2-1} \sum_{m=-M/2}^{M/2-1} e^{2\pi i[n\Delta k_x x + m\Delta k_y y]} \tag{4.5}$$

which is the Fourier transform of δ functions on the sampling square grid in k-space. The PSF, ϕ, is a Cartesian product of sinc functions convolved with a grid of δ functions with a spacing of $(1/\Delta k_x, 1/\Delta k_y)$. If $\rho(x,y) = E_{(0,0)}(x,y)$ where $E_{(0,0)}$ is the image basis function that has the value 1 on a pixel centered at $(x,y) = (0,0)$ and 0 everywhere else then $PE_{(0,0)} = \phi$. This characterization of the PSF holds for all linear reconstruction methods and can be used as the definition of a local PSF for non-linear reconstruction methods. That is, we can define $\phi_{(a,b)} = PE_{(a,b)}$. For linear reconstruction the local PSFs are all translations of the global PSF $\phi_{(a,b)}(x,y) = \phi_{(0,0)}(x-a, y-b)$.

Nonlinear RF Phase Encoded Data

The Fourier reconstruction of simulated data from the parallel conductor coil and the circular coil set-ups was done by using Eq. (4.3) with the simulated signal of Eq. (3.26) and assuming the average value of the phase gradient for each configuration.

[1]We find it helpful to explicitly write the reconstruction map P as in $\rho \to P\rho$. With Fourier encoding and reconstruction, P is linear. With the non-linear RF encoding coils P is non-linear.

4.2.2 Iterative Image Reconstruction

Using Encoding Matrix and Image Basis Functions

With realistic RF coils, the circular and parallel conductor coil sets, the phase of the B_1 field does not change linearly with position, so using the discrete Fourier transform (DFT) inverse as per Eq. (4.4) leads to a poor approximation $P\rho$ of ρ. Instead of using the inverse DFT, a more direct least squares reconstruction is possible, with the inverse DFT and least squares reconstruction being equivalent when the phase of B_1 changes linearly with position.

To set up the least squares reconstruction we first apply Eq. (3.26), without noise, to the image basis functions for the given resolution as

$$S_\ell(E_{(x_a,y_b)}) = \sum_{i=0}^{I-1}\sum_{j=0}^{J-1} E_{(x_a,y_b)}(x_i,y_j)e^{i\Phi_\ell(x_i,y_j)} \tag{4.6}$$

where E_{x_a,y_b} is the basis function defined as

$$E_{(x_a,y_b)}(x_i,y_j) = \begin{cases} 1 \text{ if } (x_i,y_j) \in [x_a-\Delta x/2, x_a+\Delta x/2]\times[y_b-\Delta y/2, y_b+\Delta y/2] \\ 0 \text{ otherwise} \end{cases} \tag{4.7}$$

Since

$$\rho(x_i,y_j) = \sum_{a=0}^{I-1}\sum_{b=0}^{J-1} \rho(x_a,y_b)\ \ E_{(x_a,y_b)}(x_i,y_j) \tag{4.8}$$

Eq. (3.26) may be written

$$\begin{aligned} S_\ell(\rho) &= \sum_{i=0}^{I-1}\sum_{j=0}^{J-1}\left(\sum_{a=0}^{I-1}\sum_{b=0}^{J-1}\rho(x_a,y_b)\ \ E_{(x_a,y_b)}(x_i,y_j)\right)e^{i\Phi_\ell(x_i,y_j)} &(4.9)\\ &= \sum_{a=0}^{I-1}\sum_{b=0}^{J-1}\rho(x_a,y_b)\left(\sum_{i=0}^{I-1}\sum_{j=0}^{J-1}E_{(x_a,y_b)}(x_i,y_j)\ \ e^{i\Phi_\ell(x_i,y_j)}\right) &(4.10)\\ &= \sum_{a=0}^{I-1}\sum_{b=0}^{J-1}\rho(x_a,y_b)S_\ell(E_{(x_a,y_b)}) &(4.11)\end{aligned}$$

where we have used Eq. (4.6).

After re-indexing $(0,0) \leq (a,b) \leq (I-1, J-1)$ to $0 \leq q \leq Q = IJ$ by ordering (a,b) lexically, Eq. (4.11) will be

$$S_\ell(\rho) = \sum_{q=0}^{Q} \rho((x,y)_q) S_\ell(E_{((x,y)_q)}) \quad 0 \leq \ell \leq L. \tag{4.12}$$

Let $\vec{S}$ be the L dimensional vector with components $S_\ell(\rho)$, $0 \leq \ell \leq L$. Let $\vec{\rho}$ be the Q dimensional vector with components $\rho((x,y)_q)$, $0 \leq q \leq Q$. And let $[T]$ be the $L \times Q$ dimensional matrix with components

$$T_{\ell,q} = S_\ell(E_{((x,y)_q)}). \tag{4.13}$$

Then Eq. (4.12) becomes

$$\vec{S} = [T]\vec{\rho}. \tag{4.14}$$

The matrix of the desired image can be reconstructed via LS method.

Using Encoding Matrix and Delta Functions

We note that there are other more efficient ways to compute a useful encoding matrix $[T]$, however the end result of the reconstruction will be similar to the results given here. For example, a least squares reconstruction method may be set up that involves the inversion of an encoding matrix [28, 50, 51, 45, 27, 52, 54] which may be defined as:

$$\mathcal{E}_\ell(x_i, y_j) = e^{i\Phi_\ell(x_i, y_j)} \tag{4.15}$$

The simulated signal can be written as the projection of the magnetization onto these encoding functions as:

$$S_\ell(\rho) = \sum_{i=0}^{M-1} \sum_{j=0}^{N-1} \rho(x_i, y_j) \;\; \mathcal{E}_\ell(x_i, y_j) \tag{4.16}$$

which would replace Eq. (4.9). With reindexing we have:

$$\vec{S} = [\mathcal{E}]\vec{\rho}. \tag{4.17}$$

in place of Eq. (4.14) which may be inverted using the LS method described here.

Least Squares method and Tikhonov Regularization

The least squares (LS) solution (without regularization) of Eq. (4.14) gives the approximate solution $\vec{R}$ for $\vec{\rho}$ as:

$$\vec{R} = \arg\min \left\| [T]\vec{R} - \vec{S} \right\|^2 \tag{4.18}$$

where $\|\cdot\|$ is the Euclidean vector norm. The LS solution was computed using the built-in solver provided by Matlab (MathWorks, Natick, MA, 2013). The image $P\rho$ is recovered from $\vec{R}$ by reindexing q back to pixel coordinates.

For the RF encoded data with added noise, Tikhonov regularization is added to Eq. (4.18) to give the constrained LS solution

$$\vec{R} = \arg\min \left(\left\| [T]\vec{R} - \vec{S} \right\|^2 + \mu \left\| [I]\vec{R} \right\|^2 \right) \tag{4.19}$$

where $[I]$ is identity matrix and μ is a regularization parameter.

A suitable value for μ was selected according to the approach given in [61, 62]. In this approach the error, η, between the approximate solution and the actual solution is estimated using:

$$\eta^2(\mu) = d_0^2/d_1 \tag{4.20}$$

where $d_0 = \|\vec{r}\|^2$ and $d_1 = \left\| [T]^T\vec{r} \right\|^2$. After substituting d_0 and d_1, the estimated error is:

$$\eta(\mu) = \frac{\|\vec{r}_\mu\|^2}{\|[T]^T\vec{r}_\mu\|} \tag{4.21}$$

where $\vec{r}_\mu = [T](\vec{\rho} - \vec{R}_\mu)$ is the residual vector and $\vec{R}_\mu$ is the solution to Eq. (4.19) for a selected μ in a given grid of μ values.

To find a suitable μ, Lanczos bidiagonalization algorithm (It is explained on page 50 of this thesis.) was used. For each step of Lanczos bidiagonalization, from $\ell = 1$ to $\ell = \ell_{\max}$(user specified), upper (η_u) and lower (η_l) bounds on η were computed using Gauss quadrature rule (It is explained on page 46 of this thesis.) [66] for each μ inside the given grid. Then the smallest j was found such that for $i > j$:

$$|\eta_u(\mu_i) - \eta_l(\mu_i)| < \beta\ \bar{\eta}(\mu_i) \tag{4.22}$$

where β is a tolerance (user specified) and $\bar{\eta}$ is the average of η_l and η_u. Then all μ_i with $i > j$ and their corresponding $\bar{\eta}(\mu_i)$ were saved. For the next step of Lanczos bidiagonalization the above procedure was repeated for all μ_i with $i < j$ until the maximum number of Lanczos bidiagonalization ($\ell_{\max}$) was reached or there is no more μ to continue with. Among the saved $\bar{\eta}(\mu_i)$, the minimum ($\bar{\eta}_{\min}$) and the corresponding $\mu_{\min}$ was then selected. The grid was systematically refined by adding point around the $\mu_{\min}$ using bisection method. For the new values of μ, the corresponding $\bar{\eta}$ were calculated. The minimum value of $\bar{\eta}$ and the corresponding new $\mu_{\min}$ were saved and the procedure was repeated until:

$$|\mu_i - \mu_{i+1}| < \epsilon \tag{4.23}$$

where ϵ is a user specified tolerance. This $\mu_{\min}$ was then as the one recorded to be used in Eq. (4.19).

Upper and lower bounds: It can be seen in Eq. (4.20) that η is computed from d_0 and d_1, therefore the bounds for η can be calculated knowing the lower and upper bounds for d_0 and d_1. Upper and lower bounds for d_0 and d_1 for step ℓ of Lanczos bidiagonalization can be

calculated as [61, 62, 60]:

$$\begin{aligned} \boldsymbol{C_\ell(\phi_\mu)} < d_0(\mu) < \boldsymbol{R_{\ell+1}(\phi_\mu)} \\ \boldsymbol{\hat{C}_\ell(\phi_\mu)} < d_1(\mu) < \boldsymbol{\hat{R}_\ell(\phi_\mu)} \end{aligned} \tag{4.24}$$

where each term of $\boldsymbol{C_\ell(\phi_\mu)}$, $\boldsymbol{R_{\ell+1}(\phi_\mu)}$, $\boldsymbol{\hat{C}_\ell(\phi_\mu)}$ and $\boldsymbol{\hat{R}_\ell(\phi_\mu)}$ will be discussed for a system of $Ax = b$ and a specific μ.

$$\boldsymbol{C_\ell(\phi_\mu)} = \mu^2 \left\|b\right\|^2 e_1^T (C_\ell C_\ell^T + \mu I)^{-2} e_1 \tag{4.25}$$

let $y_l(\mu) = \mu(C_\ell C_\ell^T + \mu I)^{-1} e_1$, so:

$$\boldsymbol{C_\ell(\phi_\mu)} = \left\|b\right\|^2 y_l^T(\mu) y_l(\mu) \tag{4.26}$$

$y_l(\mu)$ can be calculated by the least squares method using QR factorization approach (It is explained on page 51 and 52 of this thesis.):

$$y = \arg\min \left(\left\| \begin{bmatrix} C_l^T \\ \mu^{1/2} I_\ell \end{bmatrix} y - \mu^{1/2} e_{\ell+1} \right\| \right) \tag{4.27}$$

where C_ℓ^T is upper matrix and C_ℓ is defined as:

$$C_\ell = \begin{bmatrix} \rho_1 & & & & & & 0 \\ \sigma_2 & \rho_2 & & & & & \\ & \ddots & \ddots & & & & \\ & & \ddots & \ddots & & & \\ & & & \ddots & \ddots & & \\ & & & & \sigma_{\ell-1} & \rho_{\ell-1} & \\ 0 & & & & & \sigma_\ell & \rho_\ell \end{bmatrix} \tag{4.28}$$

The procedure to calculate σ and ρ will be described in the Lanczos bidiagonalization procedure (It is explained on page 50 of this thesis.).

$$\boldsymbol{R_{\ell+1}(\phi_\mu)} = \mu^2 \left\|b\right\|^2 e_1^T (\bar{C}_\ell \bar{C_\ell}^T + \mu I)^{-2} e_1 \tag{4.29}$$

let $y_l(\mu) = \mu(\bar{C}_\ell \bar{C_\ell}^T + \mu I)^{-1} e_1$, so:

$$\boldsymbol{R_{\ell+1}(\phi_\mu)} = \left\|b\right\|^2 y_l^T(\mu) y_l(\mu) \tag{4.30}$$

Similar to Eq. (4.27), $y_l(\mu)$ can be calculated using least squares method and QR approach:

$$y = \arg\min \left(\left\| \begin{bmatrix} \bar{C_l}^T \\ \mu^{1/2} I_{\ell+1} \end{bmatrix} y - \mu^{1/2} e_{\ell+1} \right\| \right) \tag{4.31}$$

where $\bar{C_\ell}^T$ is upper matrix and $\bar{C}_\ell$ defined as:

$$\bar{C}_\ell = \begin{bmatrix} \rho_1 & & & & & & 0 \\ \sigma_2 & \rho_2 & & & & & \\ & \ddots & \ddots & & & & \\ & & \ddots & \ddots & & & \\ & & & \ddots & \ddots & & \\ & & & & \sigma_{\ell-1} & \rho_{\ell-1} & \\ & & & & & \sigma_\ell & \rho_\ell \\ 0 & & & & & & \sigma_{\ell+1} \end{bmatrix} \tag{4.32}$$

$$\boldsymbol{\hat{C}_\ell(\phi_\mu)} = \mu^2 \left\|A^T b\right\|^2 e_1^T (\hat{C}_\ell \hat{C_\ell}^T + \mu I)^{-2} e_1 \tag{4.33}$$

let $y_l(\mu) = \mu(\hat{C}_\ell \hat{C_\ell}^T + \mu I)^{-1} e_1$, so:

$$\boldsymbol{\hat{C}_\ell(\phi_\mu)} = \left\|A^T b\right\|^2 y_l^T(\mu) y_l(\mu) \tag{4.34}$$

Similar to Eq. (4.27), $y_l(\mu)$ is calculate using the least squares method and QR approach:

$$y = \arg\min \left(\left\| \begin{bmatrix} \hat{C_l}^T \\ \mu^{1/2} I_{\ell+1} \end{bmatrix} y - \mu^{1/2} e_{\ell+1} \right\| \right) \tag{4.35}$$

where $\hat{C_\ell}^T$ is upper matrix and is defined as:

$$\hat{C_\ell}^T = \begin{bmatrix} \delta_1 & \gamma_2 & & & & 0 \\ & \delta_2 & \gamma_3 & & & \\ & & . & . & & \\ & & & . & . & \\ & & & & . & . \\ & & & & \delta_{\ell-1} & \gamma_\ell \\ 0 & & & & & \delta_\ell \end{bmatrix} \tag{4.36}$$

The procedure for calculating δ and γ will utilize Lanczos bidiagonalization procedure.

$$\hat{\boldsymbol{R}}_{\boldsymbol{\ell}}(\boldsymbol{\phi_\mu}) = \mu^2 \left\| A^T b \right\|^2 e_1^T (\bar{\hat{C}}_{\ell-1} \bar{\hat{C}}_{\ell-1}^T + \mu I)^{-2} e_1 \tag{4.37}$$

let $y_l(\mu) = \mu(\bar{\hat{C}}_{\ell-1} \bar{\hat{C}}_{\ell-1}^T + \mu I)^{-1} e_1$, so:

$$\hat{\boldsymbol{R}}_{\boldsymbol{\ell}}(\boldsymbol{\phi_\mu}) = \left\| A^T b \right\|^2 y_l^T(\mu) y_l(\mu) \tag{4.38}$$

Similar to Eq. (4.27), $y_l(\mu)$ is calculated using the least squares method and QR approach:

$$y = \arg\min \left(\left\| \begin{bmatrix} \bar{\hat{C}}_{\ell-1}^T \\ \mu^{1/2} I_\ell \end{bmatrix} y - \mu^{1/2} e_{\ell+1} \right\| \right) \tag{4.39}$$

where $\bar{\hat{C}}_{\ell-1}$ is calculated by removing the last column of $\hat{C}_{\ell-1}$.

Now we need to calculate factors of C_ℓ, $\bar{C}_\ell$ and $\hat{C}_\ell$. These factors can be computed using Lanczos bidiagonalization procedure.

Lanczos bidiagonalization procedure: The procedure uses iterations of the Lanczos algorithm to create a lower bidiagonal matrix. It is assumed that there is a linear system of equations of $Ax = b$. Lanczos algorithm is applied to the matrix A, which is an $m \times n$ matrix, and initial vector of b, which is an $m \times 1$ matrix, to get matrix C_ℓ (see Table 4.1). More details about the algorithm can be found in [67, 60, 66].

$$
\begin{aligned}
&\sigma_1 = \|b\|, u_1 = b/\sigma_1, \bar{v_1} = A^T u_1, \rho_1 = \|\bar{v_1}\|, v_1 = \bar{v_1}/\rho_1 \\
&\text{for } j = 2, .., \ell \text{ do:} \\
&\bar{u_j} = Av_{j-1} - \rho_{j-1}u_{j-1}, \sigma_j = \|\bar{u_j}\|, u_j = \bar{u_j}/\sigma_j \\
&\bar{v_j} = A^T u_j - \sigma_j v_{j-1}, \rho_j = \|\bar{v_j}\|, v_j = \bar{v_j}/\rho_j \\
&\text{end} \\
&\bar{u}_{\ell+1} = Av_\ell - \rho_\ell u_\ell, \sigma_{\ell+1} = \|\bar{u}_{\ell+1}\|, u_{\ell+1} = \bar{u}_{\ell+1}/\sigma_{\ell+1} \\
&\bar{\delta}_1 = \rho_1, c_1 = \frac{\bar{\delta}_1}{\left\| \begin{bmatrix} \bar{\delta}_1 \\ \sigma_2 \end{bmatrix} \right\|}, s_1 = \frac{\sigma_2}{\left\| \begin{bmatrix} \bar{\delta}_1 \\ \sigma_2 \end{bmatrix} \right\|}, \delta_1 = c_1\bar{\delta}_1 + s_1\sigma_2; \\
&\text{for } j = 2, .., \ell \text{ do:} \\
&c_j = \frac{\bar{\delta}_j}{\left\| \begin{bmatrix} \bar{\delta}_j \\ \sigma_{j+1} \end{bmatrix} \right\|} \\
&s_j = \frac{\sigma_{j+1}}{\left\| \begin{bmatrix} \bar{\delta}_j \\ \sigma_{j+1} \end{bmatrix} \right\|} \\
&\delta_j = c_j\bar{\delta}_j + s_j\sigma_{j+1} \\
&\gamma_{j+1} = s_j\rho_{j+1} \\
&\bar{\delta}_{j+1} = -c_j\rho_{j+1} \\
&\text{end}
\end{aligned}
\tag{4.40}
$$

Table 4.1: This table shows the Pseudo code for Lanczos bidiagonalization procedure .

In order to have two matrices of $U_\ell = [u_1, .., u_\ell]$ and $V_\ell = [v_1, .., v_\ell]$ with orthogonal columns, such that: $V_\ell^T V_\ell = I_\ell$ and $U_\ell^T U_\ell = I_\ell$, the classical Gram Schmidt (CGS) algorithm [68, 69, 70] was applied:

$$
\begin{aligned}
&U(:,1) = u_1, V(:,1) = v_1 \\
&\text{for } j = 2, .., \ell \text{ do:} \\
&u_j = u_j - U(:, 1:1:j-1)(U(:, 1:1:j-1)^T u_j, U(:,j) = u_j / \left\| u_j \right\| \\
&v_j = v_j - V(:, 1:1:j-1)(V(:, 1:1:j-1)^T v_j, V(:,j) = v_j / \left\| v_j \right\|
\end{aligned}
\tag{4.41}
$$

QR factorization using plane rotation: QR factorization of matrix A in a system of equations of $Ax = b$ is calculated such that:

$$
A = QR \tag{4.42}
$$

where $R = Q^T A$ and Q^T is multiplication of given rotation matrices which make matrix A an upper matrix. To have an upper matrix, it is required to make all below off diagonal elements equal to zero. To do this, some rotation matrices are used [71]

Multiplication of the matrix A by $R(i, j, \theta)$ makes the element a_{ji} of matrix A equal to zero if:

$$
\begin{aligned}
\cos(\theta) &= a_{ii} / \sqrt{a_{ii}^2 + a_{ji}^2} \\
\sin(\theta) &= -a_{ji} / \sqrt{a_{ii}^2 + a_{ji}^2}
\end{aligned}
\tag{4.43}
$$

All off diagonal nonzero elements can therefore be eliminated by a sequence of rotations. We start with the first column. As such, the procedure starts with the first element in the first column below the diagonal. If it is in k-th row, it can become zero by $R(1, k, \theta)$. Then we proceed to the next nonzero in the first column and continue until all elements below the

diagonal become zero. Next, we moved to the next column and repeat the above procedure. We continue this procedure for all columns until all the elements below the diagonal become zero. After making all the elements below the diagonal for all column equal to zero, R becomes an upper triangular matrix which is:

$$G_N G_{N-1} ... G_2 G_1 A = RQ = G_1^T G_2^T ... G_N^T \tag{4.44}$$

Least squares method using QR factorization: As mentioned earlier, Eqs. (4.27, 4.31, 4.35 and 4.39) can be solved using least squares method and QR factorization. Suppose we want to find the answer to the equation of:

$$\vec{x} = \arg\min \left\| [A]\vec{x} - \vec{b} \right\|^2 \tag{4.45}$$

where A is a $m \times n$ matrix. A can be written as $A = QR$ in which Q is a $m \times n$ orthogonal matrix and R is a $m \times n$ upper triangular matrix. Q is orthogonal, therefore $Q^{-1} = Q^T$. The condition number of Q is equal to 1 ($\|[Q]\| = 1$), therefore multiplying a matrix by matrix Q or Q^T (any orthogonal matrix) does not alter the norm of the matrix.

$$\left\| [A]\vec{x} - \vec{b} \right\|^2 = \left\| Q^T([A]\vec{x} - \vec{b}) \right\|^2 = \left\| Q^T[A]\vec{x} - Q^T\vec{b} \right\|^2 \tag{4.46}$$

$[Q]$ can be written as $[Q] = [Q_1 Q_2]$ where Q_1 is a $m \times n$ matrix and Q_2 is a $m \times m - n$ matrix. $[R]$ can also be written as $[R] = \begin{bmatrix} R_1 \\ 0 \end{bmatrix}$ where R_1 is a $n \times n$ matrix. Eq. (4.46) can therefore be rewritten as:

$$\left\| Q^T[A]\vec{x} - Q^T\vec{b} \right\|^2 = \left\| \begin{bmatrix} R_1 x \\ 0 \end{bmatrix} - \begin{bmatrix} Q_1^T b \\ Q_2^T b \end{bmatrix} \right\|^2 = \left\| R_1 x - Q_1^T \vec{b} \right\|^2 + \left\| Q_2^T \vec{b} \right\|^2 \tag{4.47}$$

To minimize Eq. (4.47), there is no control over $Q_2^T\vec{b}$, but the first term in right part of

the equation can be minimized, therefore:

$$\left\| R_1 x - Q_1^T b \right\|^2 = 0 \rightarrow R_1 x = Q_1^T b \rightarrow x = R_1^T Q_1^T b \tag{4.48}$$

4.3 Methods

TRASE has been implemented in a B_0 field of 0.2 T [5]. For the corresponding low frequencies (8.5 MHz at 0.2 T), the B_1 field may be, and was, calculated using Biot-Savart's Law (3.2).

For each of the three coil types, linear, parallel conductor and circular, simulated noiseless signals were generated following Eq. (3.26) with $L = M \times N = 128 \times 128$ for two phantom types defined on a FOV of 16 cm $\times$ 16 cm for linear and circular set coils and 14 cm $\times$ 14 cm for the parallel conductor coil set where the phase gradient variation is more linear than in the larger FOV. The reconstructed image size was $I \times J = 128 \times 128$. The two phantom types were the Shepp-Logan image [72] and point-source phantoms centered at three points $(-a, -b)$, $(0, 0)$ and (a, b):

$$\rho_1(x, y) = E_{(-a,-b)}(x, y) \tag{4.49}$$

$$\rho_2(x, y) = E_{(0,0)}(x, y) \tag{4.50}$$

$$\rho_3(x, y) = E_{(a,b)}(x, y) \tag{4.51}$$

where $E_{(x,y)}$ are the image basis functions as given by Eq. (4.7). The centers of the basis functions were specified by $(a, b) = (7.4, 7.4)$ cm for the linear and circular coil sets and $(a, b) = (6.5, 6.5)$ cm for the parallel conductor set. Reconstruction of the basis functions, being approximations of δ functions, gives an approximation of the localized PSFs, $\phi_{(a,b)} \cong PE_{(a,b)}$.

For the Shepp-Logan phantom, Gaussian white noise was added to the computed signals

to give signal noise ratios (SNR) of ∞ (no noise), 10, 50 and 100 dB in each of the real and imaginary parts. All signals were reconstructed using both the DFT and least squares methods. Difference images between the original Shepp-Logan phantom and the individual reconstructions were computed along with an overall root mean squared error (RMSE) difference $E = \sqrt{\frac{1}{IJ}\sum_i \sum_j (P\rho(x_i, y_j) - \rho(x_i, y_j))^2}$.

The 16384 $\times$ 16384 matrix $[T]$ was generated using the High Performance Computing Cluster at the University of Saskatchewan (1 node of 96 nodes was used with a node being 2 $\times$ eight-core – 16 workers – Intel E5-2650L Xeon processors running at 1.8 GHz with 32 GB RAM). Using the cluster reduced the time needed to compute the matrix components (see Eq. (4.13)) by an estimated factor of 33, based on testing with smaller matrices, from 264 hours of computation on a general purpose computer, with a Core i7 CPU with 16 GB RAM running at 2.0 GHz, to 8 hours of computation on the cluster. The matrix $[T]$ only needs to be computed once. $[T]$ was computed for the linear and circular coil sets with FOVs of 16 cm $\times$ 16 cm and for the parallel conductor coil set with a FOV of 14 cm $\times$ 14 cm. The FOV of the circular coil set was also increased from 16 cm $\times$ 16 cm to 24 cm $\times$ 24 cm to test the hypothesis that the least squares approach can give a better reconstruction in a non-linear RF encoding coil over a larger FOV than Fourier reconstruction can give in a similarly sized linear RF encoding coil.

4.4 Results

The phase of the B_1 field was made to vary linearly for the linear coil set with $G_x = G_y = 7.20$ deg/cm. Figure 4.1 shows the variation of the phase of the B_1 field in the x direction for different values of y in the circular coil set. The variation of the phase of B_1 field is not linear,

therefore the phase gradient is not constant over a field of view (FOV) of 16 cm $\times$ 16 cm. The phase gradient is 6.03 deg/cm at the center and 4.09 deg/cm at the edge of the FOV with an average of 5.42 deg/cm over the FOV. Figure 4.2 shows the variation of the phase of the B_1 field in the x direction for different values of y in the parallel conductor coil set. The phase gradient of B_1 field is not constant over a FOV of 14 cm $\times$ 14 cm. The phase gradient is 7.35 deg/cm at the center and 5.59 deg/cm at the edge of the FOV with an average of 6.68 deg/cm over the FOV.

The spatial phase variation of the B_1 field for the parallel conductor and circular coil sets was close to linear in the center and the magnitude of the B_1 field was uniform in the center as well, but the deviation from linearity and uniformity was considerable at the edges. The largest change in gradient for the circular coil set over the dimensions of the phantom FOV of 16 cm $\times$ 16 cm was approximately 47 percent of the average at the edge of the FOV. The largest change in gradient for the parallel conductor coil set over the dimensions of the the phantom FOV of 14 cm $\times$ 14 cm was approximately 13 percent of the average at the edge of the FOV.

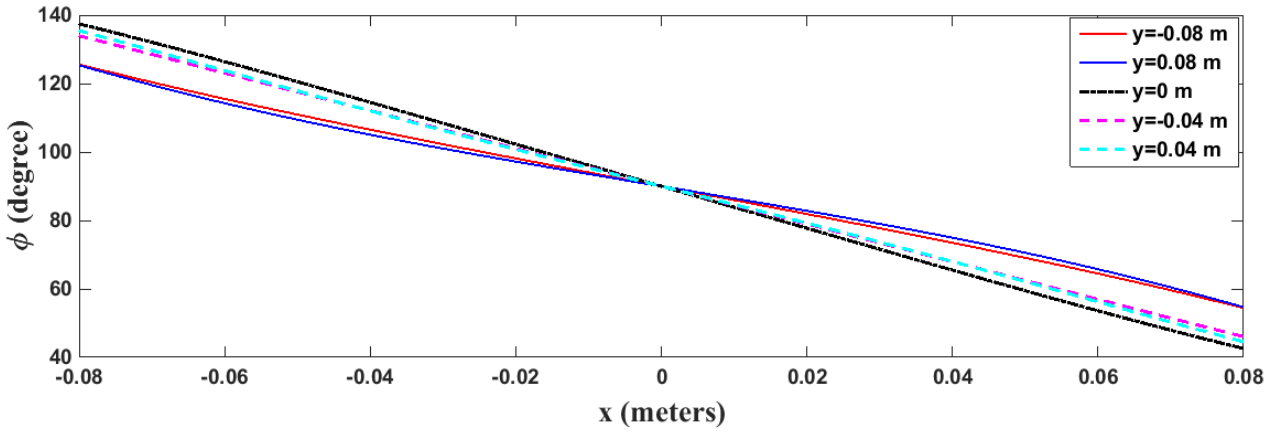

Figure 4.1: The variation of Φ along the x direction for different values of y for the circular coil set. The simulation was done in Matlab.

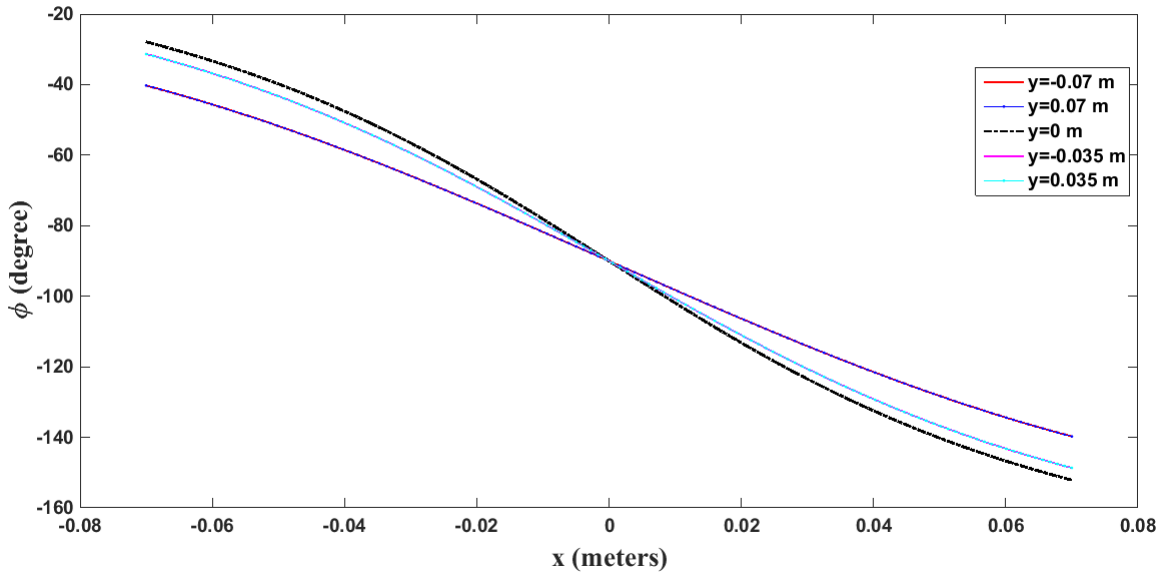

Figure 4.2: The variation of Φ along the x direction for different values of y for the parallel conductor coil set. The simulation was done in Matlab.

The computed approximations of the PSFs are shown in Figure 4.3. The PSFs for the DFT reconstructions are shifted versions of the PSF at $(0, 0)$ but the locations are shifted from the correct locations for the non-linear, circular and parallel conductor, coil sets. This shifted location of the PSFs leads to geometric distortion of the reconstructed images. The PSFs for the LS reconstructions are centered at the correct locations but their shapes, or profiles, are different from the PSF at $(0, 0)$. This characteristic of the LS PSFs leads to images that have no geometric distortion but they have a variable blurring, or resolution, across the image. With the DFT, the resolution is characterized essentially by a Cartesian product of a single Sinc function across the entire image. With the LS reconstructions the resolution is characterized by a more complex function that varies across the image.

The reconstructions of the Shepp-Logan 128×128 pixel numerical phantom, from noiseless signals, are shown in Figure 4.4. The geometric and intensity distortions present in the DFT reconstructions are not present in the LS reconstructions. The RMSE of the noiseless reconstructions are reported in Table 4.2. The effect of adding noise to the signals prior to LS reconstruction is shown in Figure 4.5. SNRs of 10 dB and possibly 20 dB are achievable with physical hardware; the 50 dB mathmatical illustration is visually indistinguishable from the noiseless reconstruction. However, there are small differences as may be seen by comparing the RMSE values reported in Table 4.3 with the LS line in the previous table.

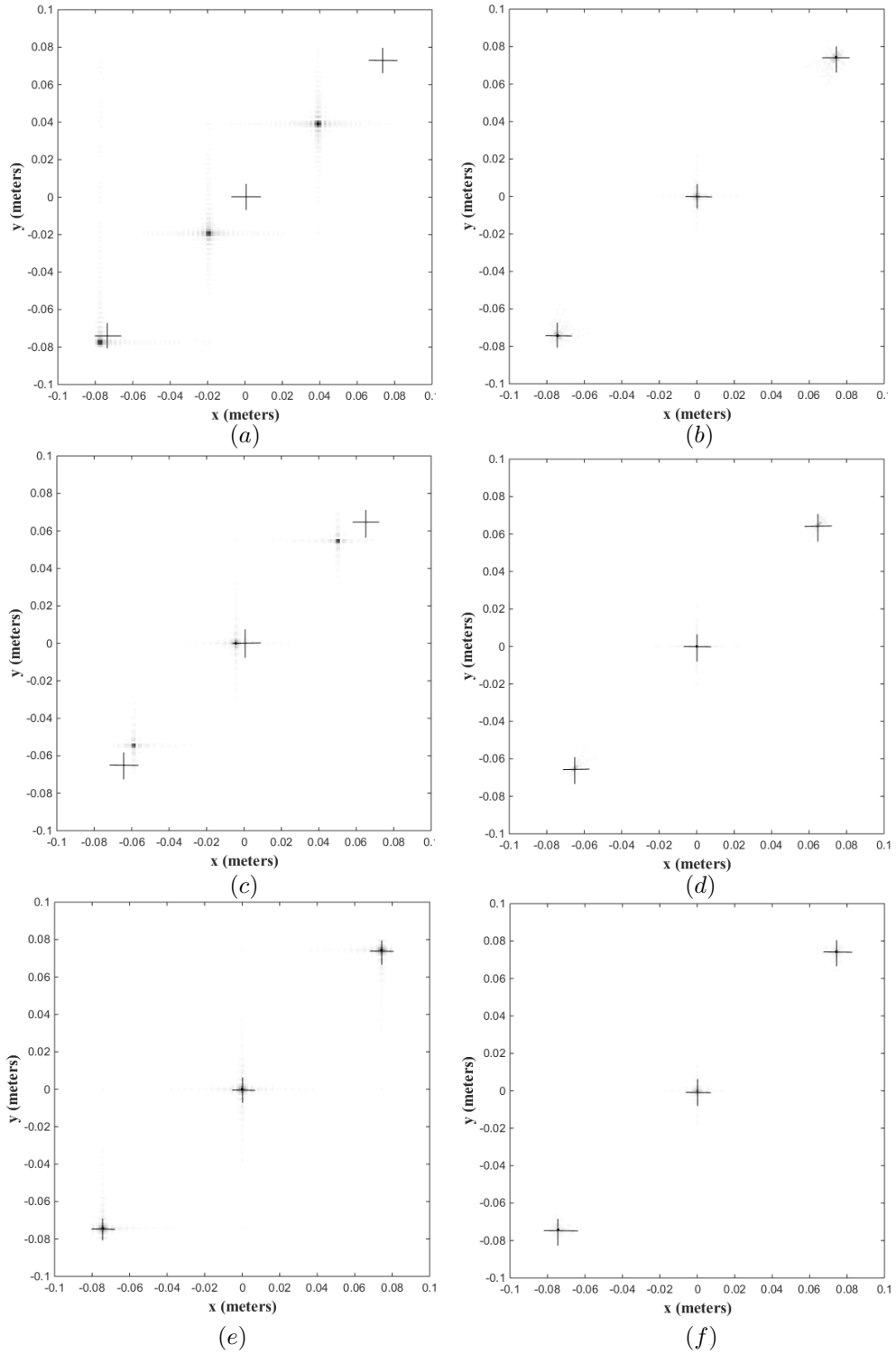

Figure 4.3: The sum of point spread functions (PSFs) from positions (a, a), $(0, 0)$ and $(-a, -a)$ where $a = 7.4$ for the linear and circular coil sets and $a = 6.5$ for the parallel coil set. The true positions of the 3 points have been shown with cross line. The left column (a, c, e) illustrates the DFT PSFs while the right column (b, d, f) illustrates the LS PSFs. The first row (a, b) is for the circular coil set, the second row (c, d) is for the parallel conductor coil set and the third row (e, f) is for the linear coil set.

	Circular coil set	Parallel conductor coil set	Linear coil set
DFT	0.1946	0.2197	0.0811
LS	0.0615	0.0501	0.0431

Table 4.2: Root Mean Square Errors for the reconstructions shown in Figure 4.4.

SNR	Circular coil set	Parallel conductor coil set	Linear coil set
10 (db)	0.0967	0.0992	0.0857
20 (db)	0.0903	0.0903	0.0783
50 (db)	0.0881	0.0856	0.0756

Table 4.3: Root Mean Square Errors for the reconstructions shown in Figure 4.5.

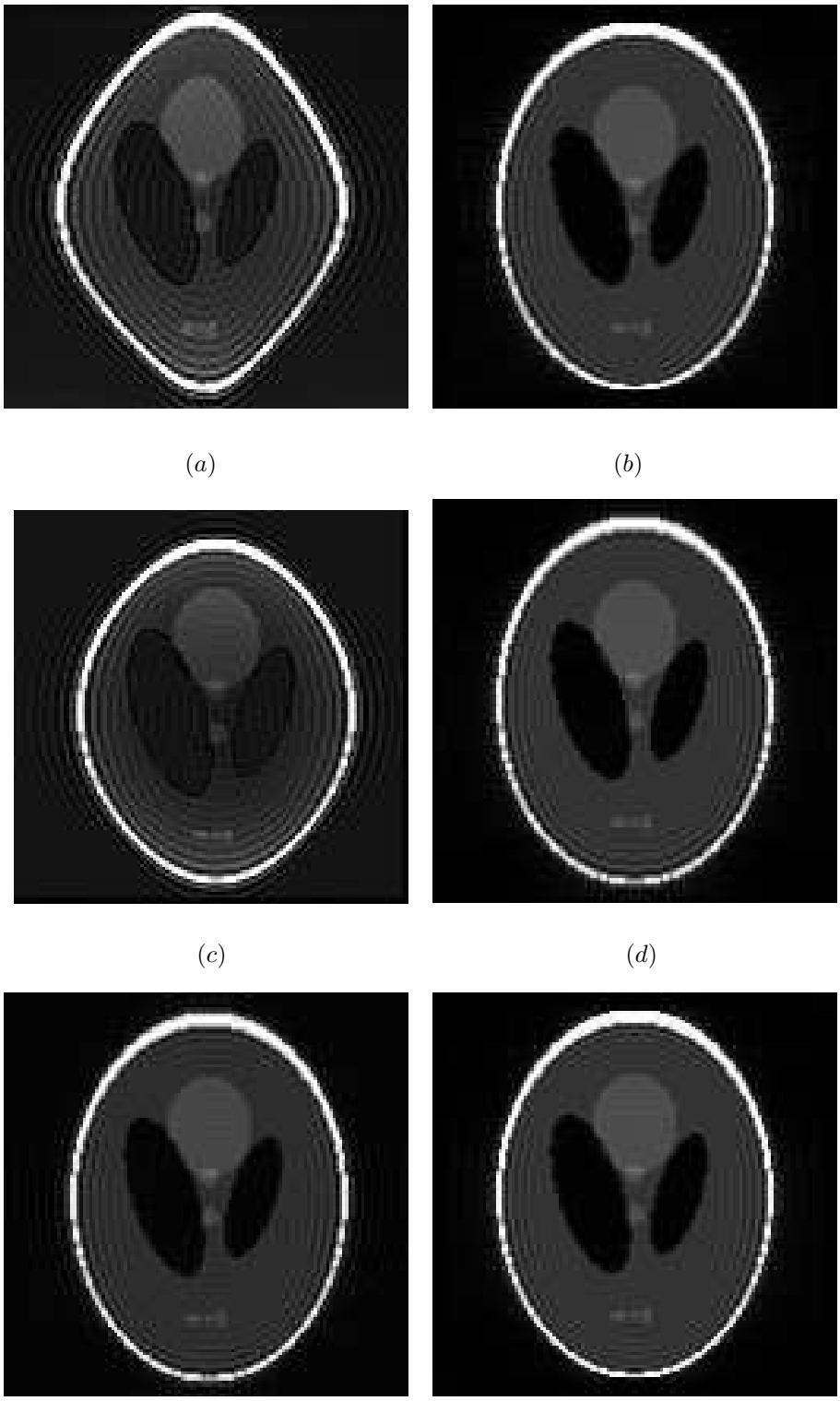

Figure 4.4: Reconstructed 128×128 pixel phantom images from noiseless signals from the circular coil set (first row a, b), the parallel conductor coil set (second row c, d) and the linear coil set (third row e, f). The left column (a, c, e) shows the DFT reconstructed images while the right column (b, d, f) shows the LS reconstructed images.

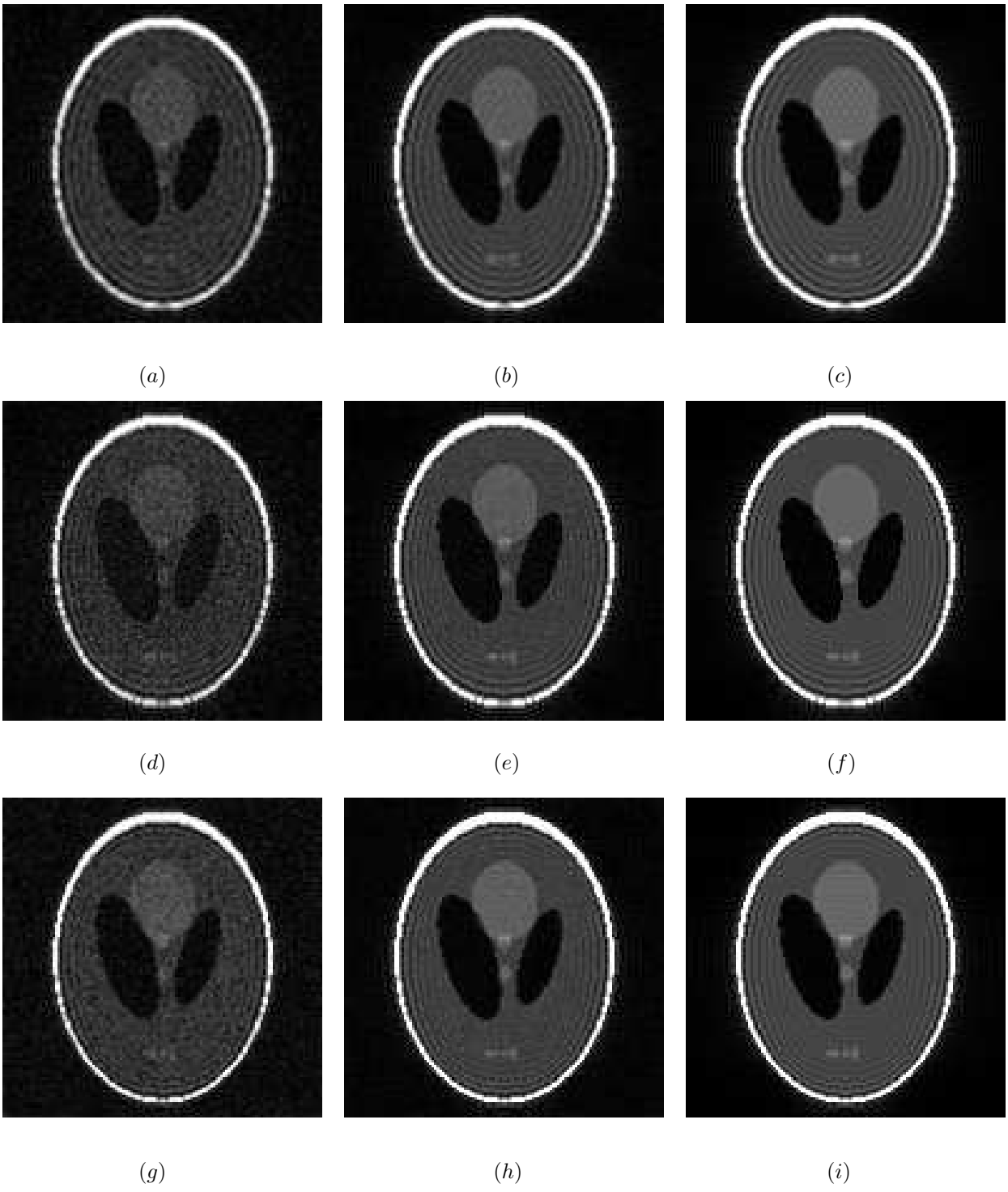

Figure 4.5: The effect of adding noise to the signals. The columns (lined up with a, b, c) show reconstructions from signals with noise added at SNR=10, 20 and 50 db. The first row (a, b, c) is for the circular coil set, the second row (d, e, f) is for the parallel conductor coil set and the last row (g, h, i) is for the linear coil set.

Increasing the size of the numerical phantom, the FOV, from 16 cm × 16 cm to 24 cm × 24 cm inside the fixed circular coil set leads to the reconstructions shown in Figure 4.6. No geometric distortions are present in the LS reconstruction despite the use of a B_1 with more variation in the spatial phase gradient.

(*a*) (*b*) (*c*)

Figure 4.6: The 128 × 128 pixel phantom and reconstructed images inside the circular coil set with FOV of 24 cm × 24 cm. (a) The phantom. (b) DFT reconstructed image. (c) LS reconstructed image.

4.5 Conclusion

The original TRASE method [5] relies on the linear variation of the RF phase with space with the result that Fourier transform techniques can be used to reconstruct the image from the encoded NMR signal. Here we have shown that, similar to SEM in arbitrary B_0 fields, that (regularized) least squares may be used to reconstruct images from NMR signals encoded in RF fields whose phase has a non-linear spatial variation.

The LS method leads to solving a system of equations as given by Eq. (4.14). A solution is possible for the B_1 fields used in our simulations because the deviation of the spatial phase

gradient from linearity is not large. With larger deviations from linearity, the condition number of the encoding matrix $[T]$ will increase, eventually leading to an ill-posed inverse problem. We did not investigate what the limits are for handling large deviations from linear phase variation. The reconstruction time for an image with 128×128 using LS is about 13 minutes, using DFT is about 6 minutes and using FFT is 0.11 second on a general purpose computer, with a Core i7 CPU with 16 GB RAM running at 2.0 GHz. The matrix $[T]$ is large with a size of 16384×16384 for an image with 128×128 pixels. The large matrix was computed using a cluster to decrease the computation time. The encoding matrix $[T]$ only needs to be computed once for any given image size, because it otherwise depends only on the known B_1 field and pulse sequences. At low B_0 field the introduction of a patient will not significantly change the B_1 field. Therefore, a set of encoding matrices could be preloaded with the software for a practical portable MRI; there is no need to compute $[T]$ every time.

For an ideal noiseless signal, a bare least squares technique with a normal equation solution gives a suitable reconstruction. However, in the presence of noise, the ordinary least squares technique is not enough to obtain a useful solution and constraints need to be applied to regularize the problem to obtain a suitable solution. Here we have demonstrated that the Tikhonov regularization technique leads to suitable reconstructions.

As you can see in Table 4.2 the RMS is not zero for noiseless Fourier encoding (linear coil set) with DFT reconstruction and even with LS reconstruction. The reason is that the model image that we are reconstructing, like real images, is not band-limited. Therefore, the image cannot be completely represented by a finite number of points in k-space and the reconstruction from those finite number of points will be the convolution of the original image with a point spread function ϕ as given by Equation (4.5). The reconstruction cannot be

perfect and will have a limited resolution and Gibbs ringing artifacts.

LS reconstructions are less robust to noise than comparable DFT reconstructions. This is because the DFT is unitary whereas LS is not, so the LS reconstruction amplifies noise where the DFT does not.

Using the Fourier transform for signal reconstruction requires that the FOV be confined to a region where the RF phase variation is appropriately close to linear. The FOV in the LS approach is not as constrained by B_1 spatial phase gradient variations and within a physically realistic circular coil set of 28 cm diameter the FOV could be increased from 16 cm $\times$ 16 cm to 24 cm $\times$ 24 cm without distorting the reconstruction.

The original RF encoding method of TRASE requires a linearly varying B_1 spatial phase gradient to encode the NMR signal and Fourier transformation methods to reconstruct the image. Here we have shown how RF encoding may be generalized to the non-linearly varying B_1 spatial phase case with a regularized least squares reconstruction replacing Fourier transformation methods. This is an important method because the reconstruction of images from non-linear phase gradients will allow more freedom to design coils optimized for other parameters such as efficiency and B_1 homogeneity. Using the approach given here, only a crude approximation to a linearly varying RF phase is required to achieve RF image encoding and, in a plane, encoding may be accomplished using simple conductor loops.

Off-resonance behavior was not simulated in this chapter which should be very similar to the behavior of linear TRASE approaches which have been demonstrated to work in physical, uniform, MRI magnets [11]. There are also numerous ways that the off-resonance effects can be mitigated. One is to shorten the number of 180° pulses in the echo train. Another is to model known inhomogeneities into the encoding matrix $[T]$ of Eq. (4.18) which

will be considered in chapter 5. The effect of inhomogeneous B_1 field on flip angle was not also simulated in this chapter which results in pulse imperfection. Therefore, we need to compensated for B_1 and B_0 inhomogeneties. In the next chapter we will show that compensating for B_0 and B_1 inhomogeneties may be possible through a combination of pulse sequence design and an expansion of the LS methods used here.

Chapter 5

Composite Pulses for RF Phase Encoded MRI

5.1 Introduction

RF phase encoded MRI encodes spatial information by using a spatially varying B_1 phase instead of traditional B_0 gradients coils [5]. Linear RF phase encoding coils can create the desired B_1 field (a linearly varying B_1 phase) over a limited field-of-view (FOV) [11]. We showed in chapter 4 that a larger FOV is possible if non-linear spatial phase variation is used [46]. The use of non-linear RF phase encoding would also simplify the design and manufacture of the RF coils. In addition to the phase, the magnitude of the B_1 field will also vary spatially with non-linear RF phase encoding coils and this will lead to differential spin tip angles in the imaged sample. Therefore, using a non-linear RF phase encoding coil will result in spatially dependent RF pulse imperfections in terms of tip angles produced versus tip angles intended.

RF encoding requires the application of a train of 180° RF pulses through an RF phase encoding coils. Spatially varying RF pulse imperfections will be accumulated if a Carr-Purcell sequence [73] is used. In order to decrease the sensitivity of the original Carr-Purcell pulse sequence to spatial RF pulse imperfections, the Carr-Purcell-Meiboom-Gill (CPMG) method was developed in which there is a 90° temporal phase shift between the original 90° pulse and the first 180° pulse of the pulse train (see Figure 5.1) [74]. However, the CPMG sequence

can not compensate for field imperfections completely [75], so composite pulses have been introduced to address this deficiency.

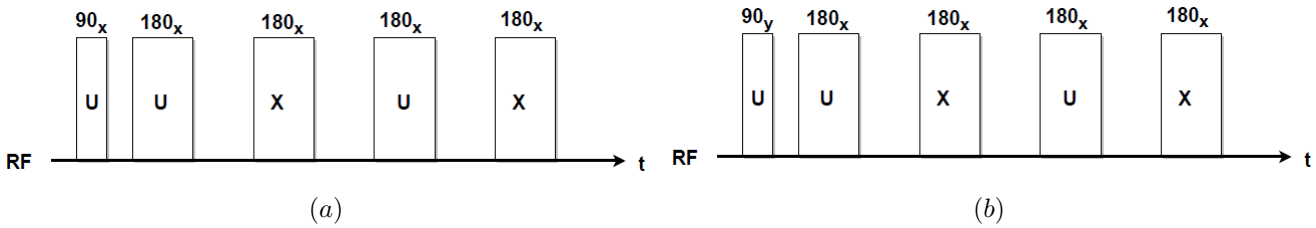

Figure 5.1: This figure shows Carr-Purcell and CPMG pulse sequence. (a) shows the Carr-Purcell pulse sequence which consist of a 90° excitation pulse using a uniform coil followed by a train of 180° pulses using a uniform and RF phase encoded coil. 90_x means 90° rotation about the x axis. U and x means using a uniform and RF phase encoded coil respectively. (b) shows CPMG pulse sequence which consists of a 90° temporal phase shift between the original 90° pulse and the first 180° pulse of the pulse train. 90_y means 90° rotation about the y axis which shows a 90° temporal phase shift.

Composite pulses are composed of a cluster of RF pulses having different phases with short time intervals between pulses, short enough so that no effective relaxation occurs between the pulses in the cluster. Different methods have been proposed to design such composite pulses including simulations based on chasing the path of the magnetization vector [76], magnetization movement analysis based on rotation operators [77], estimation based on adiabatic following [78], and coherent averaging theory with the Magnus expansion [79]. Using these methods, different composite pulses, classified as symmetric, asymmetric and antisymmetric, have been designed to compensate for both B_1 inhomogeneity and off-resonance effects caused by the inhomogeneous B_0 main field [80, 76, 81, 82, 79, 83, 84, 85, 86, 87, 88]. Composite pulses have been applied in conventional MRIs (using B_0 field gradients) to improve the performance of a population inversion of 180° [80], refocusing pulses of 180° [75] and, excitation pulses of 90° [89]. However, it is not known whether the application of composite pulses in RF encoded MRI could compensate for B_1 and B_0 imperfections.

Here we study the application of composite pulses to RF phase encoding using a Bloch simulation. The simulation, using Maxwell/Helmholtz coil pairs, is applied to identify which pulse sequence best minimizes the effect of inhomogeneous B_1 and B_0 fields on the tip angle and the resulting image reconstruction. This study is necessary because existing composite pulses have been designed for use in conventional MRIs and we need to assess the feasibility of using composite pulses for RF phase encoding.

This chapter is organized as follows. In the theory section, the Bloch simulation approach is described followed by a discussion of how multiple spin echo sequences are used for RF phase encoding and how composite pules are introduced into the multiple spin echo RF encoding sequences. A description of the Least Squares – Total Variation (LS-TV) method used for image reconstruction is then given. In the methods section, the RF coil design used in the simulations is described, the composite pulse sequences tested are listed and descriptions are given of how the effects of off-resonance (B_0 inhomogeneity) and noise were simulated. The results are presented in terms of Root Mean Square Error (RMSE) and reconstructed phantom images. Recommendations for the best composite pulses to use for RF encoded MRI are given in the discussion.

5.2 Theory

5.2.1 Bloch simulation approach

The physics of MRI was simulated using the Bloch equation [90, 91, 92, 93, 94, 95]. To encode information in two dimensions (the x and y directions, assumed in this chapter to be orthogonal to the main field z direction), the RF encoding coil needs to produce a spatial variation of the B_1 phase in the x and y directions. A simple design for the RF encoding

coil was assumed that consists of one Maxwell coil pair and one Helmholtz coil pair (see Figure 3.4). This simple RF phase encoding coil design generates a B_1 field with a non-linear spatially varying phase along the intended encoding direction and a spatially inhomogeneous magnitude. The inhomogeneous magnitude results in a spatially varying tip angle. The effect of the inhomogeneous B_1 field on the spin magnetization was simulated using the Bloch equation, $\frac{d\vec{M}}{dt} = \gamma(\vec{M} \times \vec{B})$ [90], where $\vec{M}$ is the spin magnetization and $\vec{B}$ is the magnetic field, both functions of spatial position $\vec{r}$ and time t.

Spins in the imaged sample experience a local magnetic field of:

$$\vec{B}(\vec{r}, t) = B_0(\vec{r})\vec{z} + \vec{B_1}(\vec{r}, t) \tag{5.1}$$

where $B_0(\vec{r}) = \mathcal{B}_0 + \Delta B(\vec{r})$ is the main magnetic field, which varies spatially, and $\vec{B_1}$ is the RF field which changes with time, t, and position, $\vec{r}$. A discrete time solution of the Bloch equation at discrete spatial positions $\vec{r_i}$ may be given using rotation matrices [94], which depends on the inhomogeneity of the main magnet, the relaxation times and the RF pulse sequences, according to:

$$\vec{M}(\vec{r}, t + \Delta t) = [\mathrm{Rot}_z(\theta_i)]\,[R_{\mathrm{RF}}]\,\vec{M}(\vec{r}, t) \tag{5.2}$$

where $[\mathrm{Rot}_z(\theta_i)]$ is a rotation matrix about z axis by θ_i which is related to the inhomogeneity of the main magnet ($\Delta B(\vec{r})$) by:

$$\theta_i = \gamma \Delta B(\vec{r_i}) \Delta t \tag{5.3}$$

and where $[R_{\mathrm{RF}}]$ gives the effect of RF pulses as a rotation about the phase angle axis of the RF (tip angle) as:

$$[R_{RF}] = [\mathrm{Rot_z}(\phi)]\,[\mathrm{Rot_y}(\beta)]\,[\mathrm{Rot_x}(\alpha')]\,[\mathrm{Rot_y}(-\beta)]\,[\mathrm{Rot_z}(-\phi)] \tag{5.4}$$

where [Rot_x] and [Rot_y] are rotations about x and y axes respectively, ϕ is the phase angle of the RF and α' and β are defined as:

$$\alpha' = \sqrt{\theta_i^2 + \alpha''^2} \tag{5.5}$$

$$\beta = \tan^{-1}\left(\frac{\theta_i}{\alpha''}\right) \tag{5.6}$$

where α'' is the actual tip angle in each position. The actual tip angle in each position is different than the nominal one, because spins experience an RF field different from the nominal one (the one at the center of the imaged sample ($\vec{\mathcal{B}_1}$)). The actual tip angle can be written as:

$$\alpha''(i) = \frac{B_1(i)}{\mathcal{B}_1}\alpha \tag{5.7}$$

where α is the nominal tip angle (the tip angle that nuclei at the center of the imaged sample receive), $B_1(i)$ is the magnitude of the $\vec{B_1}$ field in each position and $\mathcal{B}_1$ is the magnitude of the $\vec{B_1}$ field at the center of the imaged sample.

The main magnetic field is assumed to be oriented along the z axis so we set:

$$\vec{M}(\vec{r}_i, 0) = \rho(\vec{r}_i)\vec{z} \tag{5.8}$$

The detected signal, a complex number at each time point, is the sum of transverse magnetization over the imaged sample as measured via a uniform RF coil (one with no spatial RF phase variation – not the RF encoding coil) and is given by:

$$s(t) = \sum_i M_x(\vec{r}_i, t)\ \vec{x} + j\sum_i M_y(\vec{r}_i, t)\ \vec{y} \tag{5.9}$$

The reconstructed image from the signal will have some artifacts, because the magnitude of the RF field varies spatially whereas the image reconstruction that we will use here assumes a constant magnitude B_1.

5.2.2 Multiple spin echo RF encoding sequences

To generate RF encoded imaging data, multiple spin echo pulse sequences fed through the appropriate RF encoding coils are required. Data points are nominally generated in k-space with each data point having a nominal k-space position. While three dimensional RF encoding is possible, here we focus on and simulate two dimensional encoding with an assumed slice selection that is not modeled.

Let M and N be even. Then to generate an $(N+1)\times(M+1)$ imaging dataset centered on the origin in k-space, the following set of pulse sequences, each separated by an appropriate repeat time, T_R, will do the job. The following pulse sequence is designated as the *standard RF encoding sequence* throughout this work.

$$
\begin{aligned}
&90_u - 180_u - S - [180_x - S - 180_u - S]^{N/2} \\
&\text{for } 1 \le m \le M/2 \text{ do:} \\
&90_u - 180_y - S - [180_u - S - 180_y - S]^{m-1} - [180_x - S - 180_u - S]^{N/2} \\
&90_u - 180_y - S - [180_u - S - 180_y - S]^{m-1} - [180_{-x} - S - 180_u - S]^{N/2}
\end{aligned}
\tag{5.10}
$$

where the square bracketed pulses are repeated for the number of times indicated in the superscript (e.g. the block in the first pulse sequence of Eq. (5.10) is repeated $N/2$ times); S denotes the read out of each echo, 90_u denotes a 90° tip angle excitation with a uniform coil while 180_x and 180_u denote 180° tip angle excitation with the x direction RF encoding coil and uniform coils respectively. The second sequence of Eq. (5.10) encodes k-space information in the second and fourth quadrants and the third sequence encodes information in the first and third quadrants of k-space.

The RF encoding sequence of Eq. (5.10) trades resolution for FOV. To increase the resolution at the expense of FOV (by increasing the distance between data points in "k-space") the following *high resolution RF encoding sequence* can be used:

$$90_u - 180_u - S - [180_x - S - 180_{-x} - S]^{N/2}$$

for $1 \leq m \leq M/2$ do:

$$90_u - 180_y - S - [180_x - S - 180_y - S]^{m-1} - [180_x - S - 180_{-x} - S]^{N/2}$$

$$90_u - 180_y - S - [180_x - S - 180_y - S]^{m-1} - [180_{-x} - S - 180_x - S]^{N/2} \tag{5.11}$$

5.2.3 Multiple spin echo sequences with composite pulses

Three basic multiple spin echo sequences were investigated for RF encoding application:

1. Carr-Purcell
2. CPMG
3. Phase alternated CPMG

For each of these basic sequences, the replacement of simple 180° pulses with composite pulses is possible.

The *Carr-Purcell pulse sequence* [73] as we use it here consists of a 90° RF excitation pulse from a uniform coil followed by a train of 180° pulses made through appropriate RF encoding coils (having spatial RF phase variation) and uniform coils as per the prescription of Eq. (5.10) or (5.11) with the same transmitted RF temporal phase being used for all pulses. Between the 180° pulses, a read out of the echo is performed through uniform receiver coils, giving one data point (which may be the average of several points from the analog-to-digital

convertor, the ADC). The Carr-Purcell version of our standard RF encoding sequence, given by Eq. (5.10), is:

$$
\begin{aligned}
&90_{u,0} - 180_{u,0} - S - [180_{x,0} - S - 180_{u,0} - S]^{N/2} \\
&\text{for } 1 \leq m \leq M/2 \text{ do:} \\
&90_{u,0} - 180_{y,0} - S - [180_{u,0} - S - 180_{y,0} - S]^{m-1} - [180_{x,0} - S - 180_{u,0} - S]^{N/2} \\
&90_{u,0} - 180_{y,0} - S - [180_{u,0} - S - 180_{y,0} - S]^{m-1} - [180_{-x,0} - S - 180_{u,0} - S]^{N/2}
\end{aligned}
\tag{5.12}
$$

where the second 0 subscripts represent the angle ϕ of Eq. (5.4). In this case $\phi = 0^\circ$ means that all tip angles are about the x axis in the rotating frame. The Carr-Purcell version of the high resolution variant, given by Eq. (5.11), is:

$$
\begin{aligned}
&90_{u,0} - 180_{u,0} - S - [180_{x,0} - S - 180_{-x,0} - S]^{N/2} \\
&\text{for } 1 \leq m \leq M/2 \text{ do:} \\
&90_{u,0} - 180_{y,0} - S - [180_{x,0} - S - 180_{y,0} - S]^{m-1} - [180_{x,0} - S - 180_{-x,0} - S]^{N/2} \\
&90_{u,0} - 180_{y,0} - S - [180_{x,0} - S - 180_{y,0} - S]^{m-1} - [180_{-x,0} - S - 180_{x,0} - S]^{N/2}
\end{aligned}
\tag{5.13}
$$

A 90° temporal phase shift was added between the 90° excitation and the first 180° refocusing pulse in both the x and y encoding directions to modify the Carr-Purcell pulse sequence into the *CPMG pulse sequence* [74] with all subsequent 180° refocusing pulses having

the same phase. The CPMG version of our standard RF encoding sequence, Eq. (5.10), is:

$$
\begin{aligned}
&90_{u,90} - 180_{u,0} - S - [180_{x,0} - S - 180_{u,0} - S]^{N/2} \\
&\text{for } 1 \leq m \leq M/2 \text{ do:} \\
&90_{u,90} - 180_{y,0} - S - [180_{u,0} - S - 180_{y,0} - S]^{m-1} - [180_{x,0} - S - 180_{u,0} - S]^{N/2} \\
&90_{u,90} - 180_{y,0} - S - [180_{u,0} - S - 180_{y,0} - S]^{m-1} - [180_{-x,0} - S - 180_{u,0} - S]^{N/2}
\end{aligned}
\tag{5.14}
$$

where $\phi = 90^\circ$ means that tip angles are about the y axis in the rotating frame. The CPMG version of the high resolution version, Eq. (5.11), is:

$$
\begin{aligned}
&90_{u,90} - 180_{u,0} - S - [180_{x,0} - S - 180_{-x,0} - S]^{N/2} \\
&\text{for } 1 \leq m \leq M/2 \text{ do:} \\
&90_{u,90} - 180_{y,0} - S - [180_{x,0} - S - 180_{y,0} - S]^{m-1} - [180_{x,0} - S - 180_{-x,0} - S]^{N/2} \\
&90_{u,90} - 180_{y,0} - S - [180_{x,0} - S - 180_{y,0} - S]^{m-1} - [180_{-x,0} - S - 180_{x,0} - S]^{N/2}
\end{aligned}
\tag{5.15}
$$

The third basic pulse sequence types considered here are the *phase alternated CPMG pulse sequences* which are sequences of refocusing pulses with alternating 180° phases [96]. Specifically, the phase alternated CPMG version of the standard RF encoding sequence,

Eq. (5.10), becomes:

$$90_{u,90} - 180_{u,0} - S - [180_{x,0} - S - 180_{u,0} - S - 180_{x,180} - S - 180_{u,0} - S]^{N/4}$$

for $1 \leq m \leq M/4$ do:

$$90_{u,90} - 180_{y,0} - S - [180_{u,0} - S - 180_{y,0} - S - 180_{u,0} - S - 180_{y,180} - S]^{m}$$

$$- [180_{x,0} - S - 180_{u,0} - S - 180_{x,180} - S - 180_{u,0} - S]^{N/4}$$

$$90_{u,90} - 180_{y,0} - S - [180_{u,0} - S - 180_{y,0} - S - 180_{u,0} - S - 180_{y,180} - S]^{m}$$

$$- [180_{-x,0} - S - 180_{u,0} - S - 180_{-x,180} - S - 180_{u,0} - S]^{N/4} \tag{5.16}$$

Pulses alternated CPMG pulse sequences were incorporated into the high resolution version of the RF encoding sequence of Eq. (5.11) as follows:

$$90_{u,90} - 180_{u,0} - S - [180_{x,0} - S - 180_{-x,0} - S - 180_{x,180} - S - 180_{-x,180} - S]^{N/4}$$

for $1 \leq m \leq M/4$ do:

$$90_{u,90} - 180_{y,0} - S - [180_{x,0} - S - 180_{y,0} - S - 180_{x,180} - S - 180_{y,180} - S]^{m}$$

$$- [180_{x,0} - S - 180_{-x,0} - S - 180_{x,180} - S - 180_{-x,180} - S]^{N/4}$$

$$90_{u,90} - 180_{y,0} - S - [180_{x,0} - S - 180_{y,0} - S - 180_{x,180} - S - 180_{y,180} - S]^{m}$$

$$- [180_{-x,0} - S - 180_{x,0} - S - 180_{-x,180} - S - 180_{x,180} - S]^{N/4} \tag{5.17}$$

In an effort to compensate for the effect of inhomogeneous B_1 and B_0 fields, composite pulses were used in place of a single 180° tip angle excitation for the RF encoding coils to generate the nominal 180^0 tip angle. Composite pulses were not used for 180° pulses through the uniform coils. That is, composite pulses were used to replace $180_{\pm x,\phi}$ and $180_{\pm y,\phi}$ pulses

but not $180_{u,\phi}$ pulses. This approach was taken because the uniform coils were modeled to be perfect and so were not in need of composite pulse compensation. Therefore the simulations focus on the effect of composite pulses through the RF encoding coils exclusively. Nine symmetric [80, 81, 85, 84, 86, 76], four asymmetric [79, 88] and two antisymmetric [83, 87] composite pulses were investigated as listed in Table 5.1.

Table 5.1: Composite pulses investigated.

Symmetric	
Freeman, Kempsell, Levitt [76]:	$90_{90} - 240_0 - 90_{90}$
Levitt-Freeman [80]:	$90_{90} - 180_0 - 90_{90}$
Tycko, Method 1 [81]:	$180_0 - 180_{120} - 180_0$
Tycko, Method 2 [81]:	$180_{120} - 180_{240} - 180_{120}$
Shaka-Pines [84]:	$60_{180} - 300_0 - 60_{180}$
Koroleva et al., Method 1 [86]:	$27_{180} - 126_0 - 27_{180}$
Koroleva et al., Method 2 [86]:	$15_{180} - 150_0 - 15_{180}$
Koroleva et al., Method 3 [86]:	$10_{180} - 160_0 - 10_{180}$
Koroleva et al., Method 4 [86]:	$5_{180} - 170_0 - 5_{180}$
Asymmetric	
Tycko et al. [79]:	$180_0 - 180_{105} - 180_{210} - 360_{59}$
Wimperis, Method 1 [88]:	$180_{104.5} - 360_{313.4} - 180_{104.5} - 180_0$
Wimperis, Method 2 [88]:	$180_{90} - 360_{225} - 180_{90} - 180_0$
Wimperis, Method 3 [88]:	$180_{90} - 360_{315} - 180_{90} - 180_0$
Antisymmetric	
Tycko, Pines, Guckenheimer [83]:	$180_{256} - 180_{52} - 180_0 - 180_{128} -$ $180_0 - 180_{232} - 180_0 - 180_{308} - 180_{104}$
Wimperis [87]:	$180_{45} - 180_{270} - 180_0 - 180_{90} - 180_{315}$

5.2.4 Image reconstruction

Images were reconstructed using a constrained least squares (LS) [56] method with Tikhonov regularization [57] followed by a total variation (TV) technique [97, 98, 99, 100, 97] to minimize noise in reconstructed images.

With the square RF encoding coil sets (Figure 3.4), the phase of the B_1 field changes non-linearly with position, so the discrete Fourier transform (DFT) fails to reconstruct the images properly. Instead of using the inverse DFT, a regularized LS method with Tikhonov regularization was used to reconstruct the images (See previous chapter (see Eq. (4.19)).

The TV method was next used to further decrease artifacts. The TV regularized solution, as generally applied to denoising, is the minimization problem:

$$\vec{X} = \arg\min \left(\left\| \vec{X} - \vec{R} \right\|^2 + \lambda \, T_V(\vec{X}) \right) \tag{5.18}$$

where $\vec{X}$ is the unknown image, $\vec{R}$ is the noisy solution from the LS method, λ is the regularization parameter, and $T_V(\vec{X})$ is the discrete TV defined as:

$$T_V(\vec{X}) = \sum_{i=1}^{M} \sum_{j=1}^{N} \sqrt{(X_{i+1,j} - X_{i,j})^2 + (X_{i,j+1} - X_{i,j})^2} \tag{5.19}$$

To find the solution to Eq. (5.18), fast gradient projection (FGP) was used [99]. FGP is a combination of a gradient-based method for the denoising problem [101] and the fast iterative shrinkage/thresholding algorithm (FISTA)[102]. With the FGP algorithm the solution to Eq. (5.18) at an iteration k is:

$$\vec{X_k} = \vec{R} - \lambda \, \vec{\mathrm{div}}_k \quad k = 2, \ldots, N \tag{5.20}$$

where N is the total number of iterations, $\vec{\mathrm{div}}_k$ is defined below and $\vec{X_1} = \vec{R}$. The stopping point is reached when $(f_k - f_{k-1})/f_k \leq \tau$ where τ is a given tolerance and $f_k = ||\vec{X_k} - \vec{R}||^2 +$

$\lambda\, T_V(\vec{X}_k)$. The vector $\vec{\text{div}}_k$, with lexically ordered components, is defined in terms of the image div_k as follows:

$$\text{div}_k(x_i, y_j) = \left\{ \begin{array}{ll} p_{i,j;k} & \text{if } i = 1 \\ p_{i,j;k} - p_{i-1,j;k} & \text{if } 1 < i < N \\ -p_{i-1,j;k} & \text{if } i = N \end{array} \right\} + \left\{ \begin{array}{ll} q_{i,j;k} & \text{if } j = 1 \\ q_{i,j;k} - q_{i,j-1;k} & \text{if } 1 < j < N \\ -q_{i,j-1;k} & \text{if } j = N \end{array} \right\} \quad (5.21)$$

where i, j are pixel coordinates and k is iteration number. Dropping the pixel coordinates, the values p_k and q_k in Eq. (5.21) are defined as:

$$p_{k+1} = m_k + \frac{t_k - 1}{t_{k+1}}(m_k - m_{k-1}), \quad q_{k+1} = n_k + \frac{t_k - 1}{t_{k+1}}(n_k - n_{k-1}) \quad (5.22)$$

where $t_{k+1} = \frac{1+\sqrt{1+4t_k^2}}{2}$ and m_k, n_k are defined as

$$m_k = p_k + \frac{\text{grad}_x(\vec{X}_k)}{8\lambda}, \quad n_k = q_k + \frac{\text{grad}_y(\vec{X}_k)}{8\lambda} \quad (5.23)$$

where grad_x is gradient in the x direction and the grad_y is gradient in y direction. The iterations are started with $p_1 = q_1 = n_0 = m_0 = 0$ and $t_1 = 1$.

The performance of the TV method is related to the value of λ. Larger λ will result in over smoothing and more noise removal while a smaller λ will result in a noisy image. Different values of λ were tried and the one resulting in an image with the minimum RMSE was selected.

5.3 Methods

5.3.1 RF encoding coil design and mathematical phantom

We simulated a 24 cm $\times$ 24 cm cubic RF phase encoding coil set (Figure 3.4) inside a main magnet with a Shepp-Logan phantom [72] defined on a FOV of 20 cm $\times$ 20 cm at $z = 0$. Phantoms defined on pixel grids of 32 $\times$ 32 and 64 $\times$ 64 were used. Figure 5.2 shows the

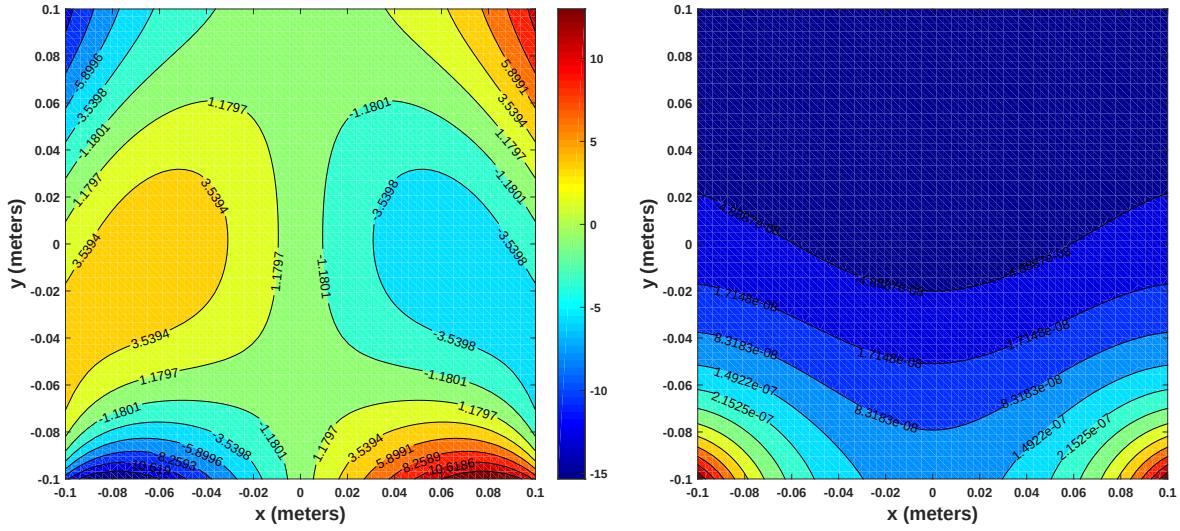

(a) (b)

Figure 5.2: It shows the variation of the actual B_1 phase and magnitude from the ideal ones for the square coil set. (a) shows the difference between the actual phase and the ideal one, $\phi(x, y) - G \times x$ (in degree), where $\phi(x, y)$ is the phase of the B_1 field for the x encoding in each position and G is the RF phase gradient in deg/m. (b) shows the difference between the actual magnitude and the ideal one $B_1(x, y) - B_{1_{av}}$, where $B_1(x, y)$ is the magnitude of B_1 field in each position and $B_{1_{av}}$ is the average of the magnitude of the B_1 field.

variation of the difference between actual phase of the B_1 field from the ideal phase in each position for the square coil set. The phase gradient of B_1 field is not constant over a FOV of 20 cm $\times$ 20 cm. The phase gradient is 5.71 deg/cm at the center and 3.31 deg/cm at the edge of the FOV with an average of 5.12 deg/cm over the FOV. The largest change in the magnitude of the RF field over the dimensions of the phantom was approximately 3.4 times of the average magnitude, at the edge of the FOV (see Figure 5.2).

5.3.2 Composite pulse sequences tested

Simulated signal generation and image reconstruction was done for each of the three types of multiple spin echo sequences as described in Section 5.2.3, without composite pulses, for

both the standard and high resolution RF encoding sequences with the smaller 32×32 phantom. The CPMG version of the standard RF encoding sequence was simulated using all the composite pulses listed in Table 5.1 with the smaller 32×32 phantom. The best result, as determined by the smallest RMSE, was determined for each of the symmetric, asymmetric and antisymmetric composite pulse designs. Simulations were then performed with the larger 64×64 phantom for the best symmetric, asymmetric and antisymmetric composite pulse designs.

5.3.3 Computational facilities

The encoding matrix $[T]$, a 4096×4096 matrix for the 64×64 phantom, was generated following Eq. (4.13) using the High Performance Computing Cluster (HPC) at the University of Saskatchewan (1 node of 96 nodes was used with a node being $2 \times$ eight-core – 16 workers – Intel E5-2650L Xeon processors running at 1.8 GHz with 32 GB RAM). The time needed to compute the matrix $[T]$ for different composite pulses using the cluster varied from about 24 hours for Levitt-Freeman composite pulse with the 64×64 phantom to about 63 hours for Wimperis composite pulse with the 64×64 phantom. For an implementation of the LS-TV as a general image reconstruction algorithm we note that the matrix $[T]$ only needs to be calculated once and stored in a look-up table for subsequent use.

5.3.4 Simulation of off-resonance effects and noise

The best CPMG standard RF encoding pulse sequence for each of the symmetric, asymmetric and antisymmetric composite pulse designs, using the larger 64×64 phantom, were run noise-free and with a homogeneous B_0 field to provide reference points for simulations of off-resonance effects and noise. For the simulation of off-resonance effects, an unknown (to

the reconstruction algorithm) quadratic inhomogeneous B_0 of 5 parts per million (ppm) ($\frac{\Delta B_0(\max)}{\mathcal{B}_0} = 5 \times 10^{-6}$) was simulated to show the effect of an inhomogeneous B_0 field on the reconstructed image. In this study, $\mathcal{B}_0$ was set equal to 0.2 T (the results nominally scale to any field strength) and ΔB_0 had a quadratic form of

$$\Delta B_0 = A(x^2 + y^2) \tag{5.24}$$

where A was specified according to the amount the inhomogeneity desired for B_0 in the FOV. Therefore $A = 50 \times 10^{-6}$ for a FOV of 20 cm $\times$ 20 cm and $\mathcal{B}_0 = 0.2T$. Although not explored here, we note that an *a priori* field map of ΔB_0 can be used in the image reconstruction algorithm, especially at low field where the magnitude of the operational wavelength is bigger than the size of body parts, and coil-tissue interactions are negligible [47]. Noise was added to the computed signals of the selected pulse sequences at signal to noise ratios (SNRs) of 20 and 50 dB.

5.4 Results

To evaluate the sequences and composite pulses relative to each other, a number of low resolution (32×32 phantom) simulations were done without added noise in a homogeneous B_0 main field.

Low resolution simulations comparing the Carr-Purcell, CPMG and alternated phase CPMG sequences without composite pulses showed the alternated phase CPMG sequence to be superior to the CPMG sequence which, in turn, was superior to the Carr-Purcell sequence for both the standard and high resolution RF encoding schemes. This showed that we may evaluate composite pulses relative to each other using the standard RF encoding sequence of Eq. (5.10) with the knowledge that the relative performance of the high resolution RF

encoding sequences with respect to composite pulse choices would be similar.

To simplify the analyses and simulations, composite pulses were evaluated only with the CPMG sequence and the standard RF encoding scheme. Low resolution (32×32 phantom) simulations for all of the composite pulses listed in Table 5.1 showed that the Levitt-Freeman design produced the best result among the symmetric composite pulse designs; the Tycko et al. design produced the best result among the asymmetric composite pulse designs and; the Wimperis design produced the best result among the antisymmetric composite pulse designs.

Figure 5.3 shows the reconstruction errors from six high resolution (64×64 phantom) standard RF encoded simulations with noiseless data in a homogeneous B_0 field. Straight Carr-Purcell, CPMG and alternated phase CPMG sequence simulations are shown along with the three best performing symmetric, asymmetric and antisymmetric CPMG composite pulse sequences. Of these six simulations, the Tycko et al. asymmetric composite pulse scheme generated the image with the least distortion (least RMSE = 0.056) and the Wimperis antisymmetric composite pulse scheme generated the image with most distortion (greatest RMSE = 0.097). On the basis of these results, the Levitt-Freeman and Tycko et al. CPMG composite pulse sequences and the straight CPMG pulse sequence were selected to show the effect of off-resonance and added noise to signals.

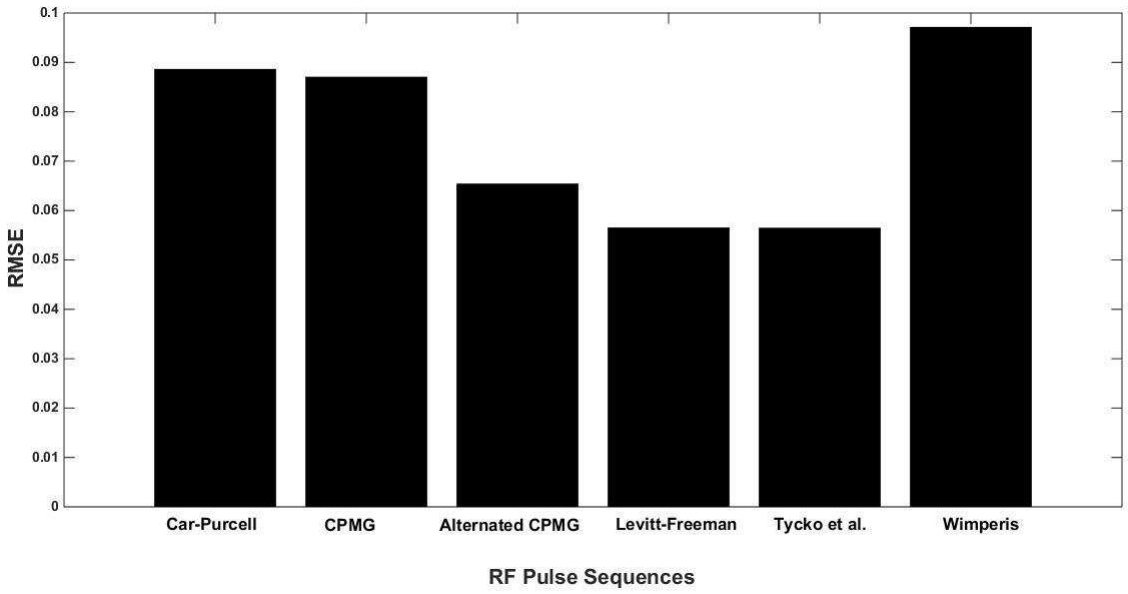

Figure 5.3: Reconstruction errors for the 64×64 phantom simulations without noise and with a homogeneous main B_0 field. The first three bars are for the multiple spin echo standard RF encoding sequences without composite pulses. The last three bars are for the CPMG standard RF encoding sequence using the indicated symmetric, asymmetric and antisymmetric composite pulses.

Figure 5.4 shows the reconstruction errors for the straight CPMG sequence and the two CPMG versions that use Levitt-Freeman and Tycho et al. composite pulses in an inhomogeneous B_0 field. The errors are increased over those shown in Figure 5.3. The RMSE between reconstructed images and the phantom ranged from 0.09 (least distortion) for CPMG Tycko et al. composite pulse sequence to 0.12 (most distortion) for straight CPMG pulse sequence.

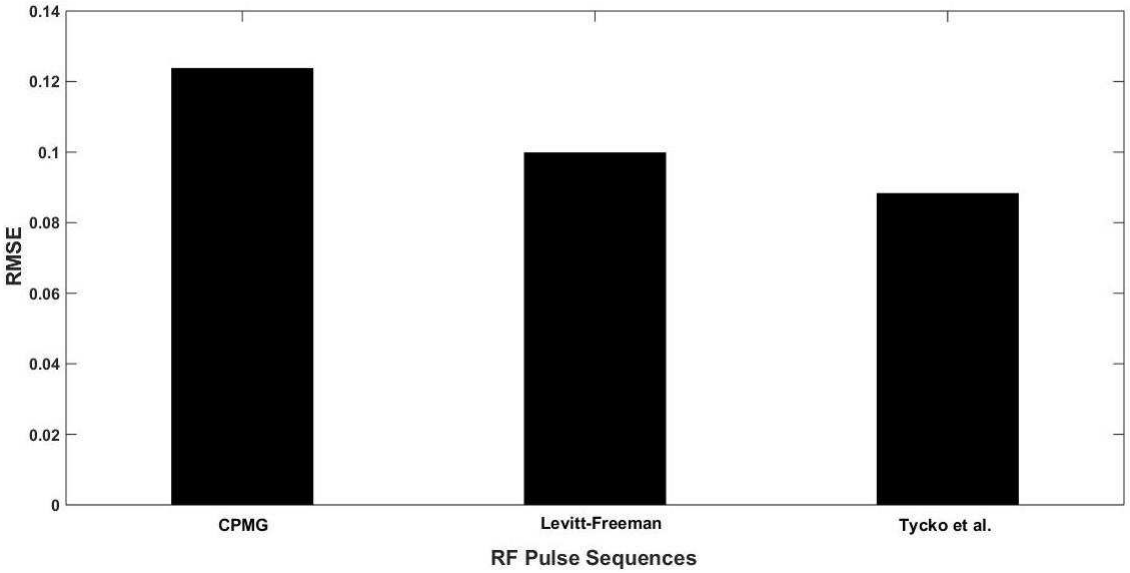

Figure 5.4: Reconstruction errors or the 64×64 phantom simulations without noise and with an inhomogeneous main B_0 field to show the effect of unknown off-resonance on the reconstructions of standard RF encoded data. The CPMG simulation is without composite pules. The Levitt-Freeman and Tycho, et al. composite pulses were used in the CPMG sequence.

The effect of added noise with SNRs of 20 and 50 dB to the straight CPMG, and the Levitt-Freeman and Tycko et al. CPMG pulse sequences in a homogeneous B_0 field is shown in Figure 5.5.

The effect of an unknown ΔB_0 (off-resonance effects) to the straight CPMG, and the Levitt-Freeman and Tycko et al. CPMG pulse sequences is shown in Figure 5.6. The images were reconstructed using LS and LS-TV.

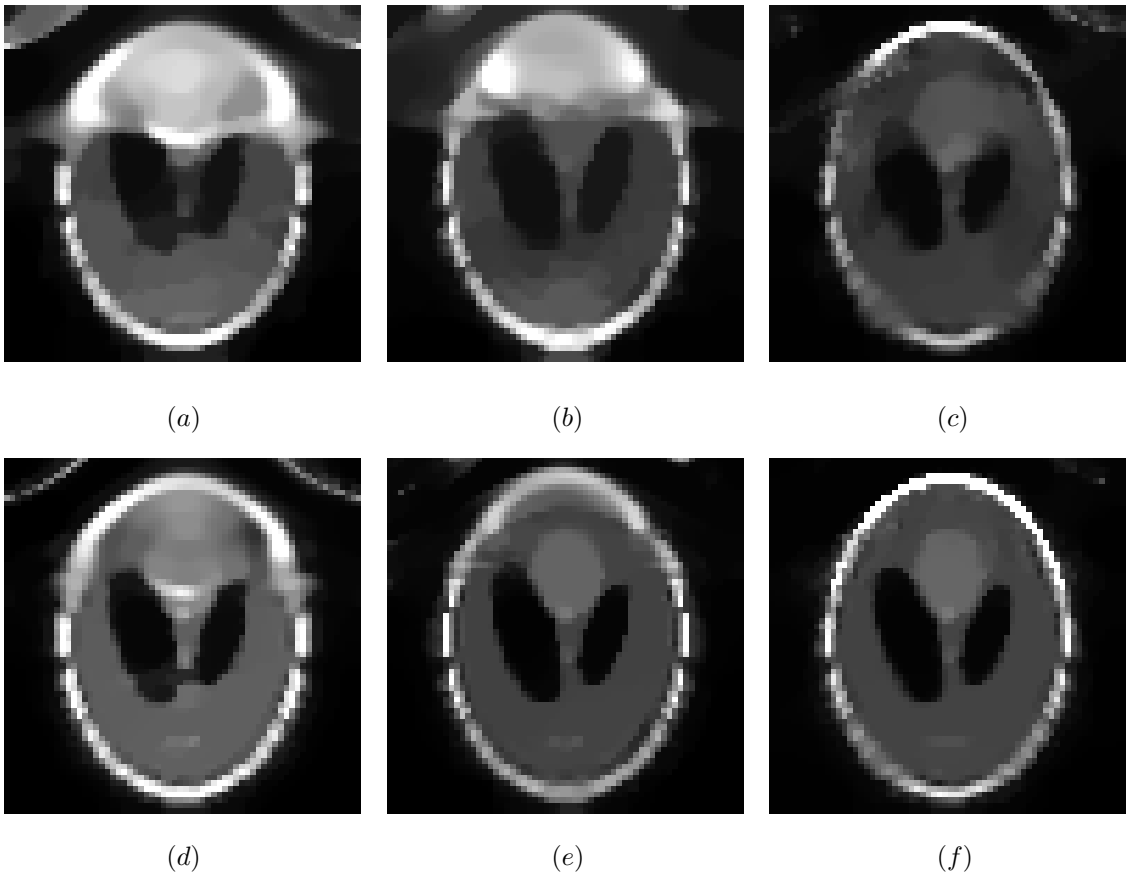

Figure 5.5: The effect of the composite pulses and adding noise to the signals in an homogeneous B_0. The upper and lower rows show images which were reconstructed from signals with noise added at SNR=20 and 50 dB respectively. The first column (a, d) is for the Meiboom-Gill pulse sequence, the second column (b, e) is for the Levitt-Freeman composite pulse sequence and the last column (c, f) is for the Tycko et al. asymmetric composite pulse sequence. All the images were reconstructed using LS-TV method.

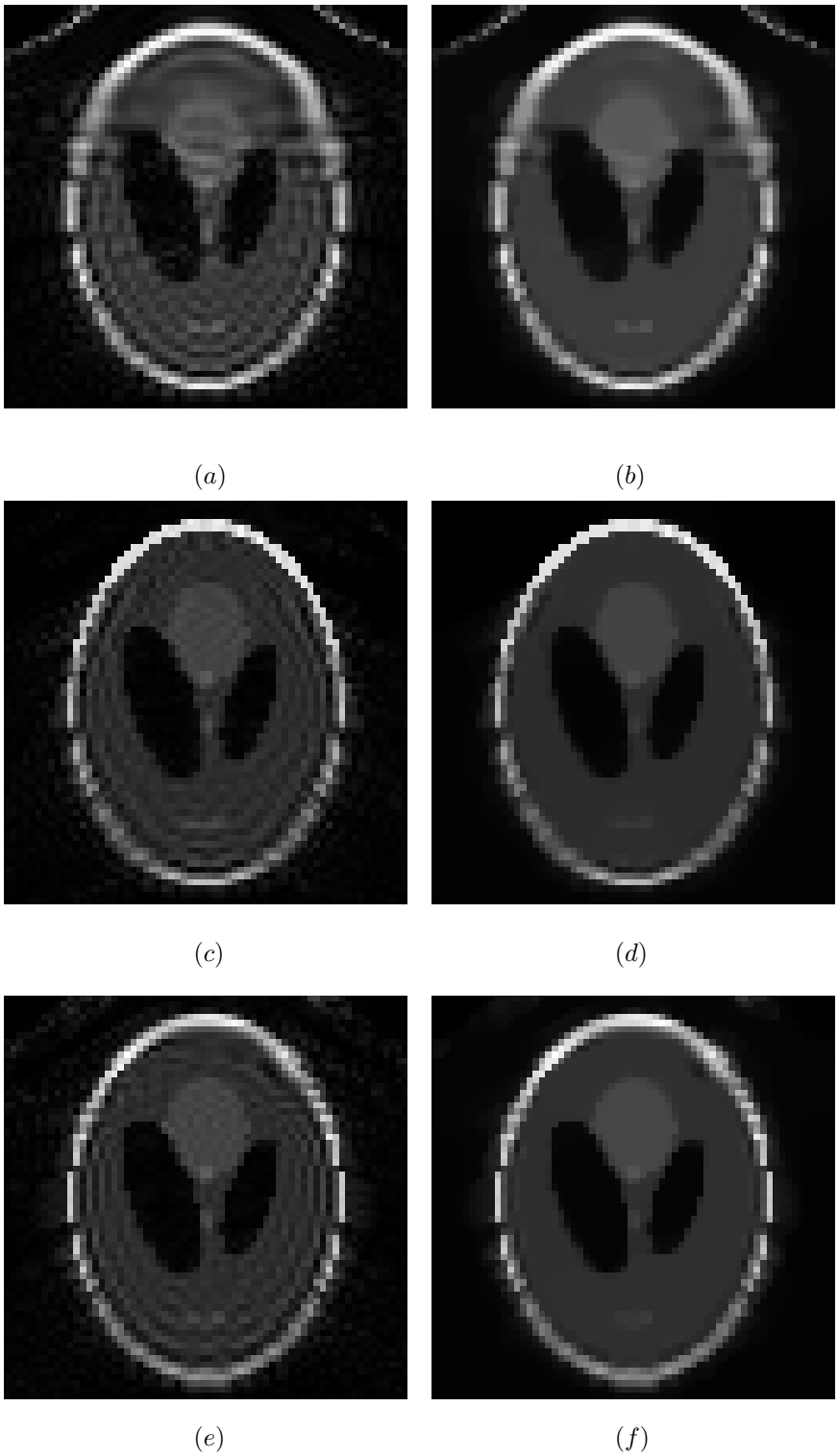

Figure 5.6: The effect of an unknown ΔB_0 (to the reconstruction) of 5 ppm on reconstructed images by adding ΔB_0 to Bloch simulation prior to LS method with and without TV method. (a, b) is for the Meiboom-Grill pulse sequence recostructed using LS method without and with TV method respectively, the second row (c, d) is for the composite pulse sequence proposed by Levitt-Freeman recostructed using LS method without and with TV method respectively, and the last row (e, f) is for the composite pulse sequence proposed by Tycko et al. recostructed using LS method without and with TV method respectively.

5.5 Conclusion

Six RF pulse sequences (three RF pulses that used simple 180° pulses and three CPMG sequences that used composite pulse sequences) were evaluated in detail for their ability to compensate for the effect of the inhomogeneous B_1 field of a cube-shaped RF phase encoding coil on tip angle using a Bloch simulation. The three composite pulses used with CPMG were (a) Levitt-Freeman (symmetric) [80], (b) Tycko et al. (asymmetric) [79] and (c) Wimperis (antisymmetric) [87] which turned out to be the best performing in their individual classes. Amongst the six RF pulse sequences, the CPMG sequence with the symmetric composite pulses proposed by Levitt-Freeman ($90_{90} - 180_0 - 90_{90}$) and asymmetric composite pulse proposed by Tycko et al. ($180_0 - 180_{105} - 180_{210} - 360_{59}$) led to minimal reconstruction errors in a homogeneous B_0 field. The Tycko et al. asymmetric composite pulse was the most appropriate composite pulse in terms of leading to an image that is less distorted when compared against images produced using other pulses in an inhomogeneous B_0 field. However, the Levitt-Freeman composite pulse is composed of less RF pulse pieces and is therefore more time efficient than the Tycko et al. composite pulse.

As composite pulses are composed of a cluster of RF pulses, they take more time than ordinary RF pulses. The time required varies between the composite pulse sequences according to the number of RF pulses they contain. The Wimperis composite pulse has more RF pulses (composed of five RF pulses: $180_{45} - 180_{210} - 180_0 - 180_{90} - 180_{315}$) than other composite pulse sequences, so it requires more time. Other composite pulses have been reported in the literature, also designed to compensate for B_0 and B_1 inhomogeneity, but they were not included in our study because those pulses are composed of even more RF pulses than the ones studied here [83, 87, 103].

The effect of an inhomogeneous B_0 field of 5 ppm was modeled as an unknown B_0 inhomogeneity to the reconstruction and found to be a minor effect when the images were examined visually although there were differences in RMSE. Compensating for a known inhomogeneous B_0 field is nevertheless possible by modeling the inhomogeneities into the encoding matrix $[T]$ of Eq. (4.13), in the same way as the effect of the non-linear RF phase and a known inhomogeneous B_1 field were modeled.

This study suggests that use of symmetric and asymmetric composite pulses in RF encoding sequences leads to images with less distortion than antisymmetric pulses. The symmetric composite pulse proposed by Levitt-Freeman and the asymmetric composite pulse designed by Tycko et al. give the minimum distortion in the reconstruction among other pulses. This is contrary to the conclusion that antisymmetric composite pulses are the best ones to use for spin echo sequences in conventional, B_0 encoded, MRI [104].

Composite pulses have previously been designed for use in conventional MRIs (having gradient coils and non-phase encoding RF coils). This study is the first to examine the feasibility of applying composite pulses to RF phase encoded MRI.

The symmetric composite pulses proposed by Levitt-Freeman and the asymmetric composite pulse designed by Tycko et al. emerged as the most promising ones to use with RF encoded MRI to compensate for inhomogeneous B_1 fields when B_0 is homogeneous. The asymmetric composite pulse designed by Tycko et al. emerged as the most appropriate one to use when both inhomogeneous B_1 and off-resonance effects are a concern.

All details about signal encoding and image reconstruction for RF phase encoded MRI was presented. RF phase encoded MRI is possible and could remove the need for gradient coils and lead to a cheaper and lighter MRI. To have a portable MRI, the shim coils need to

be removed in addition to gradient coils which will be discussed in the next chapter. Moreover in the next chapter, the developed image reconstruction techniques from chapters 4 and 5 will be tested experimentally.

Chapter 6

Image Reconstruction of Experimental Data of Rotating Magnet and RF Coils

6.1 Introduction

To have a truly portable MRI, the need for shim coils and other B_0 homogeneity requirements must also be removed along with the need for gradient coils. The idea of using an inhomogeneous B_0 field to encode information has been used to encode the depth of water. A 1D inhomogeneous permanent magnet (rare-earth magnets) was used to encode information [105, 106]. Cooley et.al [45, 107] designed a portable MRI which does not need shim coils and other B_0 homogeneity requirements. In fact this MRI takes advantage of the inhomogeneous fields to encode information in 2D dimensions. They used an inhomogeneous B_0 field pattern and eight channel receiver array for spatial encoding. An inhomogeneous B_0 field was generated using a rotating permanent Halbach magnet.

Our rotating MRI is a wrist size MRI which uses an inhomogeneous field to encode information in 2D. Since the rotating MRI uses inhomogeneous B_0 fields to encode spatial information, there is no need for gradient coils to encode information or shim coils and other B_0 homogeneity requirements to homogenize the main magnet.

A Halbach magnet was used to generate a non-uniform radially-varying B_0 field, such that intended image plane was perpendicular to the axis of the main magnet (see Figure 2.4). The

static field is approximately parabolic inside the rotating MRI which means that the Larmor frequency is a function of radius, so the non-uniform radially-varying B_0 field can be used to encode information in the radial direction. To encode information in the angular direction, the rotating magnet uses two RF receiver coils which are fixed related to the main magnet, but both the receives and the main magnet rotate around the sample using a stepper motor.

The rotating MRI uses a non-linear spatial encoding magnet field, so Fourier transform can not be used to reconstruct images. A least squares method followed by a total variation technique (LS-TV) were used instead of FT to reconstruct the images.

To reconstruct the images using LS-TV method an accurate map of B_0 and the B_1 field in the FOV is required. In "Methods" section, the approaches taken to measure the main magnet field are described, pulse sequences used to get MRI data are given, the B_1 field is simulated and the reconstruction method to get the image is discussed. Results from the simulated and experimental data are presented in the "Results" section.

6.2 Methods

A Halbach magnet was used to generate an inhomogeneous radially-varying B_0 field with average strength of 80 mT. To measure the B_0 field, three different approaches were taken. In the first method, B_0 field was calculated using a simulation software based on multi-dipole expansion. B_0 field was also measured experimentally using static field probe and NMR. To reconstruct the images accurately, in addition to the map of B_0 field, the map of the receiver fields was also required. Two separate saddle receiver coils were located 180^0 from each other. The receiver coils were fixed relative to the magnet and both rotated around the imaged object using a stepper motor (see Figure 6.1). The rotation enables spatial encoding

in the angular direction through variation of the receiver B_1 field relative to the object.

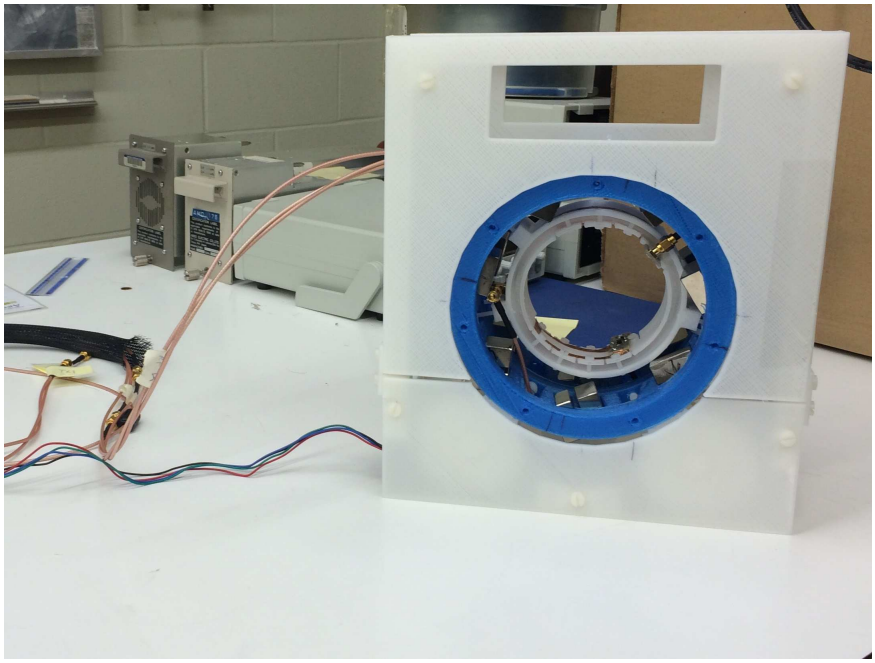

Figure 6.1: The Halbach magnet configuration and the two Saddle receiver coils in y direction (up-down). The figure shows the whole rotating MRI configuration including the main magnet, RF receivers, stepper motor and wires for transfering energy to receiver and transmitter RF coils. B_0 field direction was in the x direction (left-right), B_1 receiver field direction was in y direction and B_1 transmit field was in the z direction (magnet axis).

In the experiment reported here, 32 angular positions were used. The magnet rotated in a specific pattern of angles of [0 3 10 13 20 26 30 36 46 52 56 62 68 72 78 82 88 95 98 105 115 121 125 131 137 141 147 151 157 163 167 173](in degree) . Also 44 transmission frequencies were used for radial encoding in the inhomogeneous B_0 field. The whole experiment took about 15 minutes. For our model the receiver bandwidth was 250 kHz, the center frequency was 3437.5 kHz, and the γ was 42.5 MHz/T. Therefore the range of B_0 field, corresponding to the nuclei that could be excited was $77.9 - 83.8$ mT. In the experiment, the nuclei corresponding to the B_0 field in the range of $79.5 - 83.8$ mT were selected to be excited. To model the sensitivity of the receiver coils, the Biot Savart's law (Eq. (3.2)) was used to calculate B_1

field of each receiver coil for different positions in the FOV.

6.2.1 Main Magnetic Field Measurement

The magnet was a permanent Halbach magnet configuration of 24 cubes with 1 inch on each side to generate a magnetic field with magnitude average of 0.08 T. A 3D printer was used to build the structure to hold 24 cubes. The 3D printer material was Polylactic Acid (PLA).

Simulation

The Halbach magnet generates an approximately parabolic B_0 field inside the rotating MRI. The B_0 field was simulated using a simulation software which generates the field based on multi-dipole expansion (see Figure 6.2). The simulation measurement was provided by Logi Vidarsson from LT imaging company.

Using Static Field Probe

In order to create an accurate image we need to know the exact map for B_0 field inside the rotating magnet, therefore B_0 field needs to be measured experimentally. A static field probe was used to measure the B_0 field inside the FOV. The probe had 5 Hall effect sensors. One sensor measured B_0 magnitude along the z axis, two measured B_0 magnitude along the y axis (an average was taken to provide a measurement along the y axis of the probe center) and two measured B_0 magnitude along the x axis (an average was taken to provide a measurement along the x axis of the probe center). The sensors were Allegro Micro Systems Hall effect sensors which mounted on a delrin (a non-magnetic material) cylinder (see Figure 6.3).

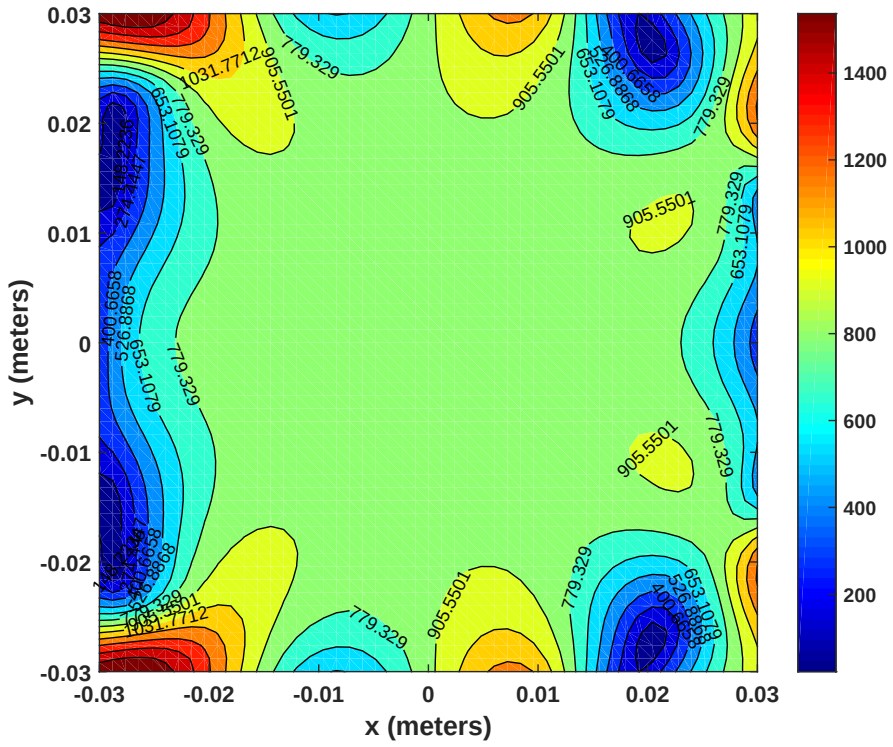

Figure 6.2: Calculated distribution of B_0 field map using a simulation software. The map was generated from a matrix of 51×51 measurements for B_0 filed which was provided by LT imaging company. The range of the B_0 field in the middle of the FOV varies from 79-90 mT.

A Computer Numerical Control (CNC) machine was used to move the probe inside the rotating field MRI to measure the B_0 field at different positions (see Figure 6.4). A C code was written to show the movement path for the CNC machine in 2D. This C script was then converted to G-code using the available software with the CNC machine. The G-Code was used to interact with an Arduino microcontroller board to control the motors of the CNC machine to move the machine to given positions. The given positions were 1 mm apart from each other. The static probe will move by the CNC to each position, because it is attached to the CNC machine (see Figure 6.5). At each given position the B_0 field is measured along the x, y and z directions and is stored in a text file. Figure 6.6 shows the map of B_0 field inside the rotating MRI using the average of measurements from the static probe experimentally. The experiment was performed five times on different days and then an average was used to

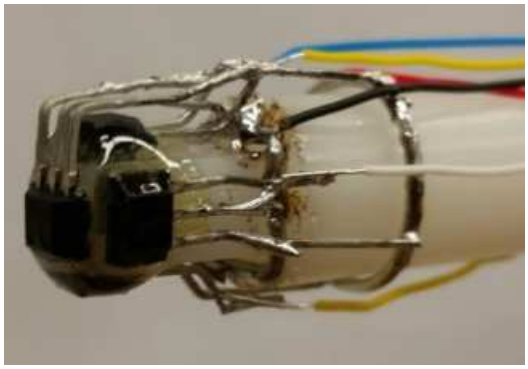

Figure 6.3: The 5 Hall effect sensors were mounted on a derlin cylinder to measure the B_0 field in the x, y and z directions. One sensor measured the B_0 field in the z direction, two measured the B_0 field in the x direction and two measured the B_0 field in the y direction. The sensors are Allegro Micro Systems Hall effect sensors.

map the B_0 field. The experiment was also done in an RF shielded room in the Department of Physics and Engineering Physics of University of Saskatchewan.

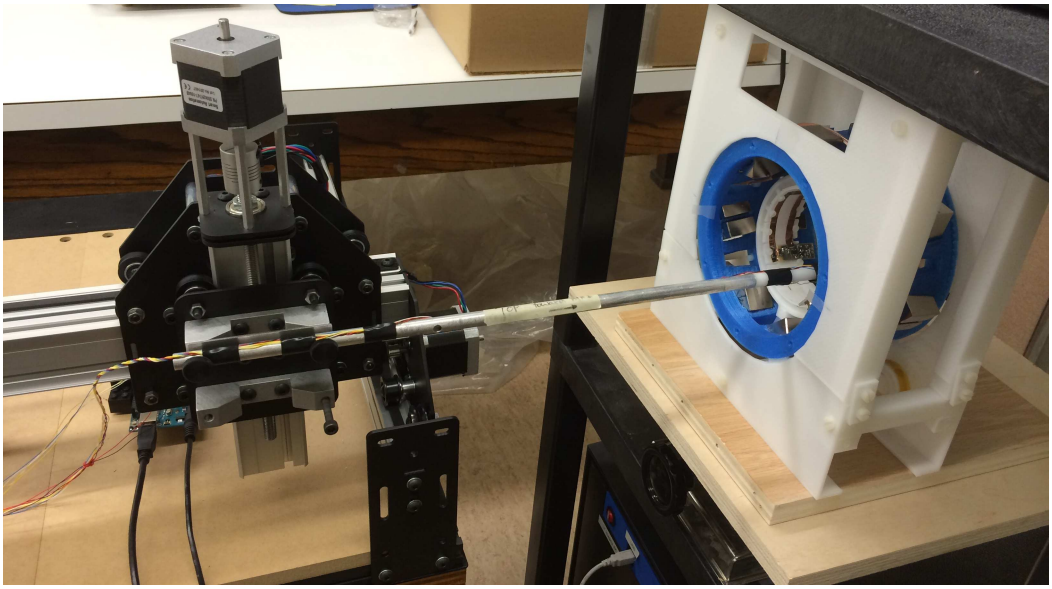

Figure 6.4: A CNC machine used to move the probe inside the rotating field MRI. The CNC machine is Shapeoko 2 stepper motor system.

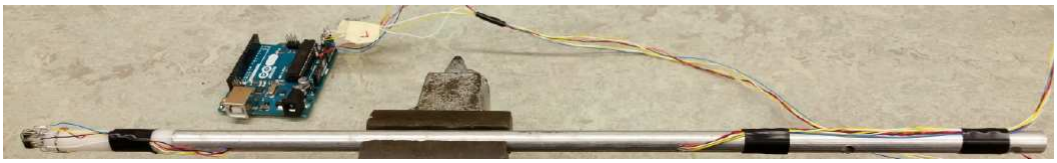

Figure 6.5: The probe was mounted on an aluminum rod which was attached to the CNC machine.

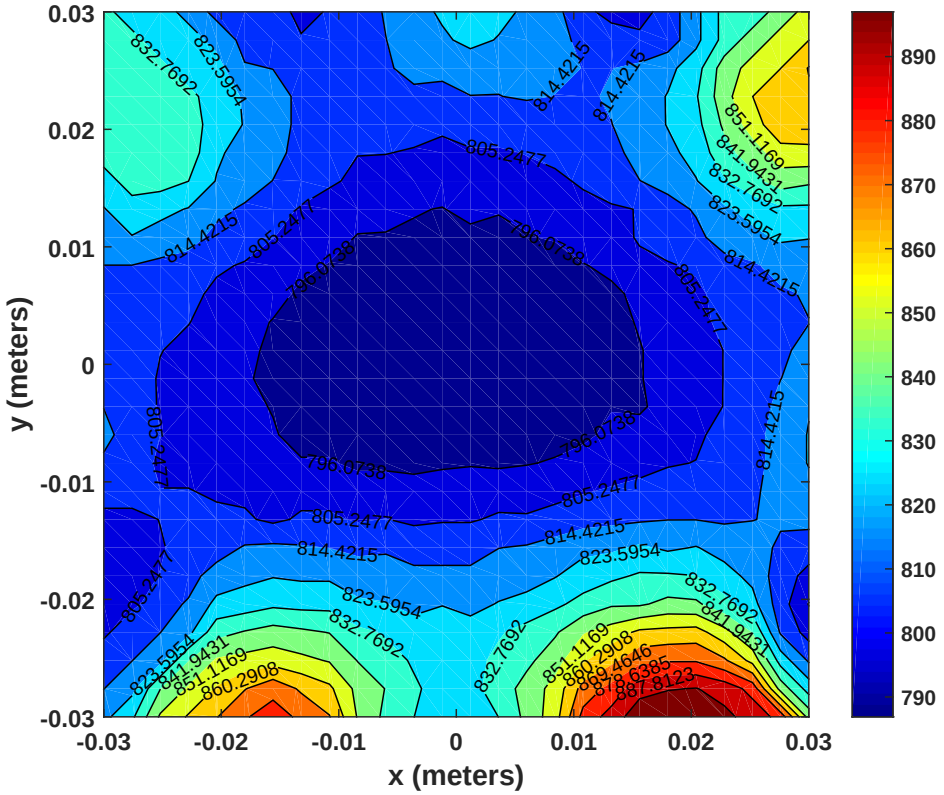

Figure 6.6: The contours of B_0 field inside the FOV obtained using the probe measurements. The B_0 field was measured in each positions five times and then an average was used to map the B_0 field. The given positions where the probe was moved to measure the B_0 field, were 1 mm apart from each others. The minimum amount of the B_0 field is about 78.3 mT located in the middle. The range of the B_0 field in the middle of the FOV varies from 78.3-79.6 mT.

Using NMR

NMR was another method used to measure the magnetic field. In this method a point source was moved inside the rotating MRI using the CNC machine. The point source signal was then measured for a range of transmission frequencies at each position inside the rotating field MRI. At each position, the maximum amount of signals and the corresponding frequency was found. From the known corresponding frequency in each position, the magnetic field at that position was calculated using the equation of $B_0 = f/\gamma$, where B_0 is the amount of the magnetic field in each position, f is the corresponding measured frequency and γ is the gyromagnetic ratio.

To measure the signal a capillary tube was used as a point source signal. The tube was filled with mineral oil and mounted on an aluminum rod was attached to the CNC machine (see Figure 6.7). The CNC machine moved the tube inside the rotating field MRI. The CNC machine was stopped at each position, so the signal could be measured for the point source in that position. This step was repeated until the signal from all different positions inside the rotating field MRI was measured.

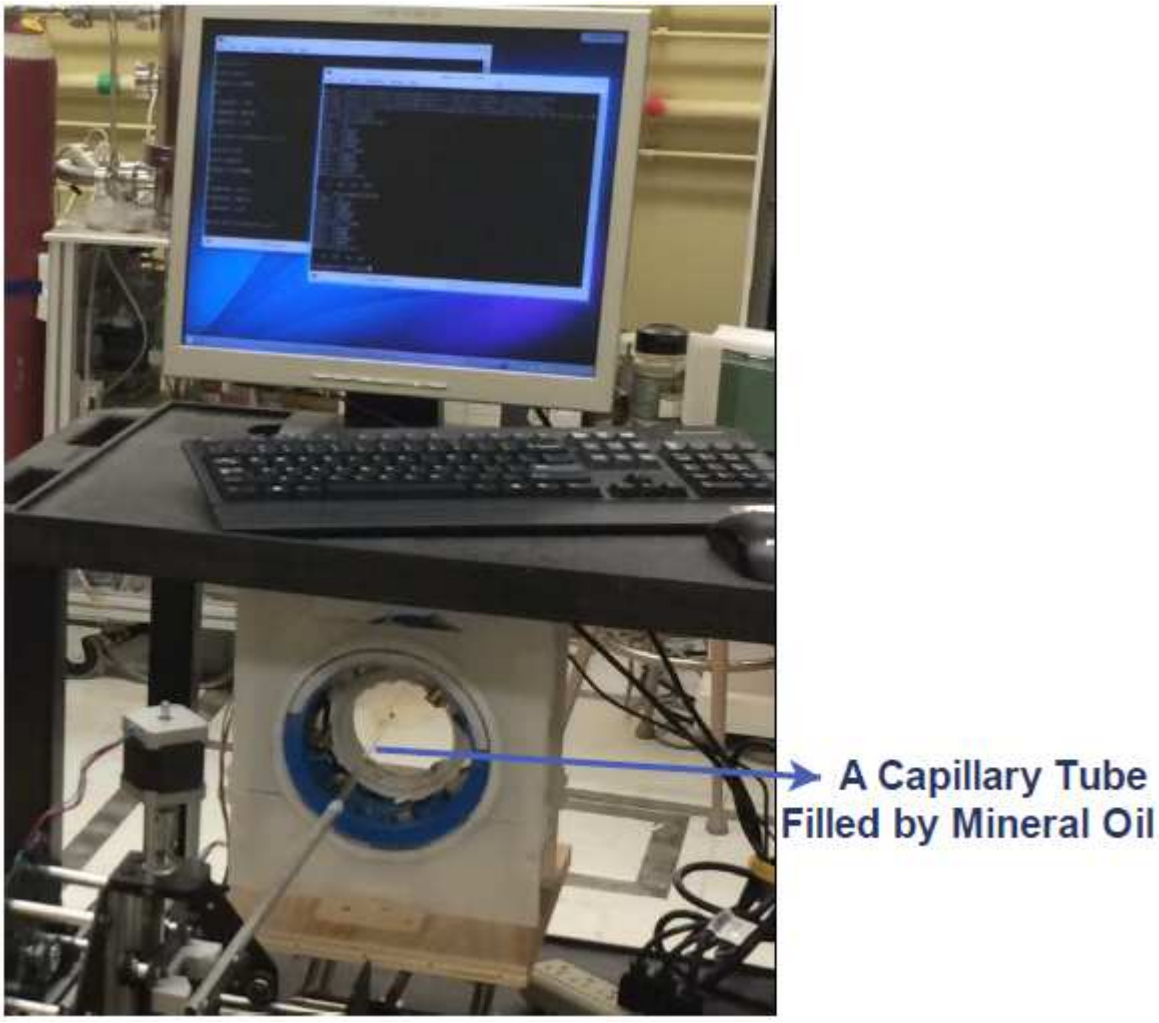

Figure 6.7: A capillary tube filled with mineral oil and mounted on an aluminum rod which was moved inside the magnet using a CNC machine.

6.2.2 Pulse Sequence

An RF pulse sequence was a series of square low flip angle pulses similar to a gradient echo pulse sequence. An RF spoiling pulse consisting of a 4-phase quadratic phase cycling scheme of $90^0 - 180^0 - 0^0 - 270^0$ [108] was used to avoid unwanted coherence buildup. The pulse sequence trains was provided by LT imaging company.

6.2.3 Receiver RF Coil sensitivity profiles

Two separate saddle receiver coils were located 180^0 from each other. The receiver coils were implemented in a low field strength of 0.08 T. At such a low field strength, the coil tissue interactions are negligible because the RF coils are small compared to the wavelength of the RF field inside the biological tissue. Therefore a prior field map can be used in the image reconstruction algorithm. Also at low field, a quasistatic field approximation can be used to calculate the B_1 field because the RF frequency is low. In other words, B_1 field can be calculated using the Biot-Savart's Law (Eq. (3.2)). Figure 6.8 shows the map of B_1 contours obtained from of the saddle coil.

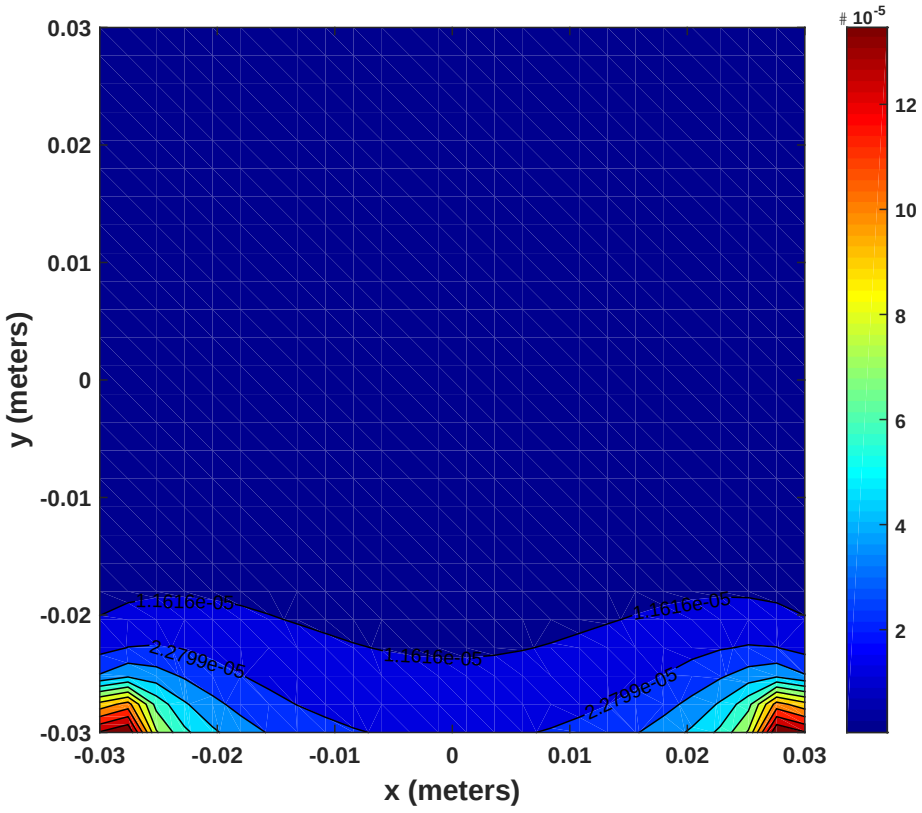

Figure 6.8: The contours of the sensitivity of one of the receiver RF field inside the FOV obtained the Biot-Savart's Law.

6.2.4 Image Reconstruction

Signal Equation

B_0 field was first measured experimentally for a few points inside the FOV. B_0 field was computed for all points inside the FOV using curve fitting toolbox in Matlab. Two separate saddle receiver coils were located 180^0 from each other. To model the sensitivity of the receiver coils, the Biot Savart law was used to calculate the B_1 field of each receive coil at different positions inside the FOV. When the B_0 and B_1 map are known, the image can be reconstructed as is discussed bellow.

The detected signal from object x, indexed by transmission frequency ω and magnet position α can be modeled as:

$$y(\omega, \alpha) = \int \int x(r, \theta) A(\omega, \alpha; r, \theta)\, dr\, d\theta \tag{6.1}$$

where A is the encoding matrix and (r, θ) are polar coordinates. A Riemann sum approximation of Eq. (6.1) was used to compute the simulated signal. After rearrangement, Eq. (6.1) can be written as: $[y] = [A][x]$. The encoding matrix for each excitation, at frequency ω (for radial encoding) and rotation α, can be calculated as:

$$A(\omega, \alpha) = B_{\text{weight}}(\omega, \alpha) B_1(\alpha) e^{\triangle B_0(\omega,\alpha)\gamma \triangle T} \tag{6.2}$$

In Eq. (6.2) $B_1(\alpha)$ is the component of the RF receiver field perpendicular to the B_0 direction which changes relative to the imaged object at each magnet angular position and can be calculated as:

$$B_1 = \sqrt{B_{1x}^2 + B_{1y}^2}\sin(\phi_{B_1} - \phi_{B_0}) \tag{6.3}$$

Where ϕ_{B_1} is the phase of B_1 field at each angular position and ϕ_{B_0} is the phase of B_0 field. For each excitation the slice thickness (radially) is a sinc function which means the nuclei with the same resonant frequency are excited completely and then others according to how far they are from the Larmor frequency are excited. Therefore the coil sensitivity is multiplied by a weighing matrix. The weighting matrix for each excitation and rotation is:

$$B_{\text{weight}}(\omega, \alpha) = \mid \frac{\sin(\triangle B_0(\omega, \alpha))}{\triangle B_0(\omega, \alpha)} \mid \tag{6.4}$$

where $\triangle B_0$ is the difference of B_0 field from the Larmor frequency field:

$$\triangle B_0(\omega, \alpha) = B_0(\alpha) - B_\omega(\omega) \tag{6.5}$$

where $B_0(\alpha)$ is the measured B_0 field at each rotation angle and $B_\omega(\omega)$ is the Larmor frequency magnetic field as determined by the transmitted frequency.

Iterative Reconstruction Method

The image $[x]$, from $[y] = [A][x]$, was reconstructed using a regularized LS method (as described in chapter 4 (see Eq. (4.19)). The TV method was next used to further decrease artifacts (as described in chapter 5 (see Eq. (5.18)). Let M be the number of frequencies that we want to transmit at each rotation, R be the number of angular positions we want to rotate the magnet to (main magnet and the receive coils rotate together), C be the number of the receiver coils, and $N \times N$ be the number of image pixel. Then matrix $[A]$ is of size $MRC \times N^2$, $[y]$ is a vector of size $MRC \times 1$ and, $[x]$ is a vector of size $N^2 \times 1$.

6.3 Results

A Shepp-Logan phantom was used to simulate the image reconstruction. Figure 6.9 shows the reconstructed image from Shepp-Logan phantom using LS-TV method.

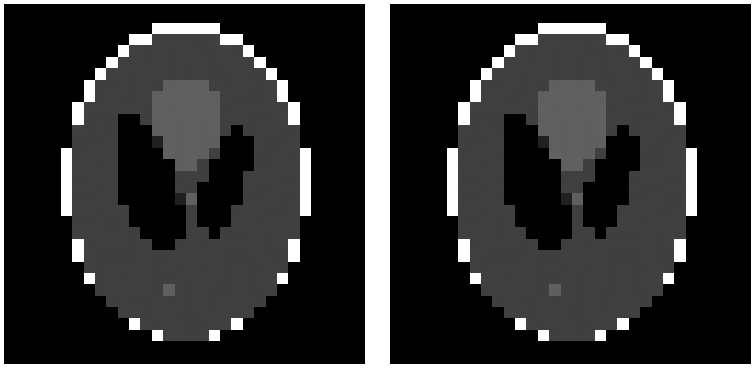

(a) (b)

Figure 6.9: Reconstructed images from noiseless signals from Shepp-Logan phantom. (a) shows Shepp-Logan phantom and (b) shows reconstructed image from a phantom of 32×32 pixel size.

Two phantoms, a circular bottle and a cubic bottle filled with mineral oil, were used for experimental part. 32 angular positions and 44 transmission frequencies were used to give enough projection (see Figure 6.10).

Figure 6.11 depicts the reconstructed images from the circular phantom filled with mineral oil, the circular phantom half filled with mineral oil and the cubic phantom filled with mineral oil.

(a) (b) (c)

Figure 6.10: The figure shows the two phantoms used inside the rotating field MRI to generate the signals. The images were taken through the Axial plane. (a) shows the circular bottle phantom. (b) shows the cubic bottle phantom. (c) shows the the circular tube phantom half filled with mineral oil inside the MRI.

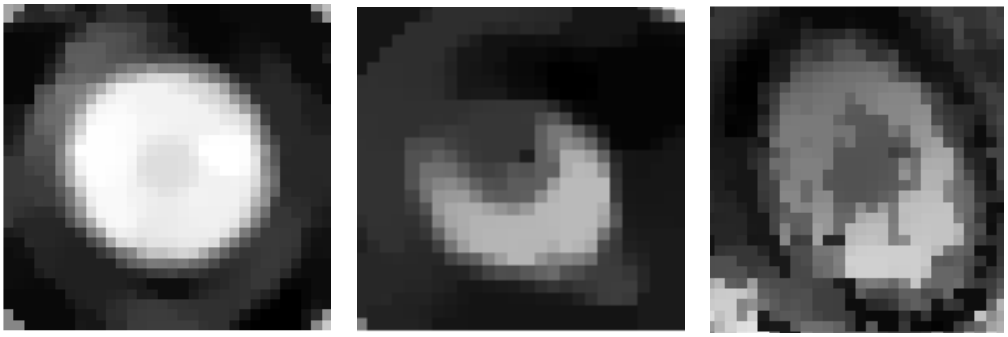

(a) (b) (c)

Figure 6.11: The figure shows the reconstructed images from two phantoms using LS-TV method.(a) The reconstructed image of a full filled circular tube phantom inside the MRI. (b) The reconstructed image of a half filled circular tube phantom inside the MRI. (c) The reconstructed image of a full filled cubic tube phantom inside the MRI.

6.4 Discussion

In this chapter, the feasibility of image reconstruction from the portable rotating MRI system was shown. A Halbach magnet was used to generate an inhomogeneous radially-varying B_0 field that can be used for spatial encoding in the radial direction. The B_0 field was measured experimentally. Two separate saddle receiver coils were located 180^0 from each other. To model the sensitivity of the receiver coils, the Biot Savart law was used to calculate the B_1 field of each receiver coil at different positions in the FOV.

The measured signals were noisy because the MRI system itself generates some noise as well. TV technique was therefore used to remove noise. Using regularized LS method without the TV technique resulted in noisy images. Noise removed was attempted by subtracting measured signals from the background noise. Background noise is the signal measured with no phantom inside the rotating MRI.

Our reconstruction method was very sensitive to accurate measurements of B_1 and B_0 magnitudes. In this experiment, the B_1 map was simulated theoretically using Biot-Savart law. If B_1 field can be measured experimentally, the reconstructed images may have less distortion due to more accurate B_1 map. B_0 field was measured experimentally using field probe. There were few errors in measuring the field. Some of the errors were due to inaccurate sensors, inaccurate corresponding position to the measured B_0 (the probe had some vibrations), and inaccurate the starting positions (starting position of receiver coils, magnet configuration, and the probe).

B_0 was also measured using NMR to validate our experimental measurements. However, the results were not useful. It is thought that the measured signal from point source phantom was very weak, because the receiver coils were far from the point source phantom. Better

results could be obtained if a loop as a receiver coil was used and kept it around the point source phantom.

A blurred point was observed at the image center. The reason for not being able to get a better resolution at the center was that the gradient of the main magnet is zero at the image center. The zero gradient position does not change with rotating the magnet and therefore information can not be encoded at the image center. In other words both the RF field and the magnetic field have a blind-spot at the same position which is at the image center.

Our results indicate the feasibility of reconstructing images from non-uniform rotating magnet. The reconstructed images from experimental data, however, included artifacts which were likely due to the high sensitivity of the reconstruction method to the assumed B_0 and B_1 field values. There were, as yet unquantified, errors associated with measuring the B_0 field. As well, the calculated B_1 field may be not be an accurate approximation to the actual field.

6.5 Conclusion

Progress was made in the realization of a novel new approach to MRI that does not rely on active magnetic gradient fields and shim coils and other B_0 homogeneity requirements. The results indicated the feasibility of reconstructing images from a non-uniform rotating magnet.

Chapter 7

Conclusion

7.1 Summary of work

The objective of my thesis was to show the feasibility of image reconstruction of MR signals from two different portable MRI systems. One of the portable MRI system was RF phase encoded MRI which uses non-linear varying RF phase to encode information instead of using B_0 gradient coils. Using a non-linear RF phase encoded coil results in a bigger FOV and less complicated RF coil design. However, in B_1 encoded MRI, a realistic non-linear RF phase encoding coil generates an inhomogeneous B_1 field that leads to spatially dependent flip angles. It is therefore needed to compensate for the B_1 inhomogeneity. The effect of B_1 inhomogeneity on tip angles for conventional B_0 encoded MRI, may be minimized using composite pulses. We explored the feasibility of using composite pulses with non-linear RF phase encoding coils to identify the most appropriate composite pulse scheme.

Another portable MRI was a rotating MRI which uses non-uniform radially varying B_0 field to encode information instead of using B_0 gradient coils. The rotating magnet has a permanent Halbach magnet and two Saddle receiver coils which rotate around the object being imaged. We used two different phantoms to generate the signals.

For the RF phase encoded MRI we simulated the signals, but for the rotating magnet we measured the signals experimentally. We used a constrained LS method with Tikhonov

regularization to reconstruct the images. TV method was also used along with the LS method to remove noise.

7.2 Future Directions

2D imaging was performed for both MRI systems. The implementation of 3D imaging can be considered for the future. 3D imaging is possible in different ways:

1. Using RF phase encoded coils to encode information in all three directions.

2. Using RF phase encoded coils to encode information in 2D and B_0 gradient coils along the other direction.

3. Using RF phase encoded coils to encode information in 2D and non-uniform B_0 field along the other direction.

4. Using rotating magnet and receiver coils to encode information in 2D and RF phase encoded coils in another direction.

We simulated the signals inside an RF phase encoded MRI system. Building a MRI and trying to reconstruct images from real data is a potential future work.

We applied different existing composite pulses in the literature to the RF phase encoded MRI. Future work can be focused on customizing a composite pulse specific to our system using different methods for designing composite pulses.

We reconstructed the images using LS-TV. Alternative methods such as non-linear FT[109], Algebraic Reconstruction Techniques (ART) [110], Randomized Kaczmarz [111], and conjugate gradients [112] can be used to reconstruct the images.

To reconstruct the images from the rotating MRI accurate measurements of B_1 and B_0 fields was needed. B_1 field was calculated theoretically in this study. One can try to measure the B_1 field experimentally and then use the accurate measurement to reconstruct the images. More accurate sensors can be used to obtain a more accurate measurement of B_0 field.

Another potential work, in rotating MRI can be shifting the place of zero gradient magnetic field off the image center. As such the place of zero gradient varies with rotating the magnet. Information can therefore be encoded at all positions.

7.3 Conclusion

Non-linear RF phase encoded MRI has a bigger FOV with less complicated RF coil design. Since the phase is non-linear, reconstructed images using the FT had some distortion, specially around the boundaries, and it was therefore required to use another technique to reconstruct the images. MRI signals encoded in B_1 fields with non-linearly varying spatial phase can be accurately reconstructed using regularized least squares thus pointing the way to the usage of simple RF coil designs for RF encoded MRI.

Non-linear RF phase encoded coil generates an inhomogeneous B_1 field which affects flip angles. Different composite pulses were evaluated to compensate for B_1 inhomogeneities. An asymmetric composite pulse scheme created images with fewer artifacts than other composite pulse schemes in inhomogeneous B_0 and B_1 fields which made it the best choice for decreasing the effects of spatially varying flip angles. This is not in agreement to the conclusion that antisymmetric composite pulses are the best ones to use for spin echo sequences in conventional B_0 encoded MRI.

For the rotating magnet MRI the signals were reconstructed using LS-TV. The images

were partially distorted which presumably was because the image reconstruction method was highly sensitive to the accuracy of B_0 and B_1 field. If accurate measurements for B_0 and B_1 fields are provided, images without artifacts can therefore be generated.

References

[1] D. Brenner and H. Hricak, "Radiation exposure from medical imaging: Time to regulate?," *JAMA*, vol. 304, no. 2, pp. 208–209, 2010.

[2] L. Medina, K. Applegate, and C. Blackmore, *Evidence-based imaging in pediatrics : optimizing imaging in pediatric patient care.* New York : Springer, 2010.

[3] M. Pearce, J. Salotti, M. Little, K. McHugh, C. Lee, K. Kim, N. Howe, C. Ronckers, P. Rajaraman, A. Craft, L. Parker, and A. Berrington de Gonzalez, "Radiation exposure from CT scans in childhood and subsequent risk of leukaemia and brain tumours: a retrospective cohort study," *The Lancet*, vol. 380, no. 9840, pp. 499–505, 2012.

[4] G. Sarty and A. Obenaus, "Magnetic resonance imaging of astronauts on the international space station and into the solar system," *Can. Aeronaut. Space. J.*, vol. 58, no. 1, pp. 60–68, 2012.

[5] J. C. Sharp and S. B. King, "MRI using radiofrequency magnetic field phase gradients," *Magn. Reson. Med.*, vol. 63, no. 1, pp. 151–161, 2010.

[6] P. Mansfield, P. M. Glover, and J. Beaumont, "Sound generation in gradient coil structures for MRI," *Magn. Reson. Med.*, vol. 39, no. 4, pp. 539–550, 1998.

[7] E. Amaro Jr., S. Williams, S. Shergill, C. Fu, M. MacSweeney, M. Picchioni, M. Brammer, and P. McGuire, "Acoustic noise and functional magnetic resonance imaging: Current strategies and future prospects," *J. Magn. Reson. Imaging.*, vol. 16, no. 5, pp. 497–510, 2002.

[8] P. Bandettini, A. Jesmanowicz, J. Van Kylen, R. Birn, and J. Hyde, "Functional MRI of brain activation induced by scanner acoustic noise," *Magn. Reson. Med.*, vol. 39, no. 3, pp. 410–416, 1998.

[9] D. Hall, M. Haggard, M. Akeroyd, A. Summerfield, A. Palmer, M. Elliott, and R. Bowtell, "Modulation and task effects in auditory processing measured using fMRI," *Hum. Brain Mapp.*, vol. 10, no. 3, pp. 107–119, 2000.

[10] R. Brummett, J. Talbot, and P. Charuhas, "Potential hearing loss resulting from MR imaging," *Radiology*, vol. 169, no. 2, pp. 539–540, 1988.

[11] Q. Deng, S. B. King, V. Volotovskyy, B. Tomanek, and J. C. Sharp, "B_1 transmit phase gradient coil for single-axis TRASE RF encoding," *Magn. Reson. Imaging.*, vol. 31, no. 6, pp. 891–899, 2013.

[12] P. C. Lauterbur, "Image Formation by Induced Local Interactions: Examples Employing Nuclear Magnetic Resonance," *Nature*, vol. 242, no. 5394, pp. 190–191, 1973.

[13] P. Mansfield and P. Grannell, "Nmr diffraction in solids?," *J. Phys. C. Solid. State.*, vol. 6, no. 22, pp. L422–L426, 1973.

[14] L. Seeger, "Physical principles of magnetic resonance imaging," *Clin. Orthop. Relat. Res.*, no. 244, pp. 7–16, 1989.

[15] E. Haacke, R. Brown, M. Thompson, and R. Venkatesan, *Magnetic Resonance Imaging.* John Wiley and Sons, Inc., Canada, 1999.

[16] M. Vlaardingerbroel and J. den Boer, *Magnetic Resonance Imaging Theory and Practice.* Springer, 2003.

[17] S. Young, *Magnetic Resonance Imaging Basic Principles.* Raven Press-New York, 1988.

[18] C. Westbrook, *MRI at a Glance.* Blackwell Science, 2002.

[19] S. Ljunggren, "A simple graphical representation of fourier-based imaging methods," *J. Magn. Reson.*, vol. 54, no. 2, pp. 338–343, 1983.

[20] V. K. D. Weishaupt and B. Marincek, *How Does MRI Work.* Springer, 2003.

[21] J. Schenck, "Safety of strong, static magnetic fields," *J. Magn. Reson. Imaging*, vol. 12, no. 1, pp. 2–19, 2000.

[22] J. Schenck, "Physical interactions of static magnetic fields with living tissues," *Prog. Biophys. Mol. Biol.*, vol. 87, no. 2-3 SPEC. ISS., pp. 185–204, 2005.

[23] D. Parker and J. Hadley, "Multiple-region gradient arrays for extended field of view, increased performance, and reduced nerve stimulation in magnetic resonance imaging," *Magn. Reson. Med.*, vol. 56, no. 6, pp. 1251–1260, 2006.

[24] J. Hennig, A. M. Welz, G. Schultz, J. Korvink, Z. Liu, O. Speck, and M. Zaitsev, "Parallel imaging in non-bijective, curvilinear magnetic field gradients: a concept study.," *MAGMA*, vol. 21, no. 1-2, pp. 5–14, 2008.

[25] G. Galiana, J. Stockmann, L. Tam, D. Peters, H. Tagare, and R. Constable, "The role of nonlinear gradients in parallel imaging: A k-space based analysis," *Concepts. Magn. Reson. Part. A. Bridg. Educ. Res.*, vol. 40 A, no. 5, pp. 253–267, 2012.

[26] G. Schultz, P. Ullmann, H. Lehr, A. Welz, J. Hennig, and M. Zaitsev, "Reconstruction of MRI data encoded with arbitrarily shaped, curvilinear, nonbijective magnetic fields," *Magn. Reson. Med.*, vol. 64, no. 5, pp. 1390–1404, 2010. cited By 42.

[27] J. P. Stockmann, P. A. Ciris, G. Galiana, L. Tam, and R. T. Constable, "O-space imaging: Highly efficient parallel imaging using second-order nonlinear fields as encoding gradients with no phase encoding," *Magn. Reson. Med.*, vol. 64, no. 2, pp. 447–456, 2010.

[28] D. Gallichan, C. A. Cocosco, A. Dewdney, G. Schultz, A. Welz, J. Hennig, and M. Zaitsev, "Simultaneously driven linear and nonlinear spatial encoding fields in MRI.," *Magn. Reson. Med.*, vol. 65, no. 3, pp. 702–14, 2011.

[29] W. Kyriakos, L. Panych, D. Kacher, C.-F. Westin, S. Bao, R. Mulkern, and F. Jolesz, "Sensitivity profiles from an array of coils for encoding and reconstruction in parallel (SPACE RIP)," *Magn. Reson. Med.*, vol. 44, no. 2, pp. 301–308, 2000.

[30] F. Lin, T. Witzel, J. Polimeni, J. Hennig, G. Schultz, J. Belliveau, and L. Wald, "Parallel imaging technique using localized gradients (PatLoc) reconstruction using orthogonal mode decomposition.," *17th ISMRM Annual Meeting*, p. 4557, 2009.

[31] L. Tam, J. Stockmann, G. Galiana, and R. Constable, "Null space imaging: Nonlinear magnetic encoding fields designed complementary to receiver coil sensitivities for improved acceleration in parallel imaging," *Magn. Reson. Med.*, vol. 68, no. 4, pp. 1166–1175, 2012.

[32] G. Schultz, D. Gallichan, H. Weber, W. Witschey, M. Honal, J. Hennig, and M. Zaitsev, "Image reconstruction in k-space from MR data encoded with ambiguous gradient fields," *Magn. Reson. Med.*, vol. 73, no. 2, pp. 857–864, 2015.

[33] H. Wang, L. Tam, R. Constable, and G. Galiana, "Fast rotary nonlinear spatial acquisition (FRONSAC) imaging," *Magn. Reson. Med.*, vol. 75, no. 3, pp. 1154–1165, 2016.

[34] L. Tam, G. Galiana, J. Stockmann, H. Tagare, D. Peters, and R. Constable, "Pseudo-random center placement O-space imaging for improved incoherence compressed sensing parallel MRI," *Magn. Reson. Med.*, vol. 73, no. 6, pp. 2212–2224, 2015.

[35] S. Littin, D. Gallichan, A. Welz, F. Jia, A. Dewdney, H. Weber, G. Schultz, J. Hennig, and M. Zaitsev, "Monoplanar gradient system for imaging with nonlinear gradients," *MAGMA*, vol. 28, no. 5, pp. 447–457, 2015.

[36] K. Layton, S. Kroboth, F. Jia, S. Littin, H. Yu, and M. Zaitsev, "Trajectory optimization based on the signal-to-noise ratio for spatial encoding with nonlinear encoding fields," *Magn. Reson. Med.*, vol. 76, no. 1, pp. 104–117, 2016.

[37] D. Hoult, "Rotating frame zeugmatography.," *J. Magn. Reson.*, vol. 33, pp. 183–197, 1979.

[38] C. F., H. Robert, J. Perlo, and D. Pusiolt, "Echo-planar rotating-frame imaging.," *J. Magn. Reson.*, vol. 162, no. 2, pp. 396–401, 2003.

[39] A. Trakic, J. Jin, E. Weber, and S. Crozier, "Model for B_1 imaging in MRI using the rotating RF field.," *Comput. Math. Methods. Med.*, vol. Article ID 461647, pp. 1–11, 2014.

[40] L. Hedges and D. Hoult, "The techniques of rotating frame selective excitation and some experimental results.," *J. Magn. Reson.*, vol. 79, pp. 391–403, 1988.

[41] D. Canet, "Radiofrequency field gradient experiments.," *Prog. Nucl. Magn. Reson. Spectrosc.*, vol. 30, pp. 101–135, 1997.

[42] R. Kartausch, T. Driessle, T. Kampf, T. BasseLsebrink, U. Hoelscher, P. Jakob, F. Fidler, and X. Helluy, "Spatial phase encoding exploiting the Bloch-Siegert shift effect.," *Magn. Reson. Mater. Phy.*, vol. 27, pp. 363–371, 2014.

[43] R. Kartausch, F. Fidler, T. Driele, T. Kampf, T. C. Basse-Lusebrink, U. C. Hoelscher, P. M. Jakob, and X. Helluy, "Spatial phase encoding using a Bloch-Siegert shift gradient," *21th ISMRM Annual Meeting*, p. 0371, 2013.

[44] Y. Wan, M. Qiu1, G. Galiana, and R. Constable, "Nonlinear RF spatial encoding with multiple transmit coils based on Bloch-Siegert shift," *24th ISMRM Annual Meeting*, p. 0099, 2016.

[45] C. Z. Cooley, J. P. Stockmann, B. D. Armstrong, M. Sarracanie, M. H. Lev, M. S. Rosen, and L. L. Wald, "Two-dimensional imaging in a lightweight portable MRI scanner without gradient coils.," *Magn. Reson. Med.*, vol. 73, no. 2, pp. 872–83, 2015.

[46] S. Salajeghe, P. Babyn, J. C. Sharp, and G. E. Sarty, "Non-linear TRASE," *20th ISMRM Annual Meeting*, p. 2461, 2015.

[47] T. S. Ibrahim, R. Lee, B. A. Baertlein, Y. Yu, and P.-M. L. Robitaille, "Computational analysis of the high pass birdcage resonator: finite difference time domain simulations for high-field MRI," *Magn. Reson. Imaging.*, vol. 18, no. 7, pp. 835–843, 2000.

[48] J. Jin, *Electromagnetic Analysis and Design in Magnetic Resonance Imaging.* Biomedical Engineering, Boca Raton, CRC Press, 1998.

[49] F. H. Lin, T. Witzel, G. Schultz, D. Gallichan, W. J. Kuo, F. N. Wang, J. Hennig, M. Zaitsev, and J. W. Belliveau, "Reconstruction of MRI data encoded by multiple nonbijective curvilinear magnetic fields.," *Magn. Reson. Med.*, vol. 68, no. 4, pp. 1145–56, 2012.

[50] F. H. Lin, "Multidimensionally encoded magnetic resonance imaging.," *Magn. Reson. Med.*, vol. 70, no. 1, pp. 86–96, 2013.

[51] F. Testud, D. Gallichan, K. J. Layton, C. Barmet, A. M. Welz, A. Dewdney, C. A. Cocosco, K. P. Pruessmann, J. Hennig, and M. Zaitsev, "Single-shot imaging with higher-dimensional encoding using magnetic field monitoring and concomitant field correction.," *Magn. Reson. Med.*, vol. 73, no. 3, pp. 1340–57, 2015.

[52] S. Tao, J. D. Trzasko, Y. Shu, J. Huston, and M. A. Bernstein, "Integrated image reconstruction and gradient nonlinearity correction," *Magn. Reson. Med.*, vol. 74, no. 4, pp. 1019–1031, 2015.

[53] V. Parot, C. Sing-Long, C. Lizama, C. Tejos, S. Uribe, and P. Irarrazaval, "Application of the fractional Fourier transform to image reconstruction in MRI.," *Magn. Reson. Med.*, vol. 68, no. 1, pp. 17–29, 2012.

[54] G. Schultz, D. Gallichan, M. Reisert, J. Hennig, and M. Zaitsev, "MR image reconstruction from generalized projections.," *Magn. Reson. Med.*, vol. 72, no. 2, pp. 546–57, 2014.

[55] G. Sarty, "Cyclic generalized projection MRI," *Magn. Reson. Imaging.*, vol. 33, no. 3, pp. 304–311, 2015.

[56] A. Neumaier, "Solving ill-conditioned and singular linear systems: A tutorial on regularization," *SIAM. Rev.*, vol. 40, no. 3, pp. 636–666, 1998.

[57] A. Tikhonov and V. Arsenin, *Solutions of Ill-Posed Problems.* New York: Wiley, 1977.

[58] S. Gull and G. Daniell, "Image reconstruction from incomplete and noisy data," *Nature*, vol. 272, no. 5655, pp. 686–690, 1978.

[59] Y. Wang and W. Lu, "Multicriterion maximum entropy image reconstruction from projections.," *IEEE. Trans. Med. Imaging*, vol. 11, no. 1, pp. 70–5, 1992.

[60] D. Calvetti, G. H. Golub, and L. Reichel, "Estimation of the L-Curve via Lanczos Bidiagonalization," *BIT. Numer. Math.*, vol. 39, no. 4, pp. 603–619, 1999.

[61] C. Brezinski, G. Rodriguez, and S. Seatzu, "Error estimates for linear systems with applications to regularization," *Numer. Algorithms*, vol. 49, no. 1-4, pp. 85–104, 2008.

[62] L. Reichel, G. Rodriguez, and S. Seatzu, "Error estimates for large-scale ill-posed problems," *Numer. Algorithms*, vol. 51, no. 3, pp. 341–361, 2008.

[63] L. Elden, "Algorithms for the regularization of ill-conditioned least squares problems," *BIT. Numerical Mathematics*, vol. 17, no. 2, pp. 134–145, 1977.

[64] R. Penrose and J. A. Todd, "A generalized inverse for matrices," *Math. Proc. Cambridge Phil. Soc.*, vol. 51, 1955.

[65] R. D. Van Walle, H. H. Barrett, K. J. Myers, M. I. Altbach, B. Desplanques, A. F. Gmitro, J. Cornells, and I. Lemahieu, "Reconstruction of MR images from data acquired on a general nonregular grid by pseudoinverse calculation," *IEEE. Trans. Med. Imaging*, vol. 19, no. 12, pp. 1160–1167, 2000.

[66] G. Golub and U. Von Matt, "Generalized cross-validation for large-scale problems," *J. Comp. Graph. Stat.*, vol. 6, no. 1, pp. 1–34, 1997.

[67] C. C. Paige and M. A. Saunders, "Lsqr: An algorithm for sparse linear equations and sparse least squares," *ACM. Trans. Math. Softw.*, vol. 8, no. 1, pp. 43–71, 1982.

[68] G. Golub and W. Kahan, "Calculating the singular values and pseudo-inverse of a matrix," *J. SIAM. Numer. Anal. Ser. B*, vol. 2, pp. 205–224, 1965.

[69] A. Björck, "Solving linear least squares problems by Gram-Schmidt orthogonalization," *BIT*, vol. 7, no. 1, pp. 1–21, 1967.

[70] A. Björck, "Numerics of Gram-Schmidt orthogonalization," *Linear. Algebra. Appl.*, vol. 197-198, no. C, pp. 297–316, 1994.

[71] H. Park and S. V. Huffel, "Two-way bidiagonalization scheme for downdating the singular-value decomposition," *Linear. Algebra. Appl.*, vol. 222, pp. 23–39, 1995.

[72] L. A. Shepp and B. F. Logan, "The Fourier reconstruction of a head section," *IEEE. Trans. Nucl. Sci.*, vol. 21, pp. 21–43, June 1974.

[73] H. Y. Carr and E. M. Purcell, "Effects of diffusion on free precession in nuclear magnetic resonance experiments," *Phys. Rev.*, vol. 94, no. 3, pp. 630–638, 1954.

[74] S. Meiboom and D. Gill, "Modified spin-echo method for measuring nuclear relaxation times," *Rev. Sci. Instrum.*, vol. 29, no. 8, pp. 688–691, 1958.

[75] M. H. Levitt and R. Freeman, "Compensation for pulse imperfections in NMR spin-echo experiments," *J. Magn. Reson.*, vol. 43, no. 1, pp. 65–80, 1981.

[76] R. Freeman, S. P. Kempsell, and M. H. Levitt, "Radiofrequency pulse sequences which compensate their own imperfections," *J. Magn. Reson.*, vol. 38, no. 3, pp. 453–479, 1980.

[77] R. Freeman and J. Keeler, "Suppression of artifacts in two-dimensional J spectra," *J. Magn. Reson.*, vol. 43, no. 3, pp. 484–487, 1981.

[78] J. Baum, R. Tycko, and A. Pines, "Broadband population inversion by phase modulated pulses," *J. Chem. Phys.*, vol. 79, no. 9, pp. 4643–4644, 1983.

[79] R. Tycko, H. Cho, E. Schneider, and A. Pines, "Composite pulses without phase distortion," *J. Magn. Reson.*, vol. 61, no. 1, pp. 90–101, 1985.

[80] M. H. Levitt and R. Freeman, "NMR population inversion using a composite pulse," *J. Magn. Reson.*, vol. 33, no. 2, pp. 473–476, 1979.

[81] R. Tycko, "Broadband population inversion," *Phys. Rev. Lett.*, vol. 51, pp. 775–777, Aug 1983.

[82] R. Tycko and A. Pines, "Iterative schemes for broad-band and narrow-band population inversion in NMR," *Chem. Phys. Lett.*, vol. 111, no. 4-5, pp. 462–467, 1984.

[83] R. Tycko, A. Pines, and J. Guckenheimer, "Fixed point theory of iterative excitation schemes in NMR," *J. Chem. Phys.*, vol. 83, no. 6, p. 2775, 1985.

[84] A. J. Shaka and A. Pines, "Symmetric phase-alternating composite pulses," *J. Magn. Reson. (1969)*, vol. 71, no. 3, pp. 495–503, 1987.

[85] A. E. Derome, "A simple composite pulse with low phase distortion," *J. Magn. Reson. (1969)*, vol. 78, no. 1, pp. 113–122, 1988.

[86] V. D. M. Koroleva, S. Mandal, Y. Q. Song, and M. D. Hrlimann, "Broadband CPMG sequence with short composite refocusing pulses," *J. Magn. Reson.*, vol. 230, pp. 64–75, 2013.

[87] S. Wimperis, "Iterative schemes for phase-distortionless composite 180^0 pulses," *J. Magn. Reson (1969)*, vol. 93, no. 1, pp. 199–206, 1991.

[88] S. Wimperis, "Broadband, narrowband, and passband composite pulses for use in advanced NMR experiments," *J. Magn. Reson. Series A*, vol. 109, no. 2, pp. 221–231, 1994.

[89] M. D. Hürlimann, "Carr-Purcell sequences with composite pulses," *J. Magn. Reson.*, vol. 152, no. 1, pp. 109–123, 2001.

[90] F. Bloch, "Nuclear induction," *Phys. Rev.*, vol. 70, no. 7-8, pp. 460–474, 1946.

[91] R. K. S. Kwan, A. C. Evans, and B. Pike, "MRI simulation-based evaluation of image-processing and classification methods," *IEEE Trans. Med. Imag.*, vol. 18, no. 11, pp. 1085–1097, 1999.

[92] A. R. Brenner, J. Kürsch, and T. G. Noll, "Distributed large-scale simulation of magnetic resonance imaging," *MAGMA*, vol. 5, no. 2, pp. 129–138, 1997.

[93] H. Benoit-Cattin, G. Collewet, B. Belaroussi, H. Saint-Jalmes, and C. Odet, "The SIMRI project: A versatile and interactive MRI simulator," *J. Magn. Reson.*, vol. 173, no. 1, pp. 97–115, 2005.

[94] J. Bittoun, J. Taquin, and M. Sauzade, "A computer algorithm for the simulation of any nuclear magnetic resonance (NMR) imaging method," *Magn. Reson. Imaging.*, vol. 2, no. 2, pp. 113–120, 1984.

[95] M. Olsson, R. Wirestam, and B. Persson, "A computer simulation program for MR imaging: Application to RF and static magnetic field imperfections," *Magn. Reson. Med.*, vol. 34, no. 4, pp. 612–617, 1995.

[96] F. Bälibanu, K. Hailu, R. Eymael, D. E. Demco, and B. Blümich, "Nuclear magnetic resonance in inhomogeneous magnetic fields," *J. Magn. Reson.*, vol. 145, no. 2, pp. 246–258, 2000.

[97] L. I. Rudin, S. Osher, and E. Fatemi, "Nonlinear total variation based noise removal algorithms," *Phys. D Nonlinear Phenom.*, vol. 60, no. 1-4, pp. 259–268, 1992.

[98] P. Rodriguez and B. Wohlberg, "Efficient minimization method for a generalized total variation functional," *IEEE Trans. Image Processing.*, vol. 18, no. 2, pp. 322–332, 2009.

[99] A. Beck and M. Teboulle, "Fast gradient-based algorithms for constrained total variation image denoising and deblurring problems," *IEEE Trans. Image Processing.*, vol. 18, no. 11, pp. 2419–2434, 2009.

[100] K. T. Block, M. Uecker, and J. Frahm, "Undersampled radial MRI with multiple coils. iterative image reconstruction using a total variation constraint," *Magn. Reson. Med.*, vol. 57, no. 6, pp. 1086–1098, 2007.

[101] A. Chambolle, "An algorithm for total variation minimization and applications," *J. Math. Imaging. Vision.*, vol. 20, no. 1-2, pp. 89–97, 2004.

[102] A. Beck and M. Teboulle, "A fast iterative shrinkage-thresholding algorithm for linear inverse problems," *SIAM J. Imaging. Sci.*, vol. 2, no. 1, pp. 183–202, 2009.

[103] S. Odedra, M. J. Thrippleton, and S. Wimperis, "Dual-compensated antisymmetric composite refocusing pulses for NMR," *J. Magn. Reson.*, vol. 225, pp. 81–92, 2012.

[104] S. Odedra and S. Wimperis, "Use of composite refocusing pulses to form spin echoes," *J. Magn. Reson.*, vol. 214, pp. 68–75, 2012.

[105] R. Kleinberg, A. Sezginer, D. Griffin, and M. Fukuhara, "Novel NMR apparatus for investigating an external sample," *J. Magn. Reson. (1969)*, vol. 97, no. 3, pp. 466–485, 1992.

[106] G. Eidmann, R. Savelsberg, P. Blmler, and B. Blmich, "The NMR MOUSE, a mobile universal surface explorer," *J. Magn. Reson. Ser. A.*, vol. 122, no. 1, pp. 104–109, 1996.

[107] C. Z. Cooley, J. P. Stockmann, M. Sarracanie, and L. L. Wald, "3D imaging in a portable MRI scanner using rotating spatial encoding magnetic fields and transmit array spatial encoding (TRASE)," *20th ISMRM Annual Meeting*, p. 0703, 2015.

[108] M. A. Bernstein, K. F. King, and X. J. Zhou, *Handbook of MRI Pulse Sequences*. Elsevier, 2004.

[109] F. A. Grunbaum, "An inverse problem related to the bloch equations and a non-linear fourier transform," *Inverse Problems*, vol. 1, no. 3, p. L25, 1985.

[110] R. Gordon, R. Bender, and G. Herman, "Algebraic reconstruction techniques (ART) for three-dimensional electron microscopy and X-ray photography," *J. Theor. Biol.*, vol. 29, no. 3, pp. 471–"476,IN1–IN2,477–481", 1970.

[111] D. Needell, "Randomized Kaczmarz solver for noisy linear systems," *BIT Numer. Math.*, vol. 50, no. 2, pp. 395–403, 2010.

[112] M. R. Hestenes and E. Stiefel, "Methods of Conjugate Gradients for solving linear systems," *J. Res. Natl. Stand.*, vol. 49, no. 6, pp. 409–436, 1952.

Appendix

Contributions

Authors contribution: Somaie Salajeghe was jointly responsible for the original ideas behind the papers and abstracts, conducting the experiments, image and data analyses, presentation of the findings, and writing and editing of the original contributions. Dr. Logi Vidarsson built the portable MRI and provided technical advice. Dr. Jonathan Sharp provided technical advice. Dr. Gordon Sarty and Dr. Paul Babyn were jointly responsible for the original ideas, provided supervision, and was the key editor on these contributions.

Published Papers

1. Somaie Salajeghe, Paul Babyn, Jonathan C. Sharp, Gordon E. Sarty, "Least Squares Reconstruction of RF encoded MRI Data", Magnetic Resonance Imaging, 34(7):951-63, 2016.

   This research is discussed in detail in Chapter 3 and Chapter 4 of this thesis.

Submitted Papers

1. Somaie Salajeghe, Paul Babyn, Gordon E. Sarty, "Composite pulses for RF phase encoded MRI: A Simulation Study", Magnetic Resonance Imaging, under revision.

   This research is discussed in detail in Chapter 5 of this thesis.

2. Somaie Salajeghe, Paul Babyn, Logi Vidarsson, Gordon E. Sarty, "Gradient Free MRI with rotating magnet and receiver fields", under preparation.

   This research is discussed in Chapter 6 of this thesis.

Conference

1. Somaie Salajeghe, Paul Babyn, Logi Vidarsson, Gordon E. Sarty, "Gradient Free MRI with a rotating magnet and receiver fields", International Society for Magnetic Resonance in Medicine (ISMRM 2016), May 7-May 13, Singapore.

   This research is discussed in detail in Chapter 6 of this thesis.

2. Somaie Salajeghe, Paul Babyn, Gordon E. Sarty, "Composite pulses for RF phase encoded MRI", International Society for Magnetic Resonance in Medicine (ISMRM 2016), May 7-May 13, Singapore.

   This research is discussed in Chapter 5 of this thesis.

3. Somaie Salajeghe, Paul Babyn, Jonathan C. Sharp, Gordon E. Sarty, "Image reconstruction of RF encoded MRI signals in an inhomogeneous B_0 field", World Congress on Medical Physics and Biomedical Engineering (2015), June 7-June 12, Toronto, ON, Canada.

   This research is discussed in Chapter 5 of this thesis.

4. Somaie Salajeghe, Paul Babyn, Jonathan C. Sharp, Gordon E. Sarty, "Non-linear TRASE" International Society for Magnetic Resonance in Medicine (ISMRM 2015), May 30-June 5, Toronto, ON, Canada.

   This research is discussed in Chapter 3 and Chapter 4 of this thesis.

5. Somaie Salajeghe, Paul Babyn, Jonathan C. Sharp, Gordon E. Sarty, "RF-Encoded MRI Image Reconstruction Using a Non-Linear Discrete Fourier Transform". Canadian Society of Applied and Industrial Mathematics (CAIMS) , June 2014, Saskatoon, SK, Canada.

   This research is discussed in Chapter 3 and chapter 4 of this thesis.

6. Somaie Salajeghe, Paul Babyn, Jonathan C. Sharp, Gordon E. Sarty, "MRI simulation of Non-linear TRASE data in an inhomogeneous B_0 and B_1 field via Bloch Equation". 21st Annual Life and Health Sciences Research Day, March 2015, Saskatoon, Canada.

   This research is discussed in Chapter 5 of this thesis.